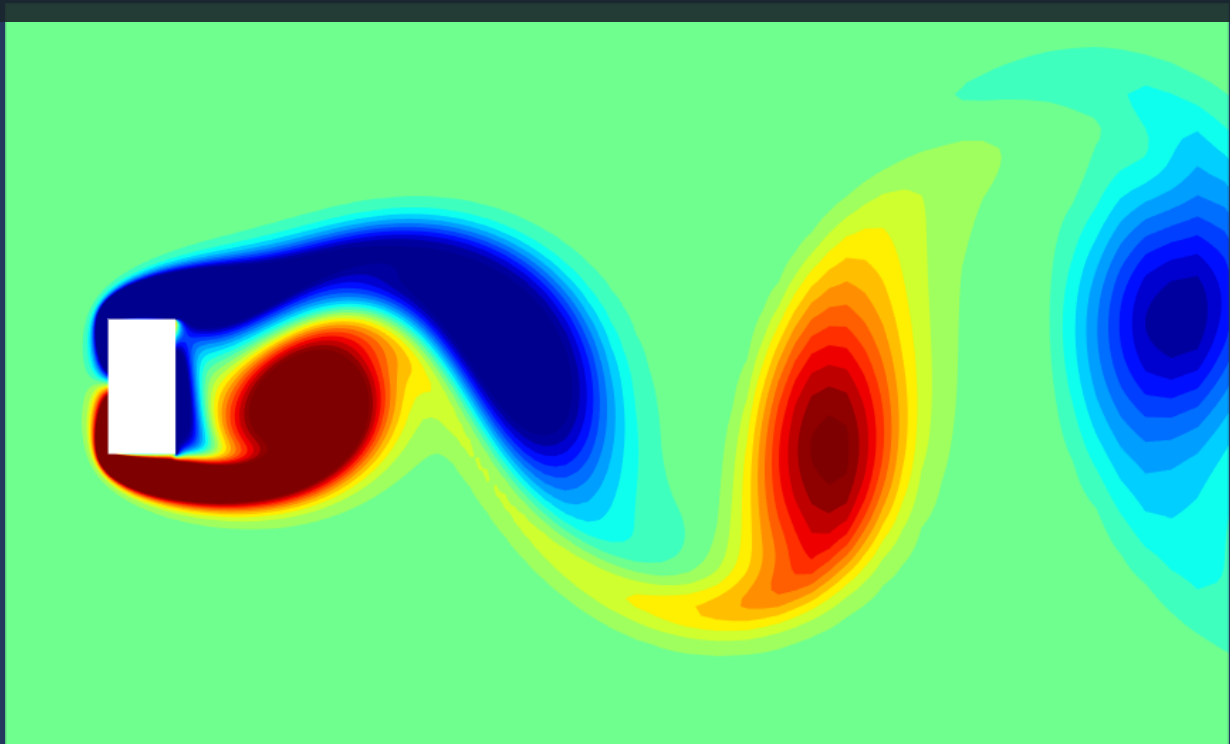# Hybrid Dual Mimetic Spectral Element Method with a Novel Dual Grid

Zeyuan Zhou

Hybrid Dual Mimetic Spectral Element Method with a Novel Dual Grid

Thesis report

by

Zeyuan Zhou

to obtain the degree of Master of Science
at the Delft University of Technology
to be defended publicly on October 27, 2023 at 14:00

Thesis committee:

Chair:	Dr. M.I. Gerritsma
Supervisors:	Dr. M.I. Gerritsma
External examiner:	Dr. A.H. van Zuijlen
	Dr. F. de Prenter
	Dr. A. Palha
Place:	Faculty of Aerospace Engineering, Delft
Project Duration:	January, 2023 - August, 2023
Student number:	5540399

An electronic version of this thesis is available at `http://repository.tudelft.nl/`.

Faculty of Aerospace Engineering · Delft University of Technology

TU Delft

Delft
University of
Technology

Preface

This thesis presents the research output in developing the hybrid dual mimetic spectral element method with a novel dual grid, which is a part of the effort to get the Master of Science degree at the Aerospace Faculty of Delft University of Technology.

First, I would like to thank my supervisor, Marc Gerritsma, and two PhDs who have worked in this field for many years, Yi Zhang and Artur Palha, for their guidance and assistance during the research and the completion of my master's thesis.

I would also like to thank my family, friends, and schoolmates for accompanying me through the busy and fulfilling two years of my master's program.

Abstract

The mimetic spectral element method (MSEM) is a structure-preserving discretization scheme based on the Galerkin Method, which strongly constrains the topology relations by discretizing and reconstructing variables in specific function spaces in order to preserve certain critical structures of the PDE in the numerical solution. In studying the 2D incompressible Navier-Stokes equations, the conservation law of mass, energy, vorticity, and enstrophy (or helicity for 3D cases) are expected to be preserved. According to the de Rham complex, the mimetic spectral element method uses differential forms rather than vector or scalar fields to present physical variables and discretize differential forms on specified function spaces. It has two significant advantages. Firstly, the topological relations between discretized variables depend only on the grid's topology structure, which means no numerical errors are introduced into the discretized conservation equations. Secondly, the variables are reconstructed with spectral functions, which can be of arbitrary high order.

Based on the MSEM, a more efficient hybrid dual mimetic spectral element method (hdMSEM) was proposed. In the hybrid mimetic spectral element method (hMSEM), a set of trace function spaces and trace variables are introduced at the interface between subdomains, applying a Lagrange multiplier to strongly couple the variables of bordered subdomains so that domain decomposition is feasible, and the solver can run in parallel efficiently. In addition, designing a proper set of dual grid and dual function spaces for trace variables can further increase the sparsity of the matrix, thus saving computational resources. However, a singularity problem arises in the structure-preserving simulation of incompressible flows with the primal hdMSEM when Lagrange multipliers are applied to couple variables of vorticity at the edge where more than two subdomains meet.

This thesis proposes the hybrid dual mimetic spectral element method with a novel dual grid, which can avoid the singularity and simultaneously keep the matrix of the discrete system symmetrical and the mathematical definition of the matrix equations rigorous. The basic idea is to introduce a dummy degree of freedom at the edge where singularity arises and design a curvilinear dual grid for trace variables to couple the degree of freedom of vorticity and the dummy degree of freedom to eliminate singularity. Besides, this thesis studies the implementations of several kinds of boundary conditions with the novel dual grid and the corresponding grid topology near boundaries. Then, we extend the hdMSEM with the novel dual grid to solve steady and unsteady 2D incompressible Navier-Stokes equations. In numerical experiments, the accuracy and structure-preserving capability are verified numerically with several benchmark cases.

Contents

Nomenclature

$\widetilde{\text{TF}}_{N-1}$ Dual discrete function space for trace variables associated to face in Nth-order element

$\widetilde{\text{VP}}_{N-1}$ Dual discrete function space for variables associated to volume in Nth-order element

P Total pressure field

p Static pressure field

P^h Discrete total pressure field

p^h Discrete static pressure field

EP_N Discrete function space for variables associated to edge in Nth-order element

FP_{N-1} Discrete function space for variables associated to face in Nth-order element

M_E Mass matrix for dofs associated to edge

M_F Mass matrix for dofs associated to face

M_TE Mass matrix for trace dofs associated to edge

M_TF Mass matrix for trace dofs associated to face

M_V Mass matrix for dofs associated to volume

TE_N Discrete function space for trace variables associated to edge in Nth-order element

TF_{N-1} Discrete function space for trace variables associated to face in Nth-order element

VP_{N-1} Discrete function space for variables associated to volume in Nth-order element

List of Figures

List of Tables

Introduction

Within computational physics, the structure-preserving method is a topic of great interest because, in the partial differential equations describing physical problems, some topological relations reflect the most fundamental laws of nature, such as the law of conservation of mass or the law of conservation of energy [1]. Numerical discretization methods should keep such structures to obtain a stable and reliable solution. The theoretical basis of structure-preserving methods, also known as mimetic methods, is derived from Whitney's theory [2] of geometrical integration and Tonti's classification scheme [3] of variables in the physical equations. This means structure-preserving methods often have multiple geometric elements for discrete domains, such as node, edge, surface, and volume, and therefore have a more complex grid structure than traditional grids based on nodes and cells.

Following the idea of previous mimetic methods, Gerritsma, Palha, Kreeft, et al. [4, 5, 6, 7, 8] built the framework of the mimetic spectral element method (MSEM), which associates different physical variables with different geometrical elements and reconstructs the variables field with high-order piecewise polynomials in spectral elements. Compared to a traditional solver for incompressible flow only considering the velocity field and pressure field, vorticity is listed as an independent variable in MSEM and related to the velocity field with the curl operator:

$$\nabla \times \boldsymbol{u} = \boldsymbol{\omega},$$

which is not so trivial, because vorticity and velocity (flux) are both on the primal grid, while the curl operator is defined on the dual grid. So, this equation is critical in preserving the conservation law of vorticity. Based on the framework of MSEM, Zhang [9] proposed a hybrid mimetic spectral element method (hMSEM) for domain decomposition by introducing trace variables and then developed hybrid dual MSEM (hdMSEM) [10] by choosing a dual grid and dual function space for primal variables and trace variables to increase computing efficiency. These developments make hdMSEM stable and efficient while resulting in a highly complex set of function spaces and grid topology for discretization.

In studying incompressible flow problems with hdMSEM, vorticity variables are associated with elements' edges. However, a singularity problem arises at the edge where more than two subdomains meet when applying Lagrange multipliers to couple the variables of vorticity. Thus, this thesis proposes a novel dual grid for the hybrid dual mimetic spectral element method to eliminate the singularity problem and further develop the hdMSEM with the novel dual grid to study incompressible fluid dynamics problems.

1.1. Literature review

An idea to classify fundamental physical quantities was firstly proposed by Tonti [3, 11, 12, 13] in the 1970s, in whose theory, *differential geometry* [14, 15, 16, 17, 18] is strongly related to *algebraic topology* [19, 20]. This scheme describes variables at grid nodes and associates them with geometric elements of different dimensions like lines, faces, and volumes called *k-cells* in algebraic topology, where k is the dimension of the geometric element. Those *k-cells* form a *k-chain* on a grid, and different *k-chains* are associated with the operator of differential geometry, such as gradient, divergence, and curl. Correspondingly, the degrees of freedom of discrete differential *k-forms* can be presented by the association between *k-chain* and *k-cochain* [16], which explains the meaning of starting from differential forms in computational physics. Tonti's theory gives a very general principle to define the association between physical variables in PDE

and geometric elements in a discrete scheme and serves as a robust principle to guide the design of a structure-preserving method [1].

Before Tonti's theory, Whitney proposed a form describing the transformation between flat cochains and differential forms in his geometric integration theory [2] in 1957. Furthermore, in 1974, this form was first applied in a finite difference method for harmonic form problems by Dodziuk [21], and named Whitney forms [22]. Besides the application in finite difference methods, a branch of finite element methods called *mixed finite element method* proposed by Brezzi, Raviart, Thomas, Nédélec, Douglas, et al. [23, 24, 25, 26, 27, 28], which use a set of mixed function spaces in the element. These mixed elements also use the idea of Whitney's form. Therefore, they are also known as *Whitney elements* [29, 30]. In the 1980s, Bossavit [31] used Whitney forms and Whitney elements in computational electromagnetics. In his method, physical variables are described in differential forms rather than scalar or vector fields, which allows the integration of variables over certain geometric elements to be accurately preserved in spatial discretization. The success of Bossavit's work is a presentative case in the development of mimetic discretization. It demonstrates the potential of the Whitney form in the structure-preserving method, and the Whitney form generally refers to finite elements for differential forms [22].

In the 2000s, Bochev and Hyman [32] proposed a more general theory covering the association between algebraic topology and differential forms in all of FDM, FEM, and FVM. This theory defines two basic operations, the *reconstruction* and the *reduction*, where reduction projects differential forms on cochains and reconstruction projects variables from cochains back to differential forms. In a spatial discrete numerical scheme, reduction introduces no numerical errors while reconstruction does, so the conservation law of physical problems should be implemented with pure reduction operation without reconstruction to preserve the structure. Besides, the idea of exterior calculus [33] and Hodge operator [34] are widely used in developing dual grid methods for differential forms.

To parallelize the computing and save computational resources, *hybridization* is one of the most common technics used in domain decomposition. Hybrid finite element method [25, 35] is a kind of FEM that allows discontinuity between bordered elements but then imposes a strong continuity by applying Lagrange multiplier [35], and it is commonly used in domain decomposition method, which divided the large-scale global matrix into sparser and smaller sub-matrices. The idea of hybridization originates from the field of solid mechanics. In the 1960s, Pian proposed the assumed stress hybrid method [36], which is the first hybrid element method to investigate solid mechanics, and then the assumed displacement method [37] and the assumed stress-displacement mixed method [38] were developed respectively in 1970 and 1976. Other methods like mortar element method [39, 40] and finite element tearing and interconnecting (FETI) method [41] are also constructed based on the idea of hybridization. Hybridization sometimes results in the problem of ill-posedness, and in 1974, the uniqueness of the saddle-point problem arising from the Lagrange multiplier was studied by Brezzi [42].

Mimetic spectral element method (MSEM), proposed and developed by Gerritsma, Palha, Kreeft et al. [4, 5, 6, 7, 8], follows the idea of Bochev and Hyman frameworks, the discrete exterior calculus and the finite element exterior calculus. MSEM uses differential forms in different dimensions according to the de Rham complex to describe physical variables, so the first-order differential operators, ∇, $\nabla\times$ and $\nabla\cdot$, which are also named primal operators, are purely topology operator so that there are no numerical errors introduced to the topological structure in spatial discretization. In the element of MSEM, Lagrange polynomials and edge polynomials are used to build node polynomials, edge polynomials, face polynomials, and volume polynomials, which are basis functions respectively for $n-3$-*form*, $n-2$-*form*, $n-1$-*form* and n-*form*, for example, in the domain of $\mathbb{R}^3$ [4]. Based on the framework of MSEM, Zhang [10] extended the hybridization to MSEM and proposed the hybrid mimetic spectral element method (hMSEM). Hybridization introduces trace degrees of freedom on the surface of elements and doubles the degrees of freedom bordered with inter-element surfaces, so it is especially efficient to be applied in the high-order spectral element method, of which the number of degrees of freedom on the surface is small compared to the number of degrees of freedom inside elements. To further increase the sparsity of the matrix and improve the condition of the discrete system, dual basis functions are used in hMSEM, and this new extension of hMSEM is called *hybrid dual mimetic spectral element method* (hdMSEM) [43, 44, 45]. The hdMSEM is applied to solve Poisson problem [44], linear elasticity problem [9] successfully, however, raises a singularity problem when using Lagrange multipliers to couple the vorticity in $n-2$-*form* of two bordered elements in solving incompressible flow problems. In the preliminary research of Zhang [10], a dummy degree of freedom is introduced at the edge where singularity arises and successfully implemented in

lid-driven Stokes flow simulation, where all boundaries satisfy the no-slip wall condition. However, this solution has drawbacks: it leads to an asymmetric matrix of the discrete system, and the matrix equations for coupling have ambiguous mathematical definitions in the hdMSEM.

In 2017, Palha and Gerritsma [46] proposed a mass, energy, enstrophy, and vorticity conserving (MEEVC) scheme for 2D incompressible Navier-Stokes equations. The MEEVC scheme formulates N-S equations in a velocity-vorticity formulation in rotational form, using the MSEM as spatial discretization scheme to preserve the topology of divergence-free fields and a conserving integrator in temporal discretization. Currently, Zhang is developing a new MEEVC scheme [47], an alternative to the original MEEVC. In the new MEEVC, the non-slip boundary condition can be applied without breaking the discrete conservation law of vorticity.

1.2. Research Objective

The main objective of the thesis is to propose the hybrid dual mimetic spectral element method with a novel dual grid to solve incompressible fluid dynamics problems.

The research focuses on the following several sub-questions:

1. Can we design a novel dual grid for the hdMSEM to eliminate the singularity problem while keeping the discrete system symmetric and the mathematical definition of matrix equations rigorous?

2. How to implement different boundary conditions in the hdMSEM with the novel dual grid?

3. How to extend the hdMSEM with the novel dual grid to solve steady and unsteady incompressible Navier-Stokes equations and implement the MEEVC scheme in the framework of the hdMSEM with the novel dual grid?

1.3. Report structure

The remaining part of this thesis is organized as follows: In Chapter 2, we introduce the framework of the hdMSEM and analyze the singularity problem that arises in studying incompressible Stokes flow; In Chapter 3, we propose the hdMSEM with a novel dual grid, including the topology of the novel dual grid, the implementation of the physical boundary conditions, and its extension to studying steady and unsteady Navier-Stokes equations; In Chapter 4, the performance of the numerical method including accuracy and conservation are verified through several benchmark cases covering all of Stokes equations, steady and unsteady Navier-Stokes equations; And we give the conclusion and recommendation for the future work in the Chapter 5.

2

The Framework of the Hybrid Dual Mimetic Spectral Element Method

This chapter introduces the framework of the hybrid dual mimetic spectral element method (hdMSEM). Firstly, we demonstrate the mimetic spectral element method (MSEM) [4, 5, 6, 7, 8] and its application in 2D incompressible Stokes flow. Then, the hybridization [9] is introduced into the mimetic spectral element method for domain decomposition, and correspondingly, a set of dual grid and dual function spaces [10, 43] are applied to further increase the computational efficiency. At last, we analyze the singularity problem that arises from the hdMSEM when coupling the vorticity variables at the edge where more than two elements meet inside the domain and a preliminary solution to the singularity problem given by Zhang [10].

2.1. Mimetic Spectral Element Method

This section introduces the mimetic spectral element method (MSEM), including the mathematical basis, the polynomials, and the function spaces in $\mathbb{R}^2$, and the application of the MSEM in studying 2D incompressible Stokes flow.

2.1.1. The de Rham complex

The de Rham complex [17, 32, 48] is the cochain complex of differential *k*-form spaces, which are connected with exterior derivative. A general form can be written as:

$$0 \to \Lambda^0(\Omega) \xrightarrow{d} \Lambda^1(\Omega) \xrightarrow{d} \Lambda^2(\Omega) \xrightarrow{d} ... \xrightarrow{d} \Lambda^n(\Omega) \to 0, \tag{2.1}$$

where d is the exterior derivative operator, $\Lambda^0(\Omega)$ is the space of smooth functions on domain Ω, $\Lambda^1(\Omega)$ is the space of 1-forms and so on.

In $\mathbb{R}^1$, there is:

$$0 \to H^1(\Omega) \xrightarrow{\nabla} L^2(\Omega) \to 0,$$
$$0 \to H(\mathsf{div}; \Omega) \xrightarrow{\nabla \cdot} L^2(\Omega) \to 0, \tag{2.2}$$

where $H^1(\Omega) = H(\mathsf{div}; \Omega)$ in $\mathbb{R}^1$.

In $\mathbb{R}^2$, there is:

$$0 \to H^1(\Omega) \xrightarrow{\nabla} H(\mathsf{rot}; \Omega) \xrightarrow{\nabla \times} L^2(\Omega) \to 0,$$
$$0 \to H(\mathsf{curl}; \Omega) \xrightarrow{\nabla \times} H(\mathsf{div}; \Omega) \xrightarrow{\nabla \cdot} L^2(\Omega) \to 0, \tag{2.3}$$

and in $\mathbb{R}^3$, there is

$$0 \to H^1(\Omega) \xrightarrow{\nabla} H(\mathsf{curl}; \Omega) \xrightarrow{\nabla \times} H(\mathsf{div}; \Omega) \xrightarrow{\nabla \cdot} L^2(\Omega) \to 0. \tag{2.4}$$

That sequence shows inclusion relations between different functional spaces. The range of an operator is a subspace of the next space, and what is more, the subspace projected from the previous space has a null space projected by the next operator.

In this thesis, all cases studied are in 2D, so in the following part, only the derivation of the numerical method in $\mathbb{R}^2$ is discussed.

4

2.1.2. The dual de Rham complex

Based on the de Rham complex, there is the other sequence of function spaces called dual de Rham complex and the other set of operators called dual operators.

Take an example in $\mathbb{R}^2$, divergence operator can be expressed as

$$\nabla \cdot : H(\text{div}; \Omega) \to L^2(\Omega), \tag{2.5}$$

so an adjoint operator can be defined as

$$\widetilde{\nabla} : L^2(\Omega) \to H(\text{div}; \Omega), \tag{2.6}$$

where the adjoint operator $\widetilde{\nabla}$ is called as the dual gradient operator.

Similarly, we can obtain the dual curl operator

$$\widetilde{\nabla \times} : H(\text{div}; \Omega) \to H(\text{curl}; \Omega). \tag{2.7}$$

So the dual de Rham complex can be expressed as Fig. 2.1.

$$0 \longrightarrow H^1(\Omega) \overset{\nabla}{\longrightarrow} H^1(\text{rot}; \Omega) \overset{\nabla \times}{\longrightarrow} L^2(\Omega) \longrightarrow 0$$

$$0 \longleftarrow H^1(\Omega) \overset{\widetilde{\nabla} \cdot}{\longleftarrow} H^1(\text{rot}; \Omega) \overset{\widetilde{\nabla \times}}{\longleftarrow} L^2(\Omega) \longleftarrow 0$$

$$0 \longrightarrow H^1(\text{curl}; \Omega) \overset{\nabla \times}{\longrightarrow} H^1(\text{div}; \Omega) \overset{\nabla \cdot}{\longrightarrow} L^2(\Omega) \longrightarrow 0$$

$$0 \longleftarrow H^1(\text{curl}; \Omega) \overset{\widetilde{\nabla \times}}{\longleftarrow} H^1(\text{div}; \Omega) \overset{\widetilde{\nabla}}{\longleftarrow} L^2(\Omega) \longleftarrow 0$$

Figure 2.1: The double de Rham complex in $\mathbb{R}^2$.

In MSEM, primal and dual operators correspond to two types of operations: reduction and reconstruction. Moreover, they can be converted to each other by integration by part:

$$\langle \boldsymbol{v}, \widetilde{\nabla} \varphi \rangle_{\Omega} = -\langle \nabla \cdot \boldsymbol{v}, \varphi \rangle_{\Omega} + \int_{\partial \Omega} \varphi (\boldsymbol{v} \cdot \boldsymbol{n}) d\Gamma \quad \forall \boldsymbol{v} \in H(\text{div}; \Omega), \tag{2.8}$$

$$\langle \boldsymbol{\omega}, \widetilde{\nabla \times} \boldsymbol{u} \rangle_{\Omega} = \langle \nabla \times \boldsymbol{\omega}, \boldsymbol{u} \rangle_{\Omega} - \int_{\partial \Omega} \boldsymbol{\Omega} \cdot (\boldsymbol{u} \times \boldsymbol{n}) d\Gamma \quad \forall \boldsymbol{\omega} \in H(\text{curl}; \Omega). \tag{2.9}$$

Moreover, the function spaces of boundary variables can be defined as:

$$\varphi|_{\partial \Omega} \in H^{1/2}(\partial \Omega) \quad \text{and} \quad \boldsymbol{u} \times \boldsymbol{n} \in TH_{\perp}(\partial \Omega). \tag{2.10}$$

2.1.3. Basic Mimetic Polynominals

In the mimetic spectral element method, we consider three discrete function spaces,

$$\{C(\Omega), D(\Omega), S(\Omega)\},$$

such that

$$\begin{array}{ccc}
C(\Omega) & \subset & H(\text{curl}; \Omega) \\
\downarrow \nabla \times & & \downarrow \nabla \times \\
D(\Omega) & \subset & H(\text{div}; \Omega) \\
\downarrow \nabla \cdot & & \downarrow \nabla \cdot \\
S(\Omega) & \subset & L^2(\Omega).
\end{array} \tag{2.11}$$

Then, these three function spaces form a discrete de Rham complex. The function space set used in this thesis is called *mimetic polynomial spaces* [44]. The construction of mimetic polynomial spaces based on two kinds of basic polynomials: Lagrange polynomials and edge polynomials [4].

Lagrange polynomials For cases in $\mathbb{R}^1$, considering a set of node $\{\xi_0, \xi_1, \ldots, \xi_N\}$ in the 1D reference domain $I_{\text{ref}} = [-1, 1]$:

$$-1 = \xi_0 < \xi_1 < \cdots < \xi_N = 1,$$

where the distribution of these nodes follows the Legendre-Gauss-Lobatto (LGL) nodes [49]. And the Lagrange polynomials,

$$l^i(\xi) = \prod_{j=0, j\neq i}^{N} \frac{\xi - \xi_j}{\xi_i - \xi_j}, \quad i \in \{0, 1, \ldots, N\}, \tag{2.12}$$

is a set of polynomials of degree N and satisfies Kronecker delta property:

$$l^i(\xi_j) = \delta_j^i = \begin{cases} 1 & \text{if } i = j \\ 0 & \text{else} \end{cases}. \tag{2.13}$$

An example of $4th$-order Lagrange polynomials is demonstrated in Fig. 2.2.
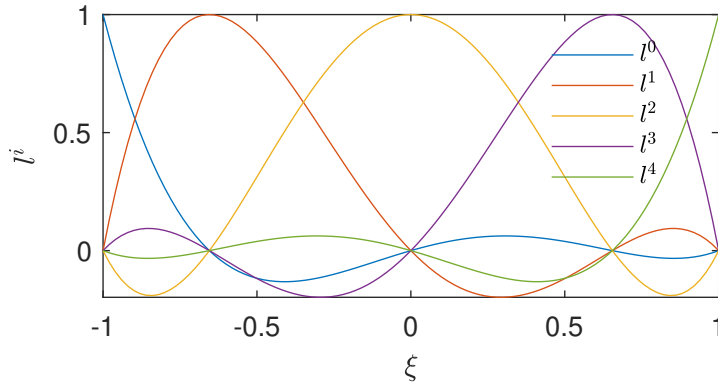
Figure 2.2: $4th$-order Lagrange polynomials.

Edge polynominals Based on the derivatives of Lagrange polynomials, a set of edge functions can be derived as:

$$e^i(\xi) = \sum_{j=i}^{N} \frac{dl^j(\xi)}{d\xi} = -\sum_{j=0}^{i-1} \frac{dl^j(\xi)}{d\xi}, \quad i \in \{1, 2, \ldots, N\}, \tag{2.14}$$

Which satisfies the integral Kronecker delta property:

$$\int_{\xi_{j-1}}^{\xi_j} e^i(\xi) d\xi = \delta_j^i. \tag{2.15}$$

An example of $4th$-order edge polynomials is demonstrated in Fig. 2.3.

So in a 1D domain, the Lagrange polynomials span a discrete polynomial space denoted as $\text{LP}_N(I_{\text{ref}})$:

$$\text{LP}_N(I_{\text{ref}}) = \text{span}(\{l^0(\xi), l^1(\xi), \ldots, l^N(\xi)\}),$$

and a discrete polynominal spaces $\text{EP}_N I_{\text{ref}}$, spanned by edge polynomials:

$$\text{EP}_N(I_{\text{ref}}) = \text{span}(\{e^0(\xi), e^1(\xi), \ldots, e^N(\xi)\}).$$

Then a polynomial of degree N can be expanded as:

$$p^h(\xi) = \sum_{i=0}^{N} p_i l^i(\xi), \tag{2.16}$$
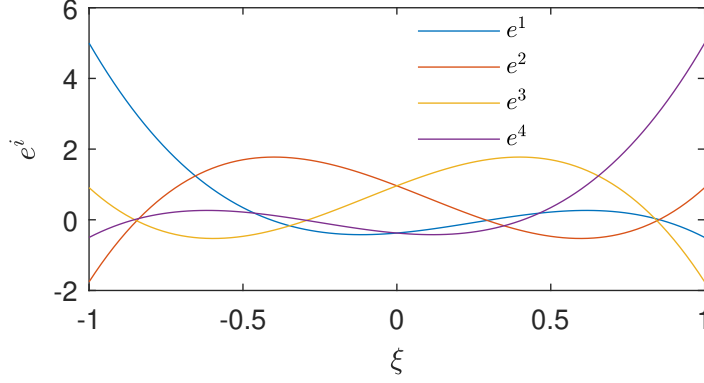
Figure 2.3: $4th$-order edge polynominals.

where $p_i \in \mathbb{R}$ are the expansion coefficients (degrees of freedom). The discrete function satisfies the nodal Kronecker delta property:

$$p^h(\xi_i) = p_i. \tag{2.17}$$

And the derivatives of function $p^h(\xi)$ can be constructed with edge polynominals:

$$q^h(\xi) = \frac{dp^h(\xi)}{d\xi} = \sum_i^N q_i e^i(\xi), \tag{2.18}$$

where q_i are the degrees of freedom and the discrete function satisfies the integral Kronecker delta property:

$$\int_{\xi_{i-1}}^{\xi_i} q^h(\xi)d\xi = q_i. \tag{2.19}$$

It is easy to find the relation between q_i and p_i by intergrating over ξ_{i-1} to ξ_i:

$$q_i = p_i - p_{i-1}. \tag{2.20}$$

Then define the vector of degrees of freedom q_i and p_i as $\underline{q}$ and $\underline{p}$, and the relation between $\underline{q}$ and $\underline{p}$ can be written as:

$$\underline{q} = E\underline{p}, \tag{2.21}$$

where E is the incidence matrix. Take the example when $N = 4$, the incidence matrix E is

$$E = \begin{bmatrix} -1 & 1 & 0 & 0 & 0 \\ 0 & -1 & 1 & 0 & 0 \\ 0 & 0 & -1 & 1 & 0 \\ 0 & 0 & 0 & -1 & 1 \end{bmatrix}. \tag{2.22}$$

The incidence matrix is composed only of entries -1, 1 and 0. Therefore, no geometrical information of grid nodes ξ_i is introduced in the incidence matrix, and it is the basis of structure-preserving capability.

2.1.4. Polynominals in 2D MSEM

Now considering cases in $\mathbb{R}^2$, and use coordinate system (ξ, η), and for reference domain $\Omega_{\text{ref}} = [-1, 1]^2$, there are a set of nodes

$$\{\xi_0, \xi_1, \dots, \xi_N\}, \text{ and } \{\eta_0, \eta_1, \dots, \eta_N\}$$

in interval $[-1, 1]$, i.e., $-1 = \xi_0 < \xi_1 < \cdots < \xi_N = 1$ and $-1 = \eta_0 < \eta_1 < \cdots < \eta_N = 1$. In 2D space, the edge perpendicular to the page plane is presented as a node, and the face perpendicular to the page plane is presented as a line. To be consistent with the physical meaning and to facilitate future extension into 3D space, the polynomials associated with them are still named as *edge polynominals* and *face*

polynominals. Similarly, the physical volume is a surface in the 2D plane, and its polynomials are named *Volume polynominals*.

Edge polynominals Define a set of polynomials,

$$\left\{ \text{II}^{i,j}(\xi,\eta) \,\middle|\, i,j \in \{0,1,...,N\} \right\}, \tag{2.23}$$

where $\text{II}^{i,j}(\xi,\eta) = l^i(\xi) l^j(\eta)$. Edge polynomials should satisfy the Kronecker delta property

$$\text{II}^{i,j}(\xi_l,\eta_m) = \delta_{l,m}^{i,j} = \begin{cases} 1 & \text{if } i = l, \ j = m \\ 0 & \text{else} \end{cases}. \tag{2.24}$$

The discrete function space spanned by edge polynomials is denoted as:

$$\text{EP}_N(\Omega_{\text{ref}}) = \text{span}\left(\left\{ \text{II}^{i,j}(\xi,\eta) = \,\middle|\, i,j \in \{0,1,...,N\} \right\} \right). \tag{2.25}$$

Face polynominals Defines three sets of polynomials,

$$\left\{ \text{el}^{i,j}(\xi,\eta) \,\middle|\, i \in \{1,2,...,N\}, \ j \in \{0,1,...,N\} \right\}, \tag{2.26a}$$

$$\left\{ \text{le}^{i,j}(\xi,\eta) \,\middle|\, j \in \{1,2,...,N\}, \ i \in \{0,1,...,N\} \right\}, \tag{2.26b}$$

where

$$\text{el}^{i,j}(\xi,\eta) = e^i(\xi) l^j(\eta),$$
$$\text{le}^{i,j}(\xi,\eta) = l^i(\xi) e^j(\eta).$$

The face polynomials satisfy line integral Kronecker delta properties:

$$\int_{([\xi_{l-1},\xi_l],\eta_m)} \text{el}^{i,j}(\xi,\eta) dr = \int_{\xi_{l-1}}^{\xi_l} e^i(\xi) d\xi \, l^j(\eta_m) = \delta_{l,m}^{i,j}, \tag{2.27a}$$

$$\int_{(\xi_l,[\eta_{m-1},\eta_m])} \text{le}^{i,j}(\xi,\eta) dr = l^i(\xi_l) \int_{\eta_{m-1}}^{\eta_m} e^j(\eta) d\eta = \delta_{l,m}^{i,j}, \tag{2.27b}$$

and the function space spanned by face polynomials is defined as:

$$\text{FP}_{N-1}(\Omega_{\text{ref}}) = \text{span}\left(\left\{ \text{el}^{i,j}(\xi,\eta) \,\middle|\, i \in \{1,2,...,N\}, \ j \in \{0,1,...,N\} \right\} \right)$$
$$\times \text{span}\left(\left\{ \text{le}^{i,j}(\xi,\eta) \,\middle|\, j \in \{1,2,...,N\}, \ i \in \{0,1,...,N\} \right\} \right). \tag{2.28}$$

Volume polynominals Defines a set of polynomials,

$$\left\{ \text{ee}^{i,j}(\xi,\eta) \,\middle|\, i,j \in \{1,2,...,N\} \right\}, \tag{2.29}$$

where

$$\text{ee}^{i,j}(\xi,\eta) = e^i(\xi) e^j(\eta).$$

The volume polynomials satisfy integral Kronecker delta properties:

$$\int_{([\xi_{l-1},\xi_l],[\eta_{m-1},\eta_m])} \text{ee}^{i,j}(\xi,\eta) dr = \int_{\xi_{l-1}}^{\xi_l} e^i(\xi) d\xi \int_{\eta_{m-1}}^{\eta_m} e^j(\eta) d\eta = \delta_{l,m}^{i,j}, \tag{2.30a}$$

and the function space spanned by face polynomials is defined as:

$$\text{VP}_{N-1}(\Omega_{\text{ref}}) = \text{span}\left(\left\{ \text{ee}^{i,j}(\xi,\eta) = \,\middle|\, i,j \in \{1,2,...,N\} \right\} \right). \tag{2.31}$$

2.1.5. Coordinates transformation

Finally, the polynomials in the reference domain need to be mapped into the real domain. The mapping of coordinate from Ω_{ref} to Ω can be expressed as

$$(x, y) = \boldsymbol{\Phi}(\xi, \eta) = (\Phi_x(\xi, \eta), \Phi_y(\xi, \eta)). \tag{2.32}$$

The Jacobian matrix is

$$\mathcal{J} = \begin{bmatrix} \frac{\partial x}{\partial \xi} & \frac{\partial x}{\partial \eta} \\ \frac{\partial y}{\partial \xi} & \frac{\partial y}{\partial \eta} \end{bmatrix}, \tag{2.33}$$

and the Jacobian of mapping is $\det(\mathcal{J})$. And the metric matrix,

$$\mathcal{G} = \mathcal{J}^{\mathsf{T}} \mathcal{J} = \begin{bmatrix} g_{1,1} & g_{1,2} \\ g_{2,1} & g_{2,2} \end{bmatrix}, \tag{2.34}$$

so the metric of mapping is

$$g = \det(G) = [\det(\mathcal{J})]^2 \tag{2.35}$$

.

Define $\boldsymbol{\Phi}^{-1}(x, y)$ as the function mapping coordinates from Ω back to Ω_{ref}, and the jacobian matrix of the inverse mapping is the inverse of the jacobian matrix of the primal mapping:

$$\mathcal{J}^{-1} = \begin{bmatrix} \frac{\partial \xi}{\partial x} & \frac{\partial \xi}{\partial y} \\ \frac{\partial \eta}{\partial x} & \frac{\partial \eta}{\partial y} \end{bmatrix} = \frac{1}{\det(\mathcal{J})} \begin{bmatrix} \frac{\partial y}{\partial \eta} & -\frac{\partial x}{\partial \eta} \\ -\frac{\partial y}{\partial \xi} & \frac{\partial x}{\partial \xi} \end{bmatrix}. \tag{2.36}$$

And the inverse metric matrix is

$$\mathcal{G}^{-1} = \mathcal{J}^{-1}(\mathcal{J}^{-1})^{\mathsf{T}} = \begin{bmatrix} g^{1,1} & g^{1,2} \\ g^{2,1} & g^{2,2} \end{bmatrix}. \tag{2.37}$$

Therefore, the polynominals in a general 2D domain Ω [8] can be derived as following:

Edge polynominals

$$\|_{\boldsymbol{\Phi}}^{i,j}(x, y) = \|^{i,j}(\boldsymbol{\Phi}^{-1}(x, y)), \ i, j \in \{0, 1, \dots N\}. \tag{2.38}$$

Face polynominals

$$\mathbf{el}_{\boldsymbol{\Phi}}^{i,j}(x, y) = (\mathcal{J}^{-1})^{\mathsf{T}} \begin{bmatrix} \mathbf{el}^{i,j}(\boldsymbol{\Phi}^{-1}(x, y)) \\ 0 \end{bmatrix}, \ i \in \{1, 2, \dots N\}, \ j \in \{0, 1, \dots N\}, \tag{2.39a}$$

$$\mathbf{le}_{\boldsymbol{\Phi}}^{i,j}(x, y) = (\mathcal{J}^{-1})^{\mathsf{T}} \begin{bmatrix} 0 \\ \mathbf{le}^{i,j}(\boldsymbol{\Phi}^{-1}(x, y)) \\ 0 \end{bmatrix}, \ j \in \{1, 2, \dots N\}, \ i \in \{0, 1, \dots N\}. \tag{2.39b}$$

Volume polynominals

$$\mathbf{ee}_{\boldsymbol{\Phi}}^{i,j}(x, y) = \frac{1}{\det(\mathcal{J})} \mathbf{ee}^{i,j}(\boldsymbol{\Phi}^{-1}(x, y)), \ i, j \in \{1, 2, \dots N\}. \tag{2.40}$$

2.1.6. Discrete function spaces in MSEM

Therefore, the de Rham complex of discrete function spaces used in MSEM can be written as:

$$\begin{array}{ccc} \text{EP}_N(\Omega) & \subset & H(\text{curl}; \Omega) \\ \downarrow \nabla \times & & \downarrow \nabla \times \\ \text{FP}_{N-1}(\Omega) & \subset & H(\text{div}; \Omega) \\ \downarrow \nabla \cdot & & \downarrow \nabla \cdot \\ \text{VP}_{N_1}(\Omega) & \subset & L^2(\Omega), \end{array} \tag{2.41}$$
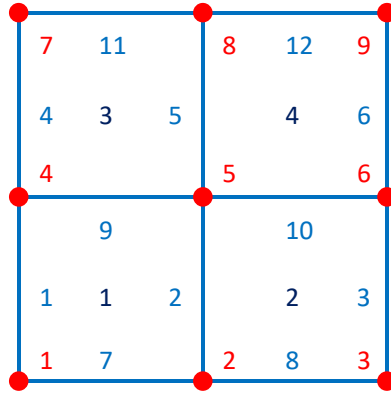
Figure 2.4: Numbering of the geometric elements in a 2nd-order element, where red numbers for edges, blue numbers for faces and black numbders for volumes.

and the *reconstruction* can be implemented as following:

$$\omega^h(x,y) = \sum_{i=0}^{N} \sum_{j=0}^{N} \omega_{i,j} \mathbb{I}_{\boldsymbol{\Phi}}^{i,j}(x,y), \tag{2.42}$$

where $\omega^h \in \mathrm{EP}_N(\Omega)$ and $\omega_{i,j}$ are the degrees of freedom associated to grid edges;

$$\boldsymbol{u}^h(x,y) = \sum_{i=0}^{N} \sum_{j=1}^{N} u_{i,j}^{\xi} \mathbf{le}_{\boldsymbol{\Phi}}^{i,j}(x,y)$$
$$+ \sum_{i=1}^{N} \sum_{j=0}^{N} u_{i,j}^{\eta} \mathbf{el}_{\boldsymbol{\Phi}}^{i,j}(x,y), \tag{2.43}$$

where $\boldsymbol{u}^h \in \mathrm{FP}_{N-1}(\Omega)$ and $u_{i,j}^{\xi}$ and $u_{i,j}^{\eta}$ are the degrees of freedom associated to grid faces;

$$f^h(x,y) = \sum_{i=1}^{N} \sum_{j=1}^{N} f_{i,j} \mathbf{ee}_{\boldsymbol{\Phi}}^{i,j}(x,y), \tag{2.44}$$

where $f^h \in \mathrm{VP}_{N-1}(\Omega)$ and $f_{i,j}$ are the degrees of freedom associated to grid volumes.

Define incidence matrices $\mathsf{E}_{\mathrm{curl}}$ and $\mathsf{E}_{\mathrm{div}}$ as exact discrete counterparts of gradient, curl, and divergence operators applied to polynomial expansion coefficients:

$$\underline{u} = \mathsf{E}_{\mathrm{curl}}\underline{\omega}, \tag{2.45a}$$
$$\underline{f} = \mathsf{E}_{\mathrm{div}}\underline{u}, \tag{2.45b}$$

where $\underline{u}$, $\underline{\omega}$ and $\underline{f}$ are the vector of expansion coefficients, see also (2.23). Take a 2nd-order element as an example, where the numberings of the geometry elements are shown in Fig. 2.4, the incidence matrices

E_{curl} and E_{div} are

$$E_{curl} = \begin{bmatrix} -1 & 0 & 0 & 1 & 0 & 0 & 0 & 0 & 0 \\ 0 & -1 & 0 & 0 & 1 & 0 & 0 & 0 & 0 \\ 0 & 0 & -1 & 0 & 0 & 1 & 0 & 0 & 0 \\ 0 & 0 & 0 & -1 & 0 & 0 & 1 & 0 & 0 \\ 0 & 0 & 0 & 0 & -1 & 0 & 0 & 1 & 0 \\ 0 & 0 & 0 & 0 & 0 & -1 & 0 & 0 & 1 \\ 1 & -1 & 0 & 0 & 0 & 0 & 0 & 0 & 0 \\ 0 & 1 & -1 & 0 & 0 & 0 & 0 & 0 & 0 \\ 0 & 0 & 1 & -1 & 0 & 0 & 0 & 0 & 0 \\ 0 & 0 & 0 & 1 & -1 & 0 & 0 & 0 & 0 \\ 0 & 0 & 0 & 0 & 1 & -1 & 0 & 0 & 0 \\ 0 & 0 & 0 & 0 & 0 & 1 & -1 & 0 & 0 \\ 0 & 0 & 0 & 0 & 0 & 0 & 1 & -1 & 0 \\ 0 & 0 & 0 & 0 & 0 & 0 & 0 & 1 & -1 \end{bmatrix}, \tag{2.46}$$

$$E_{div} = \begin{bmatrix} -1 & 1 & 0 & 0 & 0 & 0 & -1 & 0 & 1 & 0 & 0 & 0 \\ 0 & -1 & 1 & 0 & 0 & 0 & 0 & -1 & 0 & 1 & 0 & 0 \\ 0 & 0 & -1 & 1 & 0 & 0 & 0 & 0 & -1 & 0 & 1 & 0 \\ 0 & 0 & 0 & -1 & 1 & 0 & 0 & 0 & 0 & -1 & 0 & 1 \end{bmatrix}. \tag{2.47}$$

And the relation between mimetic polynominal spaces for domain Ω can be written as

$$\begin{aligned} \nabla \times \omega^h \in \mathsf{FP}_{N-1}(\Omega) \quad \forall \omega^h \in \mathsf{EP}_N(\Omega), \\ \nabla \cdot \boldsymbol{u}^h \in \mathsf{VP}_{N-1}(\Omega) \quad \forall \boldsymbol{u}^h \in \mathsf{FP}_{N-1}(\Omega). \end{aligned} \tag{2.48}$$

2.2. Hybridization and Dual function spaces

Although the advantage of high-order accuracy and structure-preserving ability has been proven for the mimetic spectral element method, the MSEM still needs to be more efficient. Because the MSEM of high order always leads to a global matrix that is not sparse and consumes huge computing resources. For FEM-like discrete methods, hybridization is an effective method for domain decomposition [35, 25]. It decomposes the global problem into multiple subproblems, which effectively increases the sparsity of the matrix and provides the feasibility of parallel computing. The MSEM with hybridization is called the hybrid mimetic spectral element method (hMSEM). In addition, properly designing a dual grid and dual function spaces [43] for hMSEM can further increase the sparsity of the matrix and achieve higher computing efficiency.

This section will present the approach to hybridizing and designing dual function spaces for MSEM. Besides, the problems that arise from hybridization and dual function spaces are discussed.

2.2.1. Mimetic trace spaces in hMSEM

First, a set of mimetic spaces and polynomials in the reference domain of $\mathbb{R}^1$ can be given similarly to the case in the 2D domain presented in the previous chapter.

Here, set a reference domain of $\mathbb{R}^1$ as $\Pi_{\mathsf{ref}} = [-1, 1]$, and choose a set of nodes,

$$\{\varrho_0, \varrho_1, \dots, \varrho_N\},$$

where $-1 = \varrho_0 < \varrho_1 < \cdots < \varrho_N = 1$. And the basis mimetic polynomials in trace space are Lagrange polynomials (2.12) and edge polynomials (2.14) in $\mathbb{R}^1$.

$$l^i(\varrho) \quad i \in \{0, 1, \dots, N\}, \tag{2.49a}$$
$$e^i(\varrho) \quad i \in \{1, 2, \dots, N\}. \tag{2.49b}$$

So the discrete spaces spanned by mimetic polynomials in $\mathbb{R}^1$ can be spanned as

$$\mathsf{TE}_N(\Pi_{\mathsf{ref}}) = \mathsf{span}\left(\{l^i(\varrho)|\ i \in \{0, 1, \dots, N\}\}\right), \tag{2.50a}$$

$$\mathsf{TF}_{N-1}(\Pi_{\mathsf{ref}}) = \mathsf{span}\left(\{e^i(\varrho)|\ i \in \{1, 2, \dots, N\}\}\right). \tag{2.50b}$$

Then, the coordinates transformation must also be considered when mapping from the reference trace domain to the general trace domain. For a domain in $\mathbb{R}^2$, the trace domain Γ is a 1D line over the boundary. Considering a smooth mapping Ψ,

$$(x, y) = \Psi(\varrho) = \left(\Psi_x(\varrho), \Psi_y(\varrho)\right),$$

there is

$$\mathcal{J} = \left[\begin{array}{c} \frac{\partial x}{\partial \varrho} \\ \frac{\partial y}{\partial \varrho} \end{array}\right]. \tag{2.51}$$

And the metric matrix is

$$\mathcal{G} = g = \mathcal{J}^{\mathsf{T}}\mathcal{J}, \tag{2.52}$$

where g is the metric of the mapping is the determinant of the metric matrix,

$$g = \mathsf{det}(\mathcal{G}). \tag{2.53}$$

So the basis mimetic polynomials in general trace domain Γ are

$$\mathsf{l}^i_\Psi(\Psi(\varrho)) = l^i(\varrho), \tag{2.54a}$$

$$\mathsf{e}^i_\Psi(\Psi(\varrho)) = \frac{1}{\sqrt{g}}e^i(\varrho), \tag{2.54b}$$

and the trace spaces for Γ can be defined as

$$\mathsf{TE}_N(\Gamma) = \mathsf{span}\left(\{\mathsf{l}^i_\Psi(\Psi(\varrho))|\ i \in \{0, 1, \dots, N\}\}\right), \tag{2.55a}$$

$$\mathsf{TF}_{N-1}(\Gamma) = \mathsf{span}\left(\{\mathsf{e}^i_\Psi(\Psi(\varrho))|\ i \in \{1, 2, \dots, N\}\}\right). \tag{2.55b}$$

Therefore, the discrete trace functions can be reconstructed as follows:

$$\alpha^h = \sum_{i=0}^{N} a_{i,j}\mathsf{l}^i_\Psi(x, y), \tag{2.56}$$

where $\alpha^h \in \mathsf{TE}_N(\Gamma)$, and $a_i \in \underline{\mathsf{TE}}_N(\Gamma)$ are expansion coefficients;

$$\gamma^h = \sum_{i=1}^{N} \gamma_i \mathsf{e}^i_\Psi(x, y), \tag{2.57}$$

where $\gamma^h \in \mathsf{TF}_{N-1}(\Gamma)$, and $\gamma_{i,j} \in \underline{\mathsf{TF}}_{N-1}(\Gamma)$ are expansion coefficients.

2.2.2. Trace operator

Considering a cubic domain Ω in $\mathbb{R}^2$, there are 4 trace domains, $\Gamma^\Phi_{\xi^-}$, $\Gamma^\Phi_{\xi^+}$, $\Gamma^\Phi_{\eta^-}$ and $\Gamma^\Phi_{\eta^+}$ on each surface of the square domain Ω, illustrated in Fig. 2.5.

Therefore, the trace spaces for $\partial\Omega$ can be written as

$$\mathsf{TE}_N(\partial\Omega) = \mathsf{TN}_N(\Gamma^\Phi_{\xi^-}) \cup \mathsf{TN}_N(\Gamma^\Phi_{\xi^+}) \cup \mathsf{TN}_N(\Gamma^\Phi_{\eta^-}) \cup \mathsf{TN}_N(\Gamma^\Phi_{\eta^+}), \tag{2.58a}$$

$$\mathsf{TF}_{N-1}(\partial\Omega) = \mathsf{TF}_{N-1}(\Gamma^\Phi_{\xi^-}) \cup \mathsf{TF}_{N-1}(\Gamma^\Phi_{\xi^+}) \cup \mathsf{TE}_{N-1}(\Gamma^\Phi_{\eta^-}) \cup \mathsf{TF}_{N-1}(\Gamma^\Phi_{\eta^+}). \tag{2.58b}$$

In hMSEM, ones can expect $\gamma^h = \boldsymbol{u}^h \cdot \boldsymbol{n} \in \mathsf{TF}_{N-1}(\partial\Omega)$. Here, a trace operator can be defined to transfer $\boldsymbol{u}^h$ to γ^h,

$$T\boldsymbol{u}^h = \gamma^h. \tag{2.59}$$

Figure 2.5: Trace domains on a general 2D domain

And in discrete systems,

$$\underline{\gamma} = \mathbb{T}_F \underline{u}, \tag{2.60}$$

where $\mathbb{T}_F$ is the matrix for the trace operator. As long as the order of the mimetic polynomials and trace polynomials are the same, $\mathbb{T}_F$ only consists of entries of 1, -1 and 0.

Similarly, the discrete function $\omega^h \in \mathsf{EP}_N(\Omega)$ can be mapped into $\mathsf{TE}_N(\Omega)$ as

$$T^{\|}\omega^h = \omega^h \times \boldsymbol{n}, \tag{2.61}$$

where n_ζ is defined as the outward unit normal vector to the boundary of the subdomain. The discrete form

$$\underline{\beta} = \mathbb{T}_E \underline{\omega}. \tag{2.62}$$

Take a 2nd-order element with trace dofs, shown in Fig.2.6, as an example, the trace matrices $\mathbb{T}_F$ and $\mathbb{T}_E$ are

$$\mathbb{T}_F = \begin{bmatrix} -1 & 0 & 0 & 0 & 0 & 0 & 0 & 0 & 0 & 0 & 0 & 0 \\ 0 & 0 & 0 & -1 & 0 & 0 & 0 & 0 & 0 & 0 & 0 & 0 \\ 0 & 0 & 1 & 0 & 0 & 0 & 0 & 0 & 0 & 0 & 0 & 0 \\ 0 & 0 & 0 & 0 & 0 & 1 & 0 & 0 & 0 & 0 & 0 & 0 \\ 0 & 0 & 0 & 0 & 0 & 0 & -1 & 0 & 0 & 0 & 0 & 0 \\ 0 & 0 & 0 & 0 & 0 & 0 & 0 & -1 & 0 & 0 & 0 & 0 \\ 0 & 0 & 0 & 0 & 0 & 0 & 0 & 0 & 0 & 0 & 1 & 0 \\ 0 & 0 & 0 & 0 & 0 & 0 & 0 & 0 & 0 & 0 & 0 & 1 \end{bmatrix}, \tag{2.63}$$

Figure 2.6: Numbering of geometric elements in a 2nd-order element with trace degrees of freedom, where red numbers for edges, blue numbers for faces, green numbers for trace edges and black numbders for trace faces.

$$
\mathbb{T}_{\mathsf{E}} = \begin{bmatrix}
1 & 0 & 0 & 0 & 0 & 0 & 0 & 0 & 0 \\
0 & 0 & 0 & 1 & 0 & 0 & 0 & 0 & 0 \\
0 & 0 & 0 & 0 & 0 & 0 & 1 & 0 & 0 \\
0 & 0 & -1 & 0 & 0 & 0 & 0 & 0 & 0 \\
0 & 0 & 0 & 0 & 0 & -1 & 0 & 0 & 0 \\
0 & 0 & 0 & 0 & 0 & 0 & 0 & 0 & -1 \\
-1 & 0 & 0 & 0 & 0 & 0 & 0 & 0 & 0 \\
0 & -1 & 0 & 0 & 0 & 0 & 0 & 0 & 0 \\
0 & 0 & -1 & 0 & 0 & 0 & 0 & 0 & 0 \\
0 & 0 & 0 & 0 & 0 & 0 & 1 & 0 & 0 \\
0 & 0 & 0 & 0 & 0 & 0 & 0 & 1 & 0 \\
0 & 0 & 0 & 0 & 0 & 0 & 0 & 0 & 1
\end{bmatrix}, \tag{2.64}
$$

where the positive sign of $\underline{\omega}$ stands for the vector outward to the paper plane and the the positive sign of $\underline{u}$ stands for the positive direction of coordinate ξ and η. Therefore, the non-zero entry in the trace operator can be either -1 or 1, depending on the angle between the outward normal vector $\boldsymbol{n}$ at face and the local coordinate $\xi - \eta$.

The trace operator can also be used to transform the function space,

$$
\mathsf{TF}_{N-1}(\partial\Omega) = T(\mathsf{FP}_{N-1}(\Omega)), \tag{2.65a}
$$

$$
\mathsf{TE}_{N}(\partial\Omega) = T^{\parallel}(\mathsf{EP}_{N}(\Omega)). \tag{2.65b}
$$

2.2.3. Application of hMSEM in Stokes Equations

An example is given to illustrate how to use hMSEM for domain decomposition. Consider the Stokes equations and divide the global domain Ω into M discontinuous sub-domains, Ω_i, $i = \{1, 2, ..., M\}$ and set $\Gamma_{i,j}$ as the interface (trace domains) between sub-domains ω_i and Ω_j,

$$
\Gamma_{i,j} = \Gamma_{j,i} = \partial\Omega_i \cap \partial\Omega_j. \tag{2.66}
$$

and denote $\boldsymbol{n}_i$ and $\boldsymbol{n}_j$ as the outward unit normal vector of domain Ω_i and Ω_j respectively. Then, the strong continuity constraint in the decomposed domain is presented in Fig. 2.7.
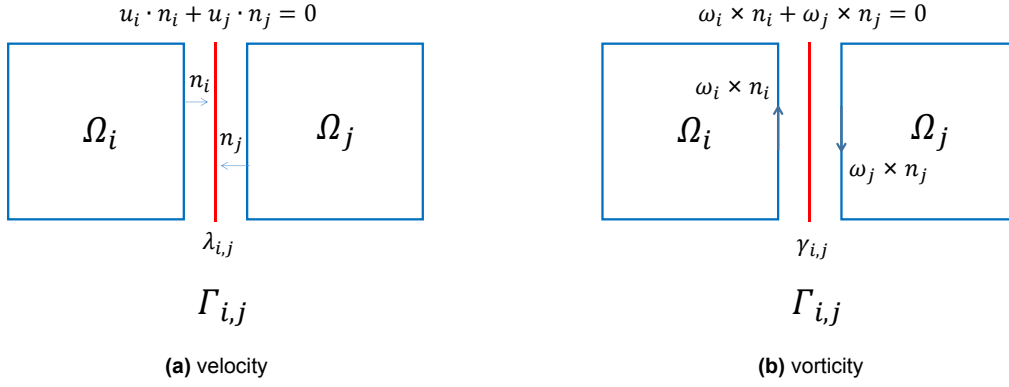
Figure 2.7: Illustration of domain decomposition

Consider a Stokes problem in the Velocity-Vorticity-Pressure formulation,

$$\omega - \nabla \times \boldsymbol{u} = 0 \qquad \text{in } \Omega_i, \tag{2.67a}$$

$$\nabla \times \omega + \nabla p = \boldsymbol{f} \qquad \text{in } \Omega_i, \tag{2.67b}$$

$$\nabla \cdot \boldsymbol{u} = 0 \qquad \text{in } \Omega_i, \tag{2.67c}$$

where Ω is a bounded domain in $\mathbb{R}^2$ with boundaries $\partial\Omega = \Gamma_p \cup \Gamma_{\boldsymbol{u}\cdot\boldsymbol{n}} = \Gamma_{\boldsymbol{u}\times\boldsymbol{n}} \cup \Gamma_\omega$, where $\Gamma_p \cap \Gamma_{\boldsymbol{u}\cdot\boldsymbol{n}} = \emptyset$ and $\Gamma_{\boldsymbol{u}\times\boldsymbol{n}} \cap \Gamma_\omega = \emptyset$, and the domain Ω is decomposed into N subdomains Ω_i, $i = 1, 2, \dots N$, and the surface of subdomain Ω_i is denoted as $\partial\Omega_i$.

So the equations at physical boundaries and interface between subdomains are

$$\omega = \hat{\omega} \qquad \text{on } \Gamma_{\hat{\omega}} \cap \partial\Omega_i, \tag{2.68a}$$

$$p = \hat{p} \qquad \text{on } \Gamma_{\hat{p}} \cap \partial\Omega_i, \tag{2.68b}$$

$$\boldsymbol{u} \times \boldsymbol{n} = \hat{\boldsymbol{u}}_\parallel \qquad \text{on } \Gamma_{\hat{\boldsymbol{u}}_\parallel} \cap \partial\Omega_i, \tag{2.68c}$$

$$\boldsymbol{u} \cdot \boldsymbol{n} = \hat{\boldsymbol{u}}_\perp \qquad \text{on } \Gamma_{\hat{\boldsymbol{u}}_\perp} \cap \partial\Omega_i, \tag{2.68d}$$

$$p = -\lambda \qquad \text{on } \Gamma_{i,j}, \tag{2.68e}$$

$$\boldsymbol{u} \cdot \boldsymbol{n}_i + \boldsymbol{u} \cdot \boldsymbol{n}_j = 0 \qquad \text{on } \Gamma_{i,j}, \tag{2.68f}$$

$$\boldsymbol{u} \times \boldsymbol{n} = \gamma \qquad \text{on } \Gamma_{i,j}, \tag{2.68g}$$

$$\omega \times \boldsymbol{n}_i + \omega \times \boldsymbol{n}_j = 0 \qquad \text{on } \Gamma_{i,j}. \tag{2.68h}$$

The variational formulation is presented as follows: Given $f \in [L^2(\Omega)]^2$, $g \in L^2(\Omega)$, $\hat{\boldsymbol{u}} \times \boldsymbol{n} \in TH_{00}^{1/2}(\Gamma_{\boldsymbol{u}\times\boldsymbol{n}})$, $\hat{p} \in H_{00}^{1/2}(\Gamma_p)$, the solution $(\omega, \boldsymbol{u}, p, \gamma, \lambda) \in H_0(\text{curl}, \Omega_i; \Gamma_\omega) \times H_0(\text{div}, \Omega_i; \Gamma_{\boldsymbol{u}\cdot\boldsymbol{n}}) \times L^2(\Omega_i) \times TH_{00}^{1/2}(\partial\Omega_i) \times H_{00}^{1/2}(\partial\Omega_i)$ has

$$\langle \omega, \xi \rangle_{\Omega_i} - \langle \boldsymbol{u}, \nabla \times \xi \rangle_{\Omega_i} - \langle \gamma, \xi \times \boldsymbol{n} \rangle_{\partial\Omega_i} = \langle \xi \times \boldsymbol{n}, \hat{\boldsymbol{u}} \times \boldsymbol{n} \rangle_{\partial\Omega_i \cap \Gamma_{\boldsymbol{u}\times\boldsymbol{n}}} \quad \forall \xi \in H_0(\text{curl}, \Omega; \Gamma_{\hat{\omega}} \cap \partial\Omega_i), \tag{2.69a}$$

$$\langle \nabla \times \omega, \boldsymbol{v} \rangle_{\Omega_i} - \langle p, \nabla \cdot \boldsymbol{v} \rangle_{\Omega_i} + \langle \lambda, \boldsymbol{v} \cdot \boldsymbol{n} \rangle_{\partial\Omega_i} = \langle \boldsymbol{f}, \boldsymbol{v} \rangle_{\Omega_i} - \langle \hat{p}, \boldsymbol{v} \cdot \boldsymbol{n} \rangle_{\partial\Omega \cap \Gamma_p} \quad \forall \boldsymbol{v} \in H_0(\text{div}, \Omega_i; \Gamma_{\boldsymbol{u}\cdot\boldsymbol{n}} \cap \partial\Omega_i), \tag{2.69b}$$

$$\langle \nabla \cdot \boldsymbol{u}, q \rangle_{\Omega_i} = 0 \quad \forall q \in L^2(\Omega_i), \tag{2.69c}$$

$$\langle \omega \times \boldsymbol{n}, \varepsilon \rangle_{\partial\Omega_i} = 0 \quad \forall \varepsilon \in TH_{00}^{1/2}(\partial\Omega_i), \tag{2.69d}$$

$$\langle \boldsymbol{u} \cdot \boldsymbol{n}, \psi \rangle_{\partial\Omega_i} = 0 \quad \forall \psi \in H_{00}^{1/2}(\partial\Omega). \tag{2.69e}$$

Equations (2.69d) and (2.69e) are constraints of strong continuity of vorticity ω and the normal component of u at the interface $\Gamma_{i,j}$, and λ and γ are called the Lagrange multiplier [35].

The discrete form for one sub-domain Ω_i can be written as: Given $f \in \mathrm{VP}_{N-1}(\Omega_i)$, the solution $(\omega^h, \boldsymbol{u}^h, p^h, \gamma^h, \lambda^h) \in \mathrm{EP}_N(\Omega_i) \times \mathrm{FP}_{N-1}(\Omega_i) \times \mathrm{VP}_{N-1}(\Omega_i) \times \mathrm{TE}_N(\partial\Omega_i) \times \mathrm{TF}_{N-1}(\partial\Omega_i)$ has

$$\langle \omega^h, \xi^h \rangle_{\Omega_i} - \langle \boldsymbol{u}^h, \nabla \times \xi^h \rangle_{\Omega_i} - \langle \gamma^h, \xi^h \times \boldsymbol{n} \rangle_{\partial\Omega_i} = 0 \quad \forall \xi^h \in \mathrm{EP}_N(\Omega_i), \tag{2.70a}$$

$$\langle \nabla \times \omega^h, \boldsymbol{v}^h \rangle_{\Omega_i} - \langle p^h, \nabla \cdot \boldsymbol{v}^h \rangle_{\Omega_i} + \langle \lambda^h, \boldsymbol{v}^h \cdot \boldsymbol{n} \rangle_{\partial\Omega_i} = \langle \boldsymbol{f}^h, \boldsymbol{v}^h \rangle_{\Omega_i} \quad \forall \boldsymbol{v}^h \in \mathrm{FP}_{N-1}(\Omega_i), \tag{2.70b}$$

$$\langle \nabla \cdot \boldsymbol{u}^h, q^h \rangle_{\Omega_i} = 0 \quad \forall q^h \in \mathrm{VP}_{N-1}(\Omega_i), \tag{2.70c}$$

$$\langle \omega^h \times \boldsymbol{n}, \varepsilon^h \rangle_{\partial\Omega_i} = 0 \quad \forall \varepsilon^h \in \mathrm{TE}_N(\partial\Omega_i), \tag{2.70d}$$

$$\langle \boldsymbol{u}^h \cdot \boldsymbol{n}, \psi^h \rangle_{\partial\Omega_i} = 0 \quad \forall \psi^h \in \mathrm{TF}_{N-1}(\partial\Omega). \tag{2.70e}$$

For convenience, the matrix format can be written as

$$\begin{bmatrix} \mathsf{M}_\mathsf{E} & -\mathsf{E}_{\mathsf{curl}}^\mathsf{T}\mathsf{M}_\mathsf{F} & 0 & \mathbb{T}_\mathsf{E}^\mathsf{T}\mathsf{M}_{\mathsf{TE}} & 0 \\ -\mathsf{M}_\mathsf{F}^\mathsf{T}\mathsf{E}_{\mathsf{curl}} & 0 & \mathsf{E}_{\mathsf{div}}^\mathsf{T}\mathsf{M}_\mathsf{V} & 0 & \mathbb{T}_\mathsf{F}^\mathsf{T}\mathsf{M}_{\mathsf{TF}} \\ 0 & \mathsf{M}_\mathsf{V}^\mathsf{T}\mathsf{E}_{\mathsf{div}} & 0 & 0 & 0 \\ \mathsf{M}_{\mathsf{TE}}^\mathsf{T}\mathbb{T}_\mathsf{E} & 0 & 0 & 0 & 0 \\ 0 & \mathsf{M}_{\mathsf{TF}}^\mathsf{T}\mathbb{T}_\mathsf{F} & 0 & 0 & 0 \end{bmatrix} \begin{bmatrix} \underline{\omega} \\ \underline{\boldsymbol{u}} \\ \underline{p} \\ \underline{\gamma} \\ \underline{\lambda} \end{bmatrix} = \begin{bmatrix} 0 \\ -\mathsf{M}_\mathsf{V}\underline{\boldsymbol{f}} \\ 0 \\ 0 \\ 0 \end{bmatrix}. \tag{2.71}$$

To demonstrate the local matrix system conveniently, denote the system (2.71) as

$$\begin{bmatrix} A & B \\ C & D \end{bmatrix} \begin{bmatrix} \underline{\boldsymbol{a}}_i \\ \underline{b}_i \end{bmatrix} = \begin{bmatrix} g \\ h \end{bmatrix}, \tag{2.72}$$

where $\underline{\boldsymbol{a}}_i = [\boldsymbol{\omega} \ \underline{\boldsymbol{u}} \ p]^\mathsf{T}$ and $\underline{b}_i = [\underline{\gamma} \ \underline{\lambda}]^\mathsf{T}$.

Denote the solution vector of $\underline{\boldsymbol{a}}_i$ and $\underline{b}_i$ as

$$\underline{\boldsymbol{x}}_i = \begin{bmatrix} \underline{\boldsymbol{a}}_i \\ \underline{b}_i \end{bmatrix}, \tag{2.73}$$

where i stands for the index of sub-domain Ω_i, then a reduced system for $\underline{b}_i$ can be derived with Schur complement technique:

$$(D - CA^{-1}B)\underline{b}_i = h - CA^{-1}g. \tag{2.74}$$

Generally speaking, the degrees of freedom in one sub-domain are of limited size, so the local matrix A inverse can be calculated directly. Assemble equations (2.74) of all sub-domains, and insert the boundary conditions correctly, the $\underline{b}_i$ can be solved, and then compute $\underline{\boldsymbol{a}}_i$ in

$$\underline{\boldsymbol{a}}_i = A^{-1}(g - B\underline{b}_i). \tag{2.75}$$

For step (2.74) and (2.75), the computation can be done locally in parallel, and only in solving $\underline{b}_i$, the solver needs to solve a global system. Although solving a global system is inevitable, the global system degrees of freedom to be solved in high-order hMSEM are much smaller than in MSEM. The proof can be found in the study of Zhang [44]:

2.2.4. Dual mimetic spaces for hMSEM

As the hybrid MSEM has been illustrated in previous sections, a set of dual grid and dual basis polynomials can be designed to increase the sparsity of the matrix further and improve computing efficiency. The hMSEM that employs the dual mimetic spaces is called the hybrid dual mimetic spectral element method (hdMSEM) [43, 10].

The starting point for using dual mimetic space is simple. Take system (2.71) for example; it can be

rewritten as

$$
\begin{bmatrix}
\mathsf{M_E} & -\mathsf{E_{curl}^T}\mathsf{M_F} & 0 & \mathbb{T}_\mathsf{E}^\mathsf{T} & 0 \\
-\mathsf{M_F^T}\mathsf{E_{curl}} & 0 & \mathsf{E_{div}^T} & 0 & \mathbb{T}_\mathsf{F}^\mathsf{T} \\
0 & \mathsf{E_{div}} & 0 & 0 & 0 \\
\mathbb{T}_\mathsf{E} & 0 & 0 & 0 & 0 \\
0 & \mathbb{T}_\mathsf{F} & 0 & 0 & 0
\end{bmatrix}
\begin{bmatrix}
\underline{\omega} \\
\underline{u} \\
\mathsf{M_V}\underline{p} \\
\mathsf{M_{TE}}\underline{\gamma} \\
\mathsf{M_{TF}}\underline{\lambda}
\end{bmatrix}
=
\begin{bmatrix}
0 \\
-\mathsf{M_V}\underline{f} \\
0 \\
0 \\
0
\end{bmatrix}.
\tag{2.76}
$$

and the left-hand side matrix is sparser than system (2.76). As for $\mathsf{M_E}$ and $\mathsf{M_F}$ which still exist, only the local mass matrices for each subdomain are required to be computed when domain decomposed.

So a set of dual grids and basis functions is expected to be designed such that

$$
\underline{\tilde{p}}_i = \mathsf{M_V}\underline{p}, \quad \underline{\tilde{\gamma}} = \mathsf{M_{TE}}\underline{\gamma} \quad \text{and} \quad \underline{\tilde{\lambda}} = \mathsf{M_{TF}}\underline{\lambda}.
\tag{2.77}
$$

The mimetic spaces can be demonstrated systematically as follows: For a general form of the discrete function q^h, there is

$$
q^h = \sum_i q_i e_i = \sum_i \tilde{q}_i \tilde{e}_i.
\tag{2.78}
$$

And the relation between dual coefficients and primal coefficients should follow

$$
\underline{\tilde{q}} = \mathsf{M}\underline{q},
\tag{2.79}
$$

therefore, the dual basis functions can be derived as

$$
\underline{\tilde{e}} = \mathsf{M}^{-1}\underline{e}.
\tag{2.80}
$$

The dual mimetic spaces are denoted with $\tilde{}$, and the transformation from primal mimetic spaces to dual mimetic spaces is named as Hodege operator, $\star$, for example

$$
\mathsf{FP}_{N-1}(\Omega) \xrightarrow{\star} \widetilde{\mathsf{FP}}_{N-1}(\Omega) \quad \text{and} \quad \widetilde{\mathsf{FP}}_{N-1}(\Omega) \xrightarrow{\star^{-1}} \mathsf{FP}_{N-1}(\Omega).
\tag{2.81}
$$

Thus, the inner product operator between p^h, q^h becomes

$$
\langle p^h, q^h \rangle_\Omega = \underline{p}^\mathsf{T}\underline{\tilde{q}}.
\tag{2.82}
$$

For trace variables, a set of dual trace spaces can be defined in a similar way: For $\psi^h \in NP_N(\Omega)$ and $\alpha^h \in \widetilde{\mathsf{TN}}_N(\partial\Omega)$, the inner product has

For $\omega^h \in \mathsf{EP}_N(\Omega)$ and $\beta^h \in \widetilde{\mathsf{TE}}_N(\partial\Omega)$, the inner product has

$$
\langle \omega^h, \beta^h \rangle_{\partial\Omega} = \int_{\partial\Omega} \omega^h \beta^h d\Gamma = \int_{\partial\Omega} (T^\parallel \omega^h)\beta^h d\Gamma = \underline{\omega}^\mathsf{T}\mathbb{T}_\mathsf{E}^\mathsf{T}\underline{\tilde{\beta}}.
\tag{2.83}
$$

For $u^h \in FP_{N-1}(\Omega)$ and $\lambda^h \in \widetilde{\mathsf{TF}}_{N-1}(\partial\Omega)$, the inner product has

$$
\langle u^h, \lambda^h \rangle_{\partial\Omega} = \int_{\partial\Omega} u^h \lambda^h \Gamma = \int_{\partial\Omega} (T^\parallel u^h)\lambda^h \Gamma = \underline{u}^\mathsf{T}\mathbb{T}_\mathsf{F}^\mathsf{T}\underline{\tilde{\lambda}}.
\tag{2.84}
$$

Since dual variables and dual basis functions are linear compositions of the primal variables and primal basis functions, the total number of degrees of freedom is not changed after applying dual mimetic spaces.

2.2.5. Discrete dual operator

After introducing a set of dual trace variables and mimetic trace spaces, a set of discrete dual operators can be defined as follows:

Discrete dual gradient operator

For the dual gradient operator, there is

$$
\widetilde{\nabla} : L^2(\Omega) \times H^{1/2}(\partial\Omega) \to H(\mathrm{div};\Omega).
\tag{2.85}
$$

The weak form is

$$\langle \boldsymbol{v}, \widetilde{\nabla}\varphi \rangle_\Omega = -\langle \nabla \cdot \boldsymbol{v}, \varphi \rangle_\Omega + \int_{\partial\Omega} \text{tr}(\varphi)(\boldsymbol{v}\cdot\boldsymbol{n})d\Gamma \qquad \forall \boldsymbol{v} \in H(\text{div};\Omega). \tag{2.86}$$

At the discrete level, define

$$\widetilde{\boldsymbol{\psi}}^h = \widetilde{\nabla}\widetilde{\varphi}^h \in \widetilde{\text{FP}}_{N-1}(\Omega),$$

$$\widetilde{\varphi}^h \in \widetilde{\text{VP}}_{N-1}(\Omega),$$

$$\hat{\varphi}^h \in \widetilde{\text{TF}}_{N-1}(\partial\Omega),$$

and there is

$$\langle \boldsymbol{v}^h, \widetilde{\boldsymbol{\psi}}^h \rangle_\Omega = -\langle \nabla \cdot \boldsymbol{v}^h, \widetilde{\varphi}^h \rangle_\Omega + \int_{\partial\Omega} \hat{\varphi}^h(\boldsymbol{v}^h\cdot\boldsymbol{n})d\Gamma \qquad \forall \boldsymbol{v}^h \in \text{FP}_{N-1}(\Omega), \tag{2.87}$$

and the matrix form can be written as

$$\underline{\boldsymbol{v}}^T\underline{\widetilde{\boldsymbol{\psi}}} = -\underline{\boldsymbol{v}}^T\mathsf{E}_{\text{div}}^T\underline{\widetilde{\varphi}} + \mathbb{T}_{\mathsf{F}}^T\underline{\hat{\varphi}} \qquad \forall\underline{\boldsymbol{v}} \in \underline{\text{FP}}_{N-1}(\Omega). \tag{2.88}$$

Discrete dual curl operator

Similar with the dual gradient operator, the dual curl operator is

$$\widetilde{\nabla\times} : H(\text{div};\Omega) \times TH_\perp(\partial\Omega) \to H(\text{div};\Omega), \tag{2.89}$$

and the weak form can be written as

$$\langle \xi, \widetilde{\nabla\times}\boldsymbol{u} \rangle_\Omega = \langle \nabla \times \xi, \boldsymbol{u} \rangle_\Omega - \int_{\partial\Omega} \xi\text{tr}(\boldsymbol{u}\times\boldsymbol{n})d\Gamma \qquad \forall\xi \in H(\text{curl};\Omega). \tag{2.90}$$

Different from the discrete dual gradient operator, in this thesis, ξ^h and $\widetilde{\nabla\times}\boldsymbol{u}^h$ are both in $\text{EP}_N(\Omega)$ rather than the dual mimetic space $\widetilde{\text{EP}}_N(\Omega)$. Therefore, define

$$\omega^h = \widetilde{\nabla\times}\boldsymbol{u}^h \in \text{EP}_N(\Omega),$$

$$\boldsymbol{u}^h \in \text{FP}_{N-1}(\Omega),$$

$$\hat{\boldsymbol{u}}^h \in \widetilde{\text{TF}}_{N-1}(\partial\Omega),$$

there is

$$\langle \xi^h, \omega^h \rangle_\Omega = \langle \nabla \times \xi^h, \boldsymbol{u}^h \rangle_\Omega - \int_{\partial\Omega} (T_\|\xi^h)\cdot\hat{u}d\Gamma \qquad \forall\xi^h \in \text{EP}_N(\Omega), \tag{2.91}$$

and the corresponding matrix form,

$$\underline{\xi}^\mathsf{T}\mathsf{M}_\mathsf{E}\underline{\omega} = \underline{\xi}^\mathsf{T}\mathsf{E}_{\text{curl}}^\mathsf{T}\mathsf{M}_\mathsf{F}\underline{\boldsymbol{u}} - \underline{\xi}^\mathsf{T}\mathbb{T}_\mathsf{E}^\mathsf{T}\underline{\hat{u}} \qquad \forall\underline{\xi} \in \underline{\text{EP}}_N(\Omega). \tag{2.92}$$

Therefore $\underline{\omega}$ can be calculated as

$$\underline{\omega} = \mathsf{M}_\mathsf{E}^{-1}(E_{\text{curl}}^\mathsf{T}\mathsf{M}_\mathsf{F}\underline{\boldsymbol{u}} - \mathbb{T}_\mathsf{E}^\mathsf{T}\underline{\hat{u}}). \tag{2.93}$$

2.2.6. Problems to solve for the hdMSEM

The hdMSEM has been successfully used to solve Poisson and linear elasticity problems [43, 44]. However, when solving Stokes equations, hdMSEM can cause singularity problems [10].

Consider the matrix format of the linear system of Stokes equations in the hdMSEM,

$$\begin{bmatrix} \mathsf{M}_\mathsf{E} & -\mathsf{E}_{\text{curl}}^\mathsf{T}\mathsf{M}_\mathsf{F} & 0 & \mathbb{T}_\mathsf{E}^\mathsf{T} & 0 \\ -\mathsf{M}_\mathsf{F}^\mathsf{T}\mathsf{E}_{\text{curl}} & 0 & \mathsf{E}_{\text{div}}^\mathsf{T} & 0 & \mathbb{T}_\mathsf{F}^\mathsf{T} \\ 0 & \mathsf{E}_{\text{div}} & 0 & 0 & 0 \\ \mathbb{T}_\mathsf{E} & 0 & 0 & 0 & 0 \\ 0 & \mathbb{T}_\mathsf{F} & 0 & 0 & 0 \end{bmatrix} \begin{bmatrix} \underline{\omega} \\ \underline{\boldsymbol{u}} \\ \underline{\tilde{p}} \\ \underline{\tilde{\gamma}} \\ \underline{\tilde{\lambda}} \end{bmatrix} = \begin{bmatrix} 0 \\ -\underline{\tilde{\boldsymbol{f}}} \\ 0 \\ 0 \\ 0 \end{bmatrix}. \tag{2.94}$$

This system is singular since $\mathbb{T}_E$ is not surjective, i.e.,

$$
\mathbb{T}_E = \begin{bmatrix}
... & ... & 0 & ... & ... \\
... & 0 & 1 & 0 & ... \\
... & 0 & 1 & 0 & ... \\
... & ... & 0 & ... & ...
\end{bmatrix}.
\tag{2.95}
$$

There is a more intuitive way to understand this problem: The discrete Lagrange multiplier,

$$
\mathbb{T}_E\underline{\omega} = 0,
\tag{2.96}
$$

is used to couple degrees of the freedom at edges. For instance, consider an edge where four elements come together, illustrated in Fig. 2.8, the Lagrange multiplier at four trace faces (black lines) couples degrees of freedom at edge bordered with each other (red node), i.e.,

$$
\begin{aligned}
\omega_1 - \omega_2 &= 0, \\
\omega_2 - \omega_3 &= 0, \\
\omega_3 - \omega_4 &= 0, \\
\omega_4 - \omega_1 &= 0.
\end{aligned}
\tag{2.97}
$$

Obviously, one coupling equation is redundant.
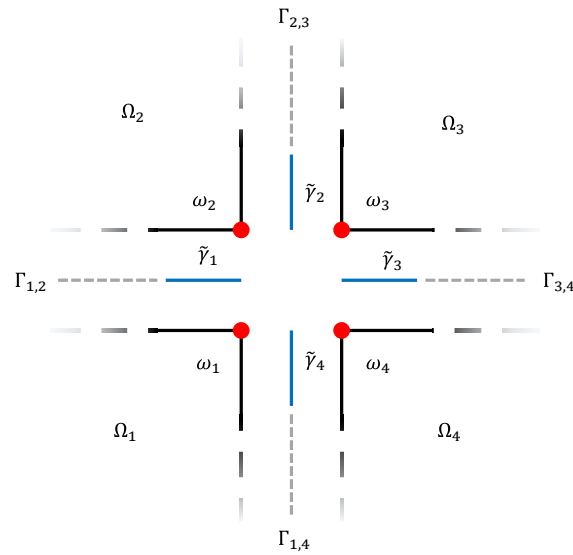
Figure 2.8: Dual grid at the corner where four elements meet: Blue lines stand for dual trace degrees of freedom $\underline{\tilde{\gamma}} \in \widetilde{\underline{\mathrm{TE}}}_N(\Gamma_i)$; red nodes stand for degrees of freedom $\underline{\omega} \in \underline{\mathrm{EP}}_N(\Gamma_i)$ [10]

Zhang gave a solution in a preliminary study [10]. A dummy degree of freedom is introduced at the corner where elements meet, illustrated in Fig. 2.9. And the four equation systems at corner (2.97) can be rewritten as

$$
\begin{aligned}
\omega_1 - \omega_c &= 0, \\
\omega_2 - \omega_c &= 0, \\
\omega_3 - \omega_c &= 0, \\
\omega_4 - \omega_c &= 0.
\end{aligned}
\tag{2.98}
$$

And discrete equations of Lagrange multiplier,

$$
\mathbb{T}_E\underline{\omega} = 0,
$$
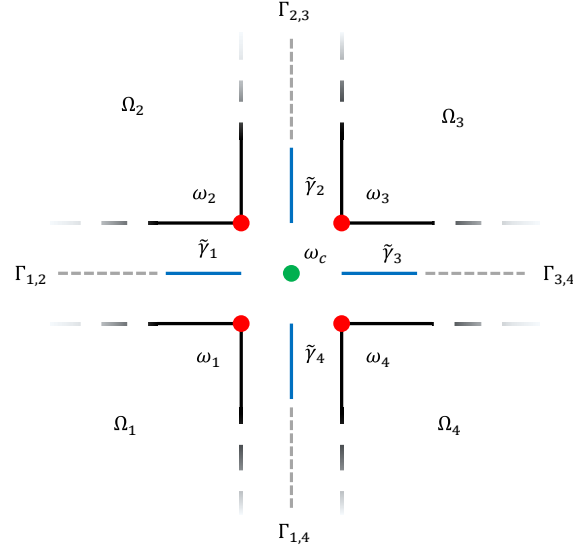
Figure 2.9: Dual grid at the corner where four elements meet: Blue lines stand for trace degrees of freedom $\tilde{\underline{\gamma}} \in \widetilde{\underline{\mathsf{TE}}}_N(\Gamma_i)$; red nodes stand for degrees of freedom $\underline{\omega} \in \underline{\mathsf{EP}}_N(\Gamma_i)$; green node stands for the dummy degree of freedom $\underline{\omega_c} \in \mathsf{EP}_N(\Omega_c)$ [10].

can be rewritten as

$$\mathbb{T}'_E \underline{\omega} + \mathbb{D}^\mathsf{T} \underline{\omega_c} = 0.$$

The matrix formulation of the linear system can be written as

$$
\begin{bmatrix}
M_E & -E_{curl}^\mathsf{T} M_F & 0 & \mathbb{T}_E^\mathsf{T} & 0 & 0 \\
-M_F^\mathsf{T} E_{curl} & 0 & E_{div}^\mathsf{T} & 0 & \mathbb{T}_F^\mathsf{T} & 0 \\
0 & E_{div} & 0 & 0 & 0 & 0 \\
\mathbb{T}'_E & 0 & 0 & 0 & 0 & \mathbb{D}^\mathsf{T} \\
0 & \mathbb{T}_F & 0 & 0 & 0 & 0 \\
0 & 0 & 0 & \mathbb{D} & 0 & 0
\end{bmatrix}
\begin{bmatrix}
\underline{\omega} \\
\underline{u} \\
\underline{\tilde{p}} \\
\underline{\tilde{\gamma}} \\
\underline{\tilde{\lambda}} \\
\underline{\omega_c}
\end{bmatrix}
=
\begin{bmatrix}
0 \\
-\underline{\tilde{f}} \\
0 \\
0 \\
0 \\
0
\end{bmatrix}.
\tag{2.99}
$$

However, this preliminary solution has two glaring disadvantages: 1. The left-hand matrix of the discrete system is asymmetric, which has numerous disadvantages compared to a real symmetric matrix when solving a linear system, such as introducing asymmetric errors into the solution or slowing the convergence [50, 51]; 2. The matrix equations, $\mathbb{T}'_E \underline{\omega} + \mathbb{D}^\mathsf{T} \underline{\omega_c} = 0$ and $\mathbb{D}\tilde{\gamma} = 0$, does not have rigorous mathematical definition in the framework of hybrid finite element method, and results in issues in verifying the discrete conservation law and implementing the physical boundary conditions.

Hybrid Dual Mimetic Spectral Element Method with a Novel Dual Grid

This chapter proposes the hdMSEM with a novel dual grid. We firstly propose a novel dual grid for the hdMSEM to eliminate the singularity problem while keeping the discrete system symmetrical and mathematical definition rigorous and study the implementation of several different kinds of boundary conditions in this framework. Finally, we propose a pressure-linked pseudo-time-stepping method and a MEEVC scheme in the framework of the hdMSEM with the novel dual grid and extend it to solve steady and unsteady Navier-Stokes equations.

3.1. Topology of the Novel Dual Grid for the hdMSEM
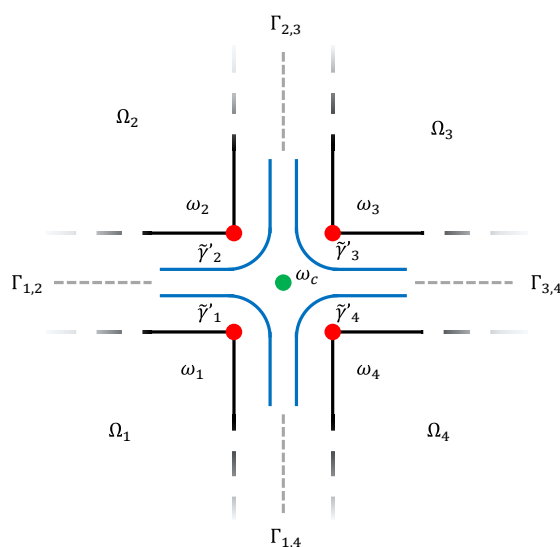
Figure 3.1: Topology of the novel dual grid: Red dots stand for degrees of freedom of $\underline{\omega} \in \underline{EP}_N(\Omega_i)$; blue lines stand for degrees of freedom of $\underline{\tilde{\gamma}}' \in \underline{\widetilde{TE}}_N(\Gamma_{c,i})$ for the novel dual grid ($\Gamma_{c,i}$ stands for the boundary between dummy element Ω_c and subdomain Ω_i); green dots is the dummy degree of freedom introduced to eliminate the singularity problem.

Based on the idea given by Zhang [10], this project proposes a novel dual grid as illustrated in Fig.3.1. This dual grid eliminates the singularity problem and keeps the discrete system symmetrical. The linear
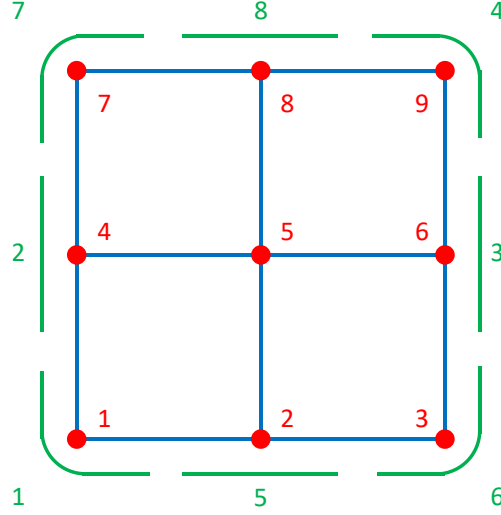
Figure 3.2: Numbering of the geometric elements in a 2nd-order element with dual trace degrees of freedom, where red numbers for edges and green numbers for dual trace edges.

system for Stokes equations with primal-dual grid can be derived as:

$$
\begin{bmatrix}
M_E & -E_{curl}^T M_F & 0 & \mathbb{T}_E'^T & 0 & 0 \\
-M_F^T E_{curl} & 0 & E_{div}^T & 0 & \mathbb{T}_F^T & 0 \\
0 & E_{div} & 0 & 0 & 0 & 0 \\
\mathbb{T}_E' & 0 & 0 & 0 & 0 & \mathbb{D}^T \\
0 & \mathbb{T}_F & 0 & 0 & 0 & 0 \\
0 & 0 & 0 & \mathbb{D} & 0 & 0
\end{bmatrix}
\begin{bmatrix}
\underline{\omega} \\
\underline{u} \\
\underline{\tilde{p}} \\
\underline{\tilde{\gamma}} \\
\underline{\tilde{\lambda}} \\
\underline{\omega_c}
\end{bmatrix}
=
\begin{bmatrix}
0 \\
-\tilde{f} \\
0 \\
0 \\
0 \\
0
\end{bmatrix},
\tag{3.1}
$$

where $\mathbb{T}_E'$ is the matrix of trace operator projecting functions from $EP_N(\Omega_i)$ to $TE_N(\partial\Omega_i)$, but now there is only one trace degree of freedom at each corner so the $\mathbb{T}_E'$ is surjective. Take a 2nd-order element with dual trace dofs over curve lines, shown in Fig3.2, as an example, the new trace matrix $\mathbb{T}_E'$ is

$$
\mathbb{T}_E' =
\begin{bmatrix}
1 & 0 & 0 & 0 & 0 & 0 & 0 & 0 & 0 \\
0 & 0 & 0 & 1 & 0 & 0 & 0 & 0 & 0 \\
0 & 0 & 0 & 0 & 0 & -1 & 0 & 0 & 0 \\
0 & 0 & 0 & 0 & 0 & 0 & 0 & 0 & -1 \\
0 & -1 & 0 & 0 & 0 & 0 & 0 & 0 & 0 \\
0 & 0 & -1 & 0 & 0 & 0 & 0 & 0 & 0 \\
0 & 0 & 0 & 0 & 0 & 0 & 1 & 0 & 0 \\
0 & 0 & 0 & 0 & 0 & 0 & 0 & 1 & 0
\end{bmatrix}.
\tag{3.2}
$$

With the novel dual grid, the singularity problem is avoided, and the discrete system remains symmetric.

In addition, the matrix $\mathbb{D}$ and $\mathbb{D}^T$ has an exact mathematical definition in the hdMSEM:

$$
\langle \omega_h \times \boldsymbol{n}, \varepsilon_h \rangle_{\partial\Omega_c} = 0 \quad \forall \varepsilon_h \in \widetilde{TE}_N(\partial\Omega_c),
\tag{3.3a}
$$

$$
\langle \tilde{\gamma}_h, \xi_h \times \boldsymbol{n} \rangle_{\partial\Omega_c} = 0 \quad \forall \xi_h \in EP_N(\Omega_c),
\tag{3.3b}
$$

where Ω_c is an infinitely small element at the edge where four elements meet. So Eq. (3.3a) is the integral over the blue curve line in Fig. 3.1, and Eq. (3.3b) is the discrete Green's formula around the infinite small element Ω_c.

Further, this thesis extends the hdMSEM with the novel dual grid to steady and unsteady Navier-Stokes equations and studies the implementation of several kinds of boundary conditions.

3.2. Implementation of Boundary Conditions in the hdMSEM

3.2.1. No-slip Wall

One of the most common boundary conditions in CFD is the no-slip condition. The normal and tangential velocities are zero or values given explicitly when the wall boundary moves.

For a wall boundary where the normal velocity and tangential velocity are given explicitly, there is

$$\begin{cases} \boldsymbol{u}^h \cdot \boldsymbol{n} = \hat{u}_\perp & \text{on } \Gamma_\perp \\ \boldsymbol{u}^h \times \boldsymbol{n} = \hat{u}_\| & \text{on } \Gamma_\| \end{cases}, \tag{3.4}$$

where $\boldsymbol{n}$ is the outward unit normal vector at the boundary.

In the framework of the hdMSEM, trace variable $\tilde{\gamma} = \boldsymbol{u} \times \boldsymbol{n}$ is associated with the tangential velocity. So, the matrix form of the boundary conditions is

$$\begin{aligned} \mathbb{T}_\mathsf{F}\underline{\boldsymbol{u}} = \hat{\underline{u}}_\perp & \qquad \forall \underline{\tilde{\lambda}} \in \widetilde{\underline{\mathsf{TF}}}_{N-1}(\Gamma_\perp), \\ \underline{\tilde{\gamma}} = \mathsf{M}_\mathsf{TE}\hat{\underline{u}}_\| & \qquad \forall \underline{\tilde{\gamma}} \in \widetilde{\underline{\mathsf{TE}}}_N(\Gamma_\|). \end{aligned} \tag{3.5}$$

The topology of the dual grid at the no-slip wall is presented in Fig. 3.3. Though the value of the trace degree of freedom $\tilde{\gamma}_i$, which is perpendicular to the boundary (presented as a green line in Fig. 3.3) is related to the boundary conditions, no values should be posed explicitly on those degrees of freedom as the discrete vorticity equation constrains them, i.e. Eq. (2.70a). In addition, whether the boundary is topologically straight or cornered, there is no need to introduce a dummy degree of freedom at the edge where subdomains meet, because there is no redundant equations in coupling the vorticity variables at the edge: for straight boundary shown in Fig. 3.3a, there is

$$\omega_1 - \omega_2 = 0, \tag{3.6a}$$

and for boundary with corner shown in Fig. 3.3b, there is

$$\omega_1 - \omega_2 = 0, \tag{3.7a}$$
$$\omega_2 - \omega_3 = 0, \tag{3.7b}$$

where there is no explicit specification for the value of ω_1, ω_2 and ω_3.

Similar to the no-slip wall condition is the velocity inlet, which is generally considered the driving force so that the tangential and normal velocity are explicitly known.

3.2.2. Free-slip Wall

Free-slip wall condition is generally used in simulating external flow fields. At the free-slip wall, normal velocity is considered zero, and the stress is also zero at the wall. In the framework of the hdMSEM, the zero stress condition can be interpreted as a zero vorticity condition. Hence there is

$$\begin{cases} \boldsymbol{u}^h \cdot \boldsymbol{n} = 0 & \text{on } \Gamma_\perp \\ \omega^h = 0 & \text{on } \Gamma_{\hat{\omega}} \end{cases}. \tag{3.8}$$

However, the topology of the dual grid used for no-slip wall presented in Fig. 3.3 is not suitable anymore for zero vorticity boundary: Take the dual grid in Fig. 3.3a for example, when zero conditions are posed for ω_1 and ω_2,

$$\omega_1 = 0 \quad \text{and} \quad \omega_2 = 0, \tag{3.9}$$

the strong continuity constraint equation posed by Lagrange multiplier $\tilde{\gamma}_3$,

$$\omega_1 - \omega_2 = 0, \tag{3.10}$$

(a) straight boundary

(b) boundary with corner
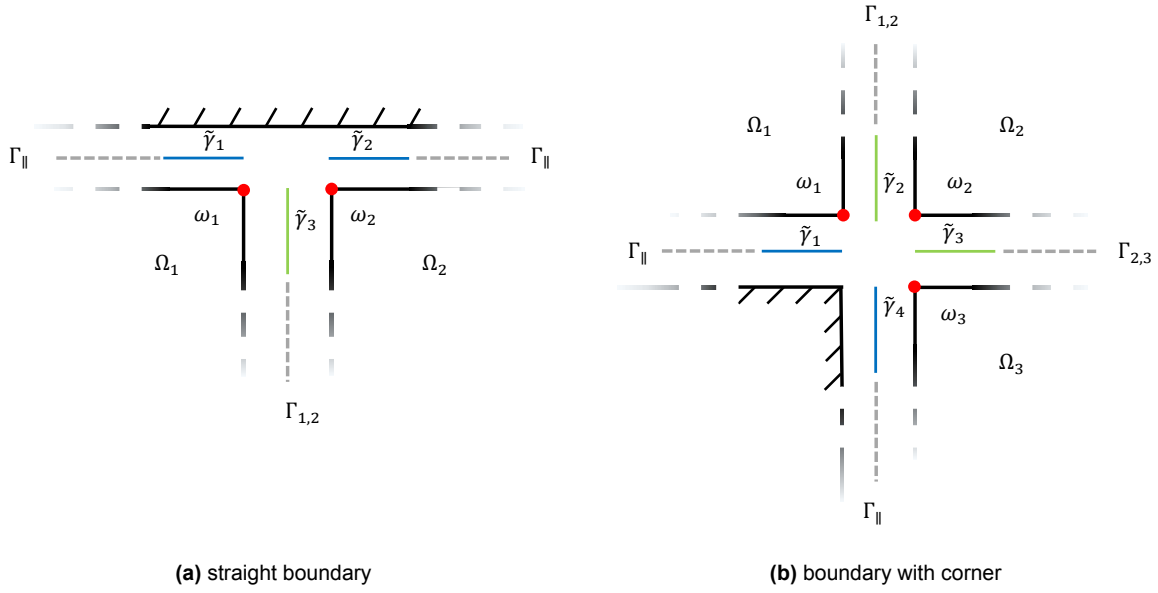
Figure 3.3: Topology of the novel dual grid near no-slip wall: Blue lines stands for trace degrees of freedom $\tilde{\underline{\gamma}} \in \widetilde{\underline{\mathsf{TE}}}_N(\Gamma_{\parallel})$, where the tangential velocity conditions are imposed; green lines stands for trace degrees of freedom $\tilde{\underline{\gamma}} \notin \widetilde{\underline{\mathsf{TE}}}_N(\Gamma_{\parallel})$, and no constraint should be posed.

is redundant and a singularity problem arises.

Hence, similar to the dual grid discussed in Section 3.1, a curve dual grid is applied around the edge where two nearby elements are bordered with the wall, see in Fig. 3.4. Here, there is no dummy degree of freedom required at the corner wherer two subdomains meet, since the curvilinear dual grid eliminates the coupling equation,

$$\omega_1 - \omega_2 = 0, \tag{3.11}$$

and the trace operator associated with the curvlinear dual grid $\mathbb{T}'_\mathsf{E}$ impose the specified values for the vorticity degrees of freedom at the boundary,

$$\omega_1 = 0, \tag{3.12a}$$
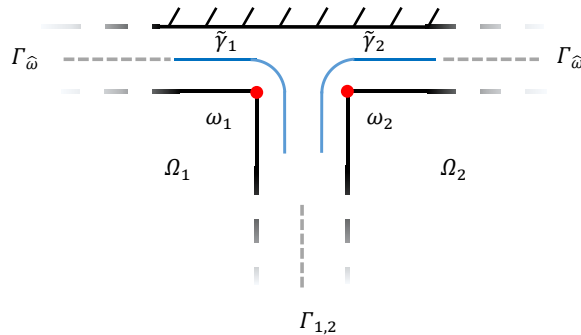$$-\omega_2 = 0. \tag{3.12b}$$

Figure 3.4: Topology of the dual grid near the free-slip wall: Blue curve lines stand for trace degrees of freedom $\tilde{\underline{\gamma}} \in \widetilde{\underline{\mathsf{TE}}}_N(\Gamma_{\hat{\omega}})$.
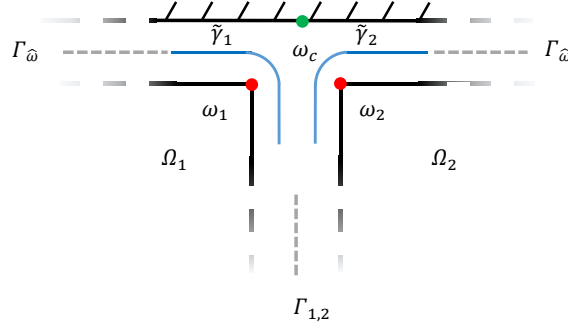
Figure 3.5: Topology of the dual grid near the non-zero vorticity boundary: Green node stands for dummy degree of freedom at the boundary $\underline{\omega_c} \in \mathsf{EP}_N(\Gamma_{\hat{\omega}})$.

And the matrix form of the free-slip boundary conditions can be expressed as

$$
\begin{aligned}
\mathbb{T}_\mathsf{F}\underline{u} &= 0 & \forall \tilde{\underline{\lambda}} &\in \widetilde{\mathbb{TF}}_{N-1}(\Gamma_\perp), \\
\mathbb{T}'_\mathsf{E}\underline{\omega} &= 0 & \forall \tilde{\underline{\gamma}} &\in \widetilde{\mathbb{TE}}_N(\Gamma_{\hat{\omega}}).
\end{aligned}
\tag{3.13}
$$

For non-zero vorticity boundary condition, i.e.,

$$
\omega^h = \hat{\omega} \qquad \text{on } \Gamma_{\hat{\omega}},
\tag{3.14}
$$

where $\hat{\omega} \not\equiv 0$, it is not convenient to define the sign of values associated to $\mathbb{T}'_\mathsf{E}\omega$, as it depends on the numbering of geometric elements during meshing. Therefore, a dummy degree of freedom is introduced, presented in Fig. 3.5. And the matrix formulation to impose the vorticity condition is

$$
\underline{\omega_c} = \hat{\underline{\omega}} \qquad \forall \underline{\omega_c} \in \mathsf{EP}_N(\Gamma_{\hat{\omega}}).
\tag{3.15}
$$

3.2.3. Total Pressure Inlet

In the Stoke equations, there is no difference between total pressure and static pressure however for the Navier-Stokes equations in the Velocity-Vorticity-Pressure formulation (3.22), which will be discussed in detail in Section 3.3, the P stands for total pressure and there is

$$
\lambda = -P \qquad \text{on } \partial\Omega_i.
\tag{3.16}
$$

Besides, the tangential velocity at the pressure inlet is generally set as zero. So, boundary conditions can be written as

$$
\begin{cases}
P^h = \hat{P} & \text{on } \Gamma_{\hat{P}}, \\
\boldsymbol{u}^h \times \boldsymbol{n} = 0 & \text{on } \Gamma_\|,
\end{cases}
\tag{3.17}
$$

with the matrix form

$$
\begin{aligned}
\tilde{\underline{\lambda}} &= -\mathsf{M}_{\mathsf{TF}}\hat{\underline{P}} & \forall \tilde{\underline{\lambda}} &\in \widetilde{\mathbb{TF}}_{N-1}(\Gamma_{\hat{P}}), \\
\tilde{\underline{\gamma}} &= \mathsf{M}_{\mathsf{TE}}\hat{\underline{u}}_\| & \forall \tilde{\underline{\gamma}} &\in \widetilde{\mathbb{TE}}_N(\Gamma_\|).
\end{aligned}
\tag{3.18}
$$

3.2.4. Static Pressure Outlet

In studying incompressible flow, a value of static pressure is generally given explicitly at the outlet. The traditional CFD method has no specification for tangential and normal velocity at the outlet.

$$
P^h = \hat{p} + \frac{1}{2}(\boldsymbol{u}^h)^2 \qquad \text{on } \Gamma_{\hat{p}}
\tag{3.19}
$$

However in the framework of the hdMSEM, trace variable γ at the pressure outlet stands for the tangential velocity at the outlet boundary, and it plays a role in the variational formulation of the vorticity equation Eq.

(2.70a). Therefore, the matrix form of the boundary conditions is

$$\underline{\tilde{\lambda}} = -\mathsf{M}_{\mathsf{TF}}(\underline{\hat{p}} + \frac{1}{2}\mathcal{M}(\underline{\boldsymbol{u}})\underline{\boldsymbol{u}}) \qquad \forall \underline{\tilde{\lambda}} \in \widetilde{\mathsf{TF}}_{N-1}(\Gamma_{\hat{p}}),$$

$$\underline{\tilde{\gamma}} = \mathsf{M}_{\mathsf{TE}}\mathcal{M}_{\|}\underline{\boldsymbol{u}} \qquad \forall \underline{\tilde{\gamma}} \in \widetilde{\mathsf{TE}}_{N}(\Gamma_{\|}),$$

$$(3.20)$$

where $\mathcal{M}$ is a matrix operator which is dependent on $\underline{\boldsymbol{u}}$ and $\mathcal{M}_{\|}$ is a constant matrix transferring the velocity field inside domain to the tangential velocity at the outlet boundary.

3.3. Temporal Discretization and Timestepping Method for the hdM-SEM

3.3.1. Navier-Stokes Equations in the Velocity-Vorticity-Pressure formulation

Write the 2D unsteady incompressible Navier-Stokes equations in the Velocity-Vorticity-Pressure formulation,

$$\omega - \nabla \times \boldsymbol{u} = 0 \qquad \text{in } \Omega_i, \tag{3.21a}$$

$$\partial_t \boldsymbol{u} + \omega \times \boldsymbol{u} + \nu\nabla \times \omega + \nabla P = \boldsymbol{f} \qquad \text{in } \Omega_i, \tag{3.21b}$$

$$\nabla \cdot \boldsymbol{u} = 0 \qquad \text{in } \Omega_i, \tag{3.21c}$$

where Ω_i is the subdomain in $\mathbb{R}^2$, $P = p + \frac{1}{2}u^2$ is the total pressure (with p being the static pressure) and ν is the kinematic viscosity.

The equations at physical boundaries and interfaces between subdomains are

$$\omega = \hat{\omega} \qquad \text{on } \Gamma_{\hat{\omega}} \cap \partial\Omega_i, \tag{3.22a}$$

$$P - \frac{1}{2}u^2 = \hat{p} \qquad \text{on } \Gamma_{\hat{p}} \cap \partial\Omega_i, \tag{3.22b}$$

$$P = \hat{P} \qquad \text{on } \Gamma_{\hat{P}} \cap \partial\Omega_i, \tag{3.22c}$$

$$\boldsymbol{u} \times \boldsymbol{n} = \hat{\boldsymbol{u}}_{\|} \qquad \text{on } \Gamma_{\hat{\boldsymbol{u}}_{\|}} \cap \partial\Omega_i, \tag{3.22d}$$

$$\boldsymbol{u} \cdot \boldsymbol{n} = \hat{\boldsymbol{u}}_{\perp} \qquad \text{on } \Gamma_{\hat{\boldsymbol{u}}_{\perp}} \cap \partial\Omega_i, \tag{3.22e}$$

$$P = -\lambda \qquad \text{on } \Gamma_{i,j}, \tag{3.22f}$$

$$\boldsymbol{u} \cdot \boldsymbol{n}_i + \boldsymbol{u} \cdot \boldsymbol{n}_j = 0 \qquad \text{on } \Gamma_{i,j}, \tag{3.22g}$$

$$\omega \times \boldsymbol{n}_i + \omega \times \boldsymbol{n}_j = 0 \qquad \text{on } \Gamma_{i,j}. \tag{3.22h}$$

And the variational formulation is presented as follows: Given $f \in [L^2(\Omega)]^3$, $g \in L^2(\Omega)$, $\hat{\boldsymbol{u}} \times \boldsymbol{n} \in TH_{00}^{1/2}(\Gamma_{\boldsymbol{u}\times\boldsymbol{n}})$, $\hat{p} \in H_{00}^{1/2}(\Gamma_P)$ and $\hat{P} \in H_{00}^{1/2}(\Gamma_P)$ the solution $(\omega, \boldsymbol{u}, P, \gamma, \lambda) \in H_0(\text{curl}, \Omega_i; \Gamma_\omega) \times H_0(\text{div}, \Omega_i; \Gamma_{\boldsymbol{u}\cdot\boldsymbol{n}}) \times L^2(\Omega_i) \times TH_{00}^{1/2}(\partial\Omega_i) \times H_{00}^{1/2}(\partial\Omega_i)$ has

$$\langle\omega, \xi\rangle_{\Omega_i} - \langle\boldsymbol{u}, \nabla \times \xi\rangle_{\Omega_i} - \langle\gamma, \xi \times \boldsymbol{n}\rangle_{\partial\Omega_i} = \langle\xi \times \boldsymbol{n}, \hat{\boldsymbol{u}} \times \boldsymbol{n}\rangle_{\partial\Omega_i \cap \Gamma_{\boldsymbol{u}\times\boldsymbol{n}}} \quad \forall\xi \in H_0(\text{curl}, \Omega; \Gamma_{\hat{\omega}} \cap \partial\Omega_i), \tag{3.23a}$$

$$\langle\partial_t\boldsymbol{u}, \boldsymbol{v}\rangle_{\Omega_i} + \langle\omega \times \boldsymbol{u}, \boldsymbol{v}\rangle_{\Omega_i} + \nu\langle\nabla \times \omega, \boldsymbol{v}\rangle_{\Omega_i} - \langle P, \nabla \cdot \boldsymbol{v}\rangle_{\Omega_i} + \langle\lambda, \boldsymbol{v} \cdot \boldsymbol{n}\rangle_{\partial\Omega_i}$$
$$= \langle\boldsymbol{f}, \boldsymbol{v}\rangle_{\Omega_i} - \langle\hat{P}, \boldsymbol{v} \cdot \boldsymbol{n}\rangle_{\partial\Omega \cap \Gamma_P} \quad \forall\boldsymbol{v} \in H_0(\text{div}, \Omega_i; \Gamma_{\boldsymbol{u}\cdot\boldsymbol{n}} \cap \partial\Omega_i), \tag{3.23b}$$

$$\langle\nabla \cdot \boldsymbol{u}, q\rangle_{\Omega_i} = 0 \quad \forall q \in L^2(\Omega_i), \tag{3.23c}$$

$$\langle\omega \times \boldsymbol{n}, \varepsilon\rangle_{\partial\Omega_i} = 0 \quad \forall\varepsilon \in TH_{00}^{1/2}(\partial\Omega_i), \tag{3.23d}$$

$$\langle\boldsymbol{u} \cdot \boldsymbol{n}, \psi\rangle_{\partial\Omega_i} = 0 \quad \forall\psi \in H_{00}^{1/2}(\partial\Omega). \tag{3.23e}$$

3.3.2. Pressure-linked Pseudo Time-stepping Method for Steady N-S Equations

For steady cases, this thesis proposes a pressure-linked pseudo time stepping method for the hdMSEM.

Considering the pseudo time-stepping, the fully discretized problem for subdomain Ω_i, there is

$$\left\langle \frac{\boldsymbol{u}_h^{k+1} - \boldsymbol{u}_h^k}{\Delta t}, \boldsymbol{v}_h \right\rangle_\Omega + \left\langle \omega_h^k \times \boldsymbol{u}_h^k, \boldsymbol{v}_h \right\rangle_{\Omega_i} + \nu \left\langle \nabla \times \omega_h^k, \boldsymbol{v}_h \right\rangle_{\Omega_i} - \left\langle P_h^{k+1}, \nabla \cdot \boldsymbol{v}_h \right\rangle_{\Omega_i}$$

$$- \left\langle \tilde{\lambda}_h^{k+1}, \boldsymbol{v}_h \cdot \boldsymbol{n} \right\rangle_{\partial \Omega_i} = \left\langle \boldsymbol{f}_h, \boldsymbol{v}_h \right\rangle_{\Omega_i} \quad \forall \boldsymbol{v}_h \in \mathsf{FP}_{N-1}(\Omega_i),$$

$$\left\langle \boldsymbol{u}_h^{k+1}, \nabla \times \xi_h \right\rangle_{\Omega_i} - \left\langle \omega_h^{k+1}, \xi_h \right\rangle_{\Omega_i} - \left\langle \tilde{\gamma}_h^{k+1}, \xi_h \times \boldsymbol{n} \right\rangle_{\partial \Omega_i} = 0 \quad \forall \xi_h \in \mathsf{EP}_N(\Omega_i), \tag{3.24}$$

$$\left\langle \nabla \cdot \boldsymbol{u}_h^{k+1}, q_h \right\rangle_{\Omega_i} = 0 \quad \forall q_h \in \widetilde{\mathsf{VP}}_{N-1}(\Omega_i),$$

$$\left\langle \omega_h^{k+1} \times \boldsymbol{n}, \varepsilon_h \right\rangle_{\partial \Omega_i} = 0 \quad \forall \varepsilon_h \in \widetilde{\mathsf{TE}}_N(\partial \Omega_i),$$

$$\left\langle \boldsymbol{u}_h^{k+1} \cdot \boldsymbol{n}, \psi_h \right\rangle_{\partial \Omega_i} = 0 \quad \forall \psi_h \in \widetilde{\mathsf{TF}}_{N-1}(\partial \Omega_i),$$

and for the dummy subdomain Ω_c:

$$\left\langle \omega_h^{k+1} \times \boldsymbol{n}, \varepsilon_h \right\rangle_{\partial \Omega_c} = 0 \quad \forall \varepsilon_h \in \widetilde{\mathsf{TE}}_N(\partial \Omega_c),$$

$$\left\langle \tilde{\gamma}_h^{k+1}, \xi_h \times \boldsymbol{n} \right\rangle_{\partial \Omega_c} = 0 \quad \forall \xi_h \in \mathsf{EP}_N(\Omega_c). \tag{3.25}$$

At first, we define a discretized operator $C(\omega, \boldsymbol{u})$ to compute the convection term with velocity and vorticity: set

$$\underline{\boldsymbol{c}} = C(\omega, \boldsymbol{u}) \quad \text{where} \quad \underline{\boldsymbol{c}} = \begin{bmatrix} \boldsymbol{c}_1 \; \boldsymbol{c}_2 \; \boldsymbol{c}_3 \; ... \; \boldsymbol{c}_{N_u} \end{bmatrix}^\mathsf{T}, \tag{3.26}$$

such that

$$\omega_h \times \boldsymbol{u}_h = \sum_i^{N_u} \boldsymbol{v}_i \boldsymbol{c}_i \quad \text{and} \quad \omega_h \times \boldsymbol{u}_h \in \mathsf{FP}_{N-1}(\Omega_i). \tag{3.27}$$

In pressure-driven time-stepping, the pressure is firstly calculated to meet the divergence-free condition of velocity:

$$\begin{bmatrix} \mathsf{E}_{\mathsf{div}} \mathsf{M}_{\mathsf{F}}^{-1} \mathsf{E}_{\mathsf{div}}^\mathsf{T} & \mathsf{E}_{\mathsf{div}} \mathsf{M}_{\mathsf{F}}^{-1} \mathbb{T}_{\mathsf{F}}^\mathsf{T} \\ \\ \mathbb{T}_{\mathbb{F}} \mathsf{M}_{\mathsf{F}}^{-1} \mathsf{E}_{\mathsf{div}}^\mathsf{T} & \mathbb{T}_{\mathsf{F}} \mathsf{M}_{\mathsf{F}}^{-1} \mathbb{T}_{\mathsf{F}}^\mathsf{T} \end{bmatrix} \begin{bmatrix} \underline{\tilde{P}}^{k+1} \\ \\ \underline{\tilde{\lambda}}^{k+1} \end{bmatrix} = \begin{bmatrix} \mathsf{E}_{\mathsf{div}} C(\underline{\omega}^k, \underline{\boldsymbol{u}}^k) + \nu \mathsf{E}_{\mathsf{div}} \mathsf{E}_{\mathsf{curl}} \underline{\omega}^k - \mathsf{E}_{\mathsf{div}} \frac{\underline{\boldsymbol{u}}^k}{\Delta t} \\ \\ \mathbb{T}_{\mathsf{F}} C(\underline{\omega}^k, \underline{\boldsymbol{u}}^k) + \nu \mathbb{T}_{\mathsf{F}} \mathsf{E}_{\mathsf{curl}} \underline{\omega}^k - \mathbb{T}_{\mathsf{F}} \frac{\underline{\boldsymbol{u}}^k}{\Delta t} \end{bmatrix}. \tag{3.28}$$

In hybrid MSEM, $\mathsf{M}_{\mathsf{F}}^{-1}$ is the inverted local mass matrix for each subdomain, so it can be calculated directly rather than solving a large-scale linear system.

In the next, update the velocity field by

$$\underline{\boldsymbol{u}}^{k+1} = \underline{\boldsymbol{u}}^k + \Delta t (\mathsf{M}_{\mathsf{F}}^{-1} \mathsf{E}_{\mathsf{div}}^\mathsf{T} \underline{\tilde{P}}^{k+1} + \mathsf{M}_{\mathsf{F}}^{-1} \mathbb{T}_{\mathsf{F}}^\mathsf{T} \underline{\tilde{\lambda}}^{k+1} - C(\underline{\omega}^k, \underline{\boldsymbol{u}}^k) - \nu \mathsf{E}_{\mathsf{curl}} \underline{\omega}^k), \tag{3.29}$$

and finally, update the field associated with vorticity:

$$\begin{bmatrix} \mathsf{M}_{\mathsf{E}} & \mathbb{T}_{\mathsf{E}}^{'\mathsf{T}} & 0 \\ \mathbb{T}_{\mathsf{E}}^{'} & 0 & \mathbb{D}^\mathsf{T} \\ 0 & \mathbb{D} & 0 \end{bmatrix} \begin{bmatrix} \underline{\omega}^{k+1} \\ \underline{\tilde{\gamma}}^{k+1} \\ \underline{\omega_c}^{k+1} \end{bmatrix} = 0. \tag{3.30}$$

For linear system (3.28) and (3.30) can be arranged in the form of system (2.72), so the domain decomposition can be implemented in the pressure-linked pseudo time stepping method for the hdMSEM.

It is worth mentioning that the implementation of the normal velocity boundary condition at the boundary is different from that mentioned in the Section 3.2.1, since the velocity field variable u does not appear in the unknowns vector in this time stepping method. Instead, it should be implemented as a constraint when updating the field of P in (3.28):

$$\mathbb{T}_{\mathsf{F}} \mathsf{M}_{\mathsf{F}}^{-1} (\mathsf{E}_{\mathsf{div}}^\mathsf{T} \underline{\tilde{P}}^{k+1} + \mathbb{T}_{\mathsf{F}}^\mathsf{T} \underline{\tilde{\lambda}}^{k+1}) = \mathbb{T}_{\mathsf{F}} (C(\underline{\omega}^k, \underline{\boldsymbol{u}}^k) + \nu \mathsf{E}_{\mathsf{curl}} \underline{\omega}^k - \frac{\underline{\boldsymbol{u}}^k}{\Delta t}) + \frac{\hat{u}_\perp}{\Delta t} \quad \underline{\tilde{\lambda}} \in \widetilde{\mathsf{TF}}_{N-1}(\Gamma_\perp), \tag{3.31}$$

3.3.3. The MEEVC Scheme for Unsteady N-S Equations

Finally, following the idea of the mass, energy, enstrophy, and vorticity conserving (MEEVC) scheme [47], this project extends hMSEM with the novel dual grid to unsteady cases for 2D incompressible Navier-Stokes equations.

The MEEVC scheme uses a kinetic energy conservative time integrator, the fully discretized formulation for subdomain Ω_i is

$$
\left\langle \frac{\boldsymbol{u}_h^{k+1} - \boldsymbol{u}_h^k}{\Delta t}, \boldsymbol{v}_h \right\rangle_{\Omega_i} + \left\langle \frac{\omega_h^{k+1} + \omega_h^k}{2} \times \frac{\boldsymbol{u}_h^{k+1} + \boldsymbol{u}_h^k}{2}, \boldsymbol{v}_h \right\rangle_{\Omega_i} + \nu \left\langle \nabla \times \frac{\omega_h^{k+1} + \omega_h^k}{2}, \boldsymbol{v}_h \right\rangle_{\Omega_i}
$$

$$
- \left\langle P_h^{k+1/2}, \nabla \cdot \boldsymbol{v}_h \right\rangle_{\Omega_i} - \left\langle \tilde{\lambda}_h^{k+1/2}, \boldsymbol{v}_h \cdot \boldsymbol{n} \right\rangle_{\partial \Omega_i} = \left\langle \boldsymbol{f}_h, \boldsymbol{v}_h \right\rangle_{\Omega_i} \quad \forall \boldsymbol{v}_h \in \mathsf{FP}_{N-1}(\Omega_i),
$$

$$
\left\langle \boldsymbol{u}_h^{k+1}, \nabla \times \xi_h \right\rangle_{\Omega} - \left\langle \omega_h^{k+1}, \xi_h \right\rangle_{\Omega_i} - \left\langle \tilde{\gamma}_h^{k+1}, \xi_h \times \boldsymbol{n} \right\rangle_{\partial \Omega_i} = 0 \quad \forall \xi_h \in \mathsf{EP}_N(\Omega_i),
$$

$$
\left\langle \nabla \cdot \boldsymbol{u}_h^{k+1}, q_h \right\rangle_{\Omega_i} = 0 \quad \forall q_h \in \widetilde{\mathsf{VP}}_{N-1}(\Omega_i),
$$

$$
\left\langle \omega_h^{k+1} \times \boldsymbol{n}, \varepsilon_h \right\rangle_{\partial \Omega_i} = 0 \quad \forall \varepsilon_h \in \widetilde{\mathsf{TE}}_N(\partial \Omega_i),
$$

$$
\left\langle \boldsymbol{u}_h^{k+1} \cdot \boldsymbol{n}, \psi_h \right\rangle_{\partial \Omega_i} = 0 \quad \forall \psi_h \in \widetilde{\mathsf{TF}}_{N-1}(\partial \Omega_i),
$$

(3.32)

and for the dummy subdomain, the scheme is the same with system (3.25).

In one time step, the discrete pressure field $\tilde{P}_h$ and discrete trace variables $\tilde{\lambda}_h$ stands for the value at middle time point, and the average value of velocity field $\boldsymbol{u}_h$ and vorticity field ω_h at time point k and $k+1$ are used to calculate the convection and dissipation terms at the middle time point. Therefore, when applying the static boundary condition, there is

$$
P^{k+1/2} = \hat{p} + \frac{1}{2} \left(\frac{\boldsymbol{u}^{k+1} + \boldsymbol{u}^k}{2} \right)^2 \qquad \text{on } \partial \Gamma_{\hat{p}},
$$

(3.33)

and the discrete form is

$$
\underline{\tilde{\lambda}} = -\mathsf{M}_{\mathsf{TF}} (\underline{\hat{p}} + \frac{1}{2} \mathcal{M}(\underline{\boldsymbol{u}}) \underline{\boldsymbol{u}}) \qquad \forall \underline{\tilde{\lambda}} \in \widetilde{\mathsf{TF}}_{N-1}(\Gamma_{\hat{p}}).
$$

(3.34)

In order to use a relatively large time step while preserving the conservation structure, the nonlinear system (3.32) is solved fully coupled with Newton iteration method. The general form of the Newton iteration to solve nonelinear equation $f(x) = 0$ can be written as

$$
f'(x^i) x^{i+1} = f'(x^i) x^i - f(x^i),
$$

(3.35)

where x^i and x^{i+1} are numerical solutions approaching the exact solution. In the MEEVC scheme updating from step k to $k+1$ there is

$$
f(x^i) =
\begin{bmatrix}
\mathsf{M}_\mathsf{E} & -\mathsf{E}_{\mathsf{curl}}^\mathsf{T} \mathsf{M}_\mathsf{F} & 0 & \mathbb{T}_\mathsf{E}'^\mathsf{T} & 0 & 0 \\
-0.5\nu \mathsf{M}_\mathsf{F}^\mathsf{T} \mathsf{E}_{\mathsf{curl}} & -\mathsf{M}_\mathsf{F}/dt & \mathsf{E}_{\mathsf{div}}^\mathsf{T} & 0 & \mathbb{T}_\mathsf{F}^\mathsf{T} & 0 \\
0 & \mathsf{E}_{\mathsf{div}} & 0 & 0 & 0 & 0 \\
\mathbb{T}_\mathsf{E}' & 0 & 0 & 0 & 0 & \mathbb{D}^\mathsf{T} \\
0 & \mathbb{T}_\mathsf{F} & 0 & 0 & 0 & 0 \\
0 & 0 & 0 & \mathbb{D} & 0 & 0
\end{bmatrix}
\begin{bmatrix}
\underline{\omega}^i \\
\underline{\boldsymbol{u}}^i \\
\underline{\tilde{P}}^i \\
\underline{\tilde{\lambda}}^i \\
\underline{\tilde{\gamma}}^i \\
\underline{\omega_c}^i
\end{bmatrix}
$$

$$
+
\begin{bmatrix}
0 \\
\mathsf{M}_\mathsf{F}(-0.5\nu \mathsf{E}_{\mathsf{curl}}{}^k + \boldsymbol{u}^k/dt - C(\frac{\underline{\omega}^i + \omega^k}{2}, \frac{\underline{\boldsymbol{u}}^i + \boldsymbol{u}^k}{2})) \\
0 \\
0 \\
0 \\
0
\end{bmatrix},
$$

(3.36)

$$
f'(x^i) = \begin{bmatrix}
\mathsf{M_E} & -\mathsf{E}_\mathsf{curl}^\mathsf{T}\mathsf{M_F} & 0 & \mathbb{T}_\mathsf{E}'^\mathsf{T} & 0 & 0 \\
-0.5\nu\mathsf{M_F}^\mathsf{T}\mathsf{E_{curl}} & -\mathsf{M_F}/dt & \mathsf{E}_\mathsf{div}^\mathsf{T} & 0 & \mathbb{T}_\mathsf{F}^\mathsf{T} & 0 \\
0 & \mathsf{E_{div}} & 0 & 0 & 0 & 0 \\
\mathbb{T}_\mathsf{E}' & 0 & 0 & 0 & 0 & \mathbb{D}^\mathsf{T} \\
0 & \mathbb{T}_\mathsf{F} & 0 & 0 & 0 & 0 \\
0 & 0 & 0 & \mathbb{D} & 0 & 0
\end{bmatrix}
- 0.25 \begin{bmatrix}
0 & 0 & 0 & 0 & 0 & 0 \\
\mathsf{M_F}C_u(\underline{\boldsymbol{u}}^i) & \mathsf{M_F}C_\omega(\underline{\omega}^i) & 0 & 0 & 0 & 0 \\
0 & 0 & 0 & 0 & 0 & 0 \\
0 & 0 & 0 & 0 & 0 & 0 \\
0 & 0 & 0 & 0 & 0 & 0 \\
0 & 0 & 0 & 0 & 0 & 0
\end{bmatrix}
$$

$$
- 0.25 \begin{bmatrix}
0 & 0 & 0 & 0 & 0 & 0 \\
\mathsf{M_F}C_u(\underline{\boldsymbol{u}}^k) & \mathsf{M_F}C_\omega(\underline{\omega}^k) & 0 & 0 & 0 & 0 \\
0 & 0 & 0 & 0 & 0 & 0 \\
0 & 0 & 0 & 0 & 0 & 0 \\
0 & 0 & 0 & 0 & 0 & 0 \\
0 & 0 & 0 & 0 & 0 & 0
\end{bmatrix},
\tag{3.37}
$$

where $C(\underline{\omega}, \underline{\boldsymbol{u}})$ is an operator to calculate the discrete convection term, and C_ω and C_u are the coefficient matrices associated with $\frac{\partial \omega \times \boldsymbol{u}}{\partial \boldsymbol{u}}$ and $\frac{\partial \omega \times \boldsymbol{u}}{\partial \omega}$.

In addition, the static pressure boundary condition is implemented in a nonlinear equation as well,

$$
\underline{\tilde{\lambda}}^{k+1/2} = -\mathsf{M_{TF}}\left[\hat{\underline{p}} + \frac{1}{2}\mathcal{M}(\frac{\boldsymbol{u}^k + \boldsymbol{u}^{k+1}}{2})(\frac{\boldsymbol{u}^k + \boldsymbol{u}^{k+1}}{2})\right] \qquad \forall \underline{\tilde{\lambda}} \in \widetilde{\mathsf{TF}}_{N-1}(\Gamma_{\hat{p}}),
\tag{3.38}
$$

and solved with Newton iteration method as following:

$$
\begin{bmatrix} 0 & 0.25\mathsf{M_{TF}}(\mathcal{M}(\underline{\boldsymbol{u}}^k) + \mathcal{M}(\underline{\boldsymbol{u}}^i)) & 0 & 0 & \mathbb{I} & 0 \end{bmatrix}
\begin{bmatrix}
\omega^{i+1} \\
\underline{\boldsymbol{u}}^{i+1} \\
\tilde{\underline{P}}^{i+1} \\
\underline{\tilde{\lambda}}^{i+1} \\
\underline{\tilde{\gamma}}^{i+1} \\
\underline{\omega}_c^{i+1}
\end{bmatrix}
$$

$$
= \begin{bmatrix} 0 & 0.25\mathsf{M_{TF}}(\mathcal{M}(\underline{\boldsymbol{u}}^k) + \mathcal{M}(\underline{\boldsymbol{u}}^i)) & 0 & 0 & \mathbb{I} & 0 \end{bmatrix}
\begin{bmatrix}
\omega^{i} \\
\underline{\boldsymbol{u}}^{i} \\
\tilde{\underline{P}}^{i} \\
\underline{\tilde{\lambda}}^{i} \\
\underline{\tilde{\gamma}}^{i} \\
\underline{\omega}_c^{i}
\end{bmatrix}
\tag{3.39}
$$

$$
+ \underline{\tilde{\lambda}}_i + \mathsf{M_{TF}}\left[\hat{\underline{p}} + \frac{1}{2}\mathcal{M}(\frac{\boldsymbol{u}^k + \boldsymbol{u}^i}{2})(\frac{\boldsymbol{u}^k + \boldsymbol{u}^i}{2})\right] \qquad \forall \underline{\tilde{\lambda}} \in \widetilde{\mathsf{TF}}_{N-1}(\Gamma_{\hat{p}}).
$$

<div style="text-align: right; font-size: 3em;">4</div>

Numerical Experiments

In this chapter, we study the accuracy and structure-preserving capability of the hdMSEM with the novel dual grid through benchmark cases of trigonometry test, pressure-driven channel flow, backward-facing step flow, and flow over a rectangular cylinder. The cases studied cover Stokes flow, steady Navier-Stokes flow, and unsteady Navier-Stokes flow and involve boundary conditions including pressure inlet/outlet, velocity inlet, no-slip wall, and free-slip wall. The grids used in this chapter are all orthogonal, and the performance of the hdMSEM with a curvilinear grid is beyond the scope of this thesis.

4.1. Accuracy and Conservation Test

Firstly, we study Stokes equations in a square domain with an exact analytical solution to examine the accuracy and structure-preserving ability of the method.

Consider a linear system,

$$\omega - \nabla \times \boldsymbol{u} = 0, \tag{4.1a}$$

$$\nu \nabla \times \omega + \nabla p = \boldsymbol{f}, \tag{4.1b}$$

$$\nabla \cdot \boldsymbol{u} = g, \tag{4.1c}$$

in the domain $\Omega = [0,1]^2$. And the domain is discretized uniformly into K^2 elements,

$$\Omega_m = \Omega_{i+(j-1)K}, \quad i,j \in \{1, 2, ..., K\}, \tag{4.2}$$

where the Lagrange multiplier is introduced at the face between each element, thus each element is one subdomain. An example of the grid can be found in Fig. 4.1, where the blue squares stand for elements and the red squares stand for the volume degree of freedom in the element.
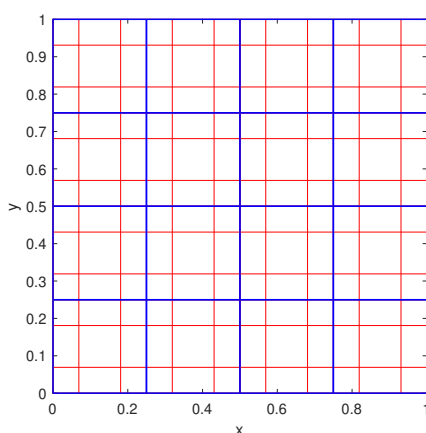

Figure 4.1: Mesh of the hdMSEM when $K = 4$ and $N = 3$.

The mapping $\boldsymbol{\Phi}_{i,j} : \Omega_{\text{ref}} \rightarrow \Omega_{i,j}$ is given as

$$\boldsymbol{\Phi}_{i,j} = \mathring{\boldsymbol{\Phi}} \circ \Xi_{i,j}, \tag{4.3}$$

where $\Xi_{i,j}$ is a linear mapping:

$$\Xi_{i,j} : \Omega_{\text{ref}} \rightarrow \left(\left[\frac{i-1}{K}, \frac{i}{K} \right], \left[\frac{j-1}{K}, \frac{j}{K} \right] \right), \tag{4.4}$$

and $\mathring{\boldsymbol{\Phi}}$ can be written as

$$\begin{pmatrix} x \\ y \end{pmatrix} = \mathring{\boldsymbol{\Phi}}(r, s) = \begin{pmatrix} r \\ s \end{pmatrix}. \tag{4.5}$$

The kinematic viscous factor ν is set as 1, and the exact solution is specified as

$$\boldsymbol{u}_{\text{exact}} = \begin{bmatrix} \cos(2\pi x)\cos(2\pi y) \\ \cos(2\pi x)\cos(2\pi y) \end{bmatrix}, \tag{4.6a}$$

$$\omega_{\text{exact}} = \nabla \times \boldsymbol{u}_{\text{exact}} = 2\pi\cos(2\pi x)\sin(2\pi y) - 2\pi\sin(2\pi x)\cos(2\pi y), \tag{4.6b}$$

$$p_{\text{exact}} = \cos(2\pi x)\cos(2\pi y). \tag{4.6c}$$

Therefore, the source term is defined as

$$\boldsymbol{f} = \begin{bmatrix} 4\pi^2\cos(2\pi x)\cos(2\pi y) + 4\pi^2\sin(2\pi x)\sin(2\pi y) - 2\pi\sin(2\pi x)\cos(2\pi y) \\ 4\pi^2\cos(2\pi x)\cos(2\pi y) + 4\pi^2\sin(2\pi x)\sin(2\pi y) - 2\pi\cos(2\pi x)\sin(2\pi y) \end{bmatrix} \tag{4.7a}$$

$$g = -2\pi\cos(2\pi x)\sin(2\pi y) - 2\pi\sin(2\pi x)\cos(2\pi y), \tag{4.7b}$$

First, we must verify that the hdMSEM with the novel dual grid can avoid the singularity problem and output results consistent with the exact solution. Fig. 4.2 presents a solution with the hdMSEM when $K = 4$ and $N = 3$, consistent with the analytical solution.

Then, the order of the accuracy is studied by refining the mesh and investigating the L^2-error of the vorticity field, velocity field, and pressure field. Choosing $N = 1, 2, 3, 4$ and $K = 4, 8, 16, 32$, the convergence performance can be found in Fig. 4.3. The convergence results prove that the errors of ω^h, $\boldsymbol{u}^h$ and p^h converge optimally with the order of the element N.

The conservation law of mass at the discrete level is maintained by the incidence matrix E_{div}, the basic topology structure of the discrete mass conservation law is one volume degree of freedom and the four face degrees of freedom around it, as illustrated in Fig. 4.4a. We can examine the discrete conservation law of mass by calculating $\|\nabla \cdot \boldsymbol{u}^h - g^h\|_{L^2}$, shown in Fig. 4.5. The error is at the level of floating-point precision. Hence, there is no discrete error introduced into the conservation law of mass in the hdMSEM.

The basic topology structure to preserve vorticity structure is more complicated than mass conservation law. As illustrated in Fig. 4.4b, the relationship between ω^h and $\boldsymbol{u}^h$ is maintained by discrete dual curl operator (2.91), besides $\boldsymbol{u}^h$, the discrete dual curl operator also requires the trace variable $\tilde{\gamma}^h$ around the element which stand for the tangential velocity at the element boundary, i.e.,

$$\widetilde{\nabla\times}(\boldsymbol{u}^h, \tilde{\gamma}^h) = \omega^h. \tag{4.8}$$

To verify the discrete dual operator, its numerical errors are computed and shown in Fig. 4.6. Obviously, only floating-point errors are introduced into the numerical solution. From this, we prove that the basic topology structure of the discrete vorticity conservation law is one element and the trace variables around the element. It can be reasoned that the Green's formula,

$$\int_\Omega \omega^h \, d\Omega = \int_\Omega \nabla \times \boldsymbol{u}^h \, d\Omega = \int_{\partial\Omega} (\boldsymbol{u} \times \boldsymbol{n})^h \, d\Gamma = \int_{\partial\Omega} \gamma^h \, d\Gamma. \tag{4.9}$$

should be maintained over the domain. Fig. 4.7 shows that the discrete Green's formula is preserved, ignoring the floating point errors.
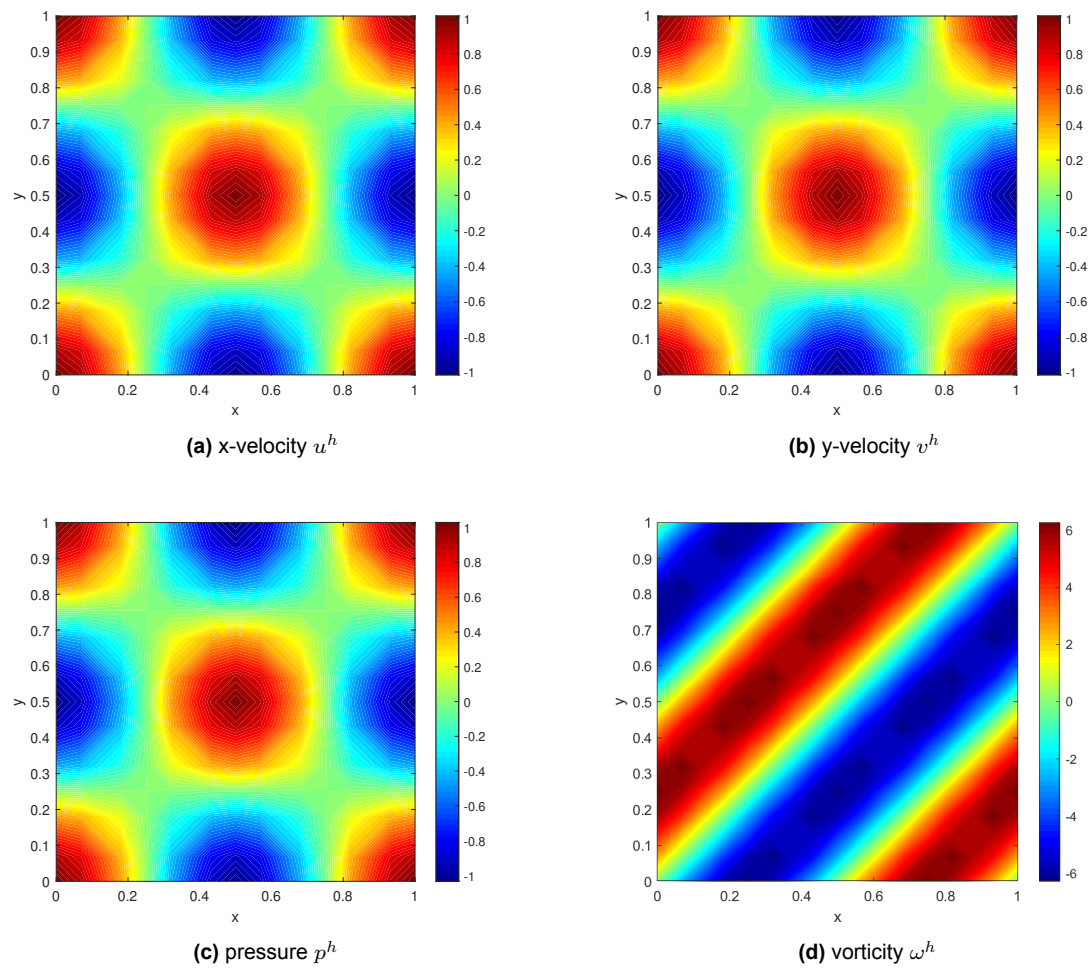
(a) x-velocity u^h

(b) y-velocity v^h

(c) pressure p^h

(d) vorticity ω^h

Figure 4.2: Numerical solution when $K = 4$ and $N = 3$.

(a) L^2-error of vorticity

(b) L^2-error of velocity

(c) L^2-error of pressure
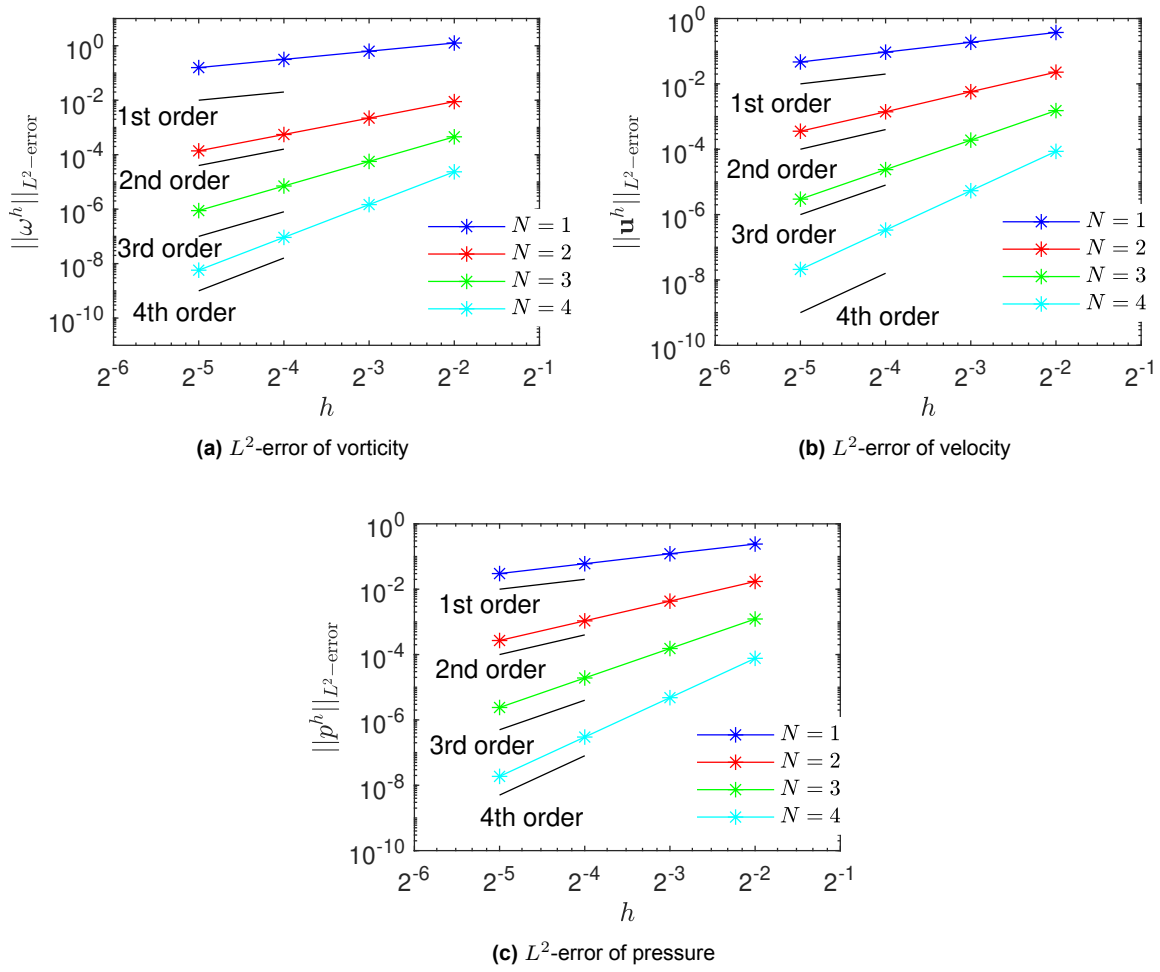
Figure 4.3: L^2-error of ω^h, $\boldsymbol{u}^h$ and p^h when $N = 1, 2, 3, 4$ and $K = 4, 8, 16, 32$.

(a) Mass conservation law

(b) Vorticity conservation law
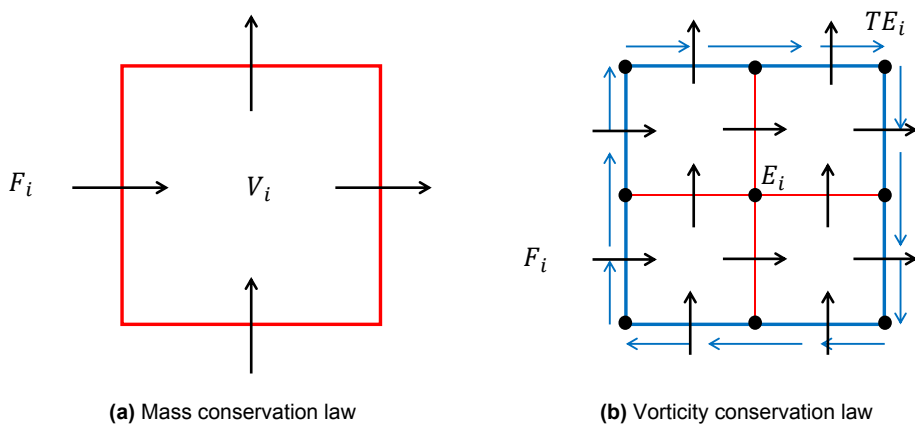
Figure 4.4: Grid topology for preserving structure.
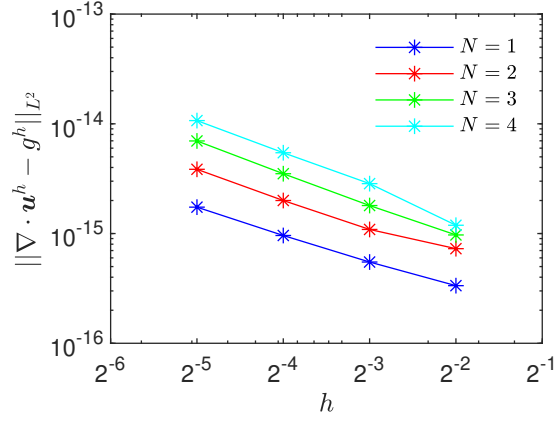
Figure 4.5: Numerical errors of the discrete mass conservation law.
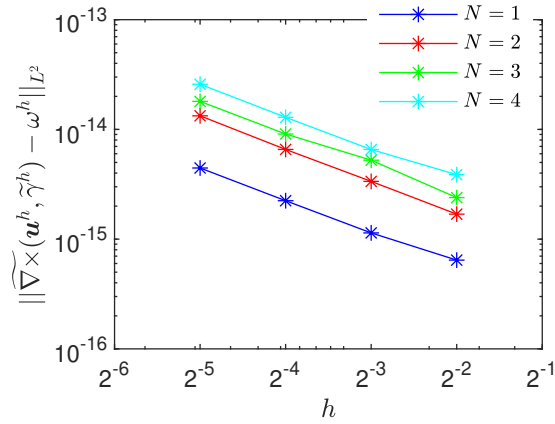
Figure 4.6: Numerical errors of the discrete dual curl operator.

In addition, we denote the matrix of the global system to solve in the hdMSEM as $\widetilde{\mathbb{S}}$ and study the condition number of $\widetilde{\mathbb{S}}$, see the result in Fig. 4.8, where k is the 2nd-norm condition number, i.e.,

$$k = ||\widetilde{\mathbb{S}}^{-1}||_2 ||\widetilde{\mathbb{S}}||_2 = \frac{\sigma_{\max}(\widetilde{\mathbb{S}})}{\sigma_{\min}(\widetilde{\mathbb{S}})}.$$

It is seen that the condition number increases with the same order as mesh refines, although the elements of different orders are chosen. It suggests the advantage in computing efficiency of the high order hdMESM and matches well with the results in [44] when solving the Poisson problem with the hdMSEM. At the same time, a comparison between the condition number with the novel dual grid (Fig. 3.1) and the primal-dual grid (Fig. 2.9) shows that the novel dual grid proposed in this thesis will not increase the condition number for certain N and K.

Finally, the rank of the global system to solve in the hdMSEM also determines the computing efficiency. We denote the global system to solve in the MSEM as $\mathbb{F}$. And the sizes of $\mathbb{F}$ and $\widetilde{\mathbb{S}}$ are denoted as $\#\mathbb{F}$ and $\#\widetilde{\mathbb{S}}$. The ratio between $\#\widetilde{\mathbb{S}}$ and $\#\mathbb{F}$ is demonstrated in Table 4.1. The hdMSEM with the novel dual grid proposed in this thesis can save computing resources efficiently compared with MSEM, especially using high-order elements, and the ratio keeps decreasing as mesh refines (unless using the first-order element).
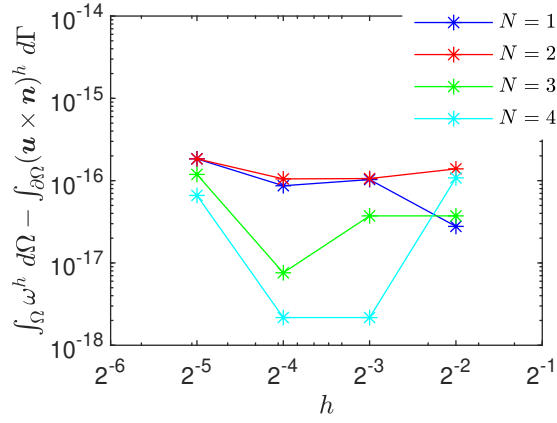
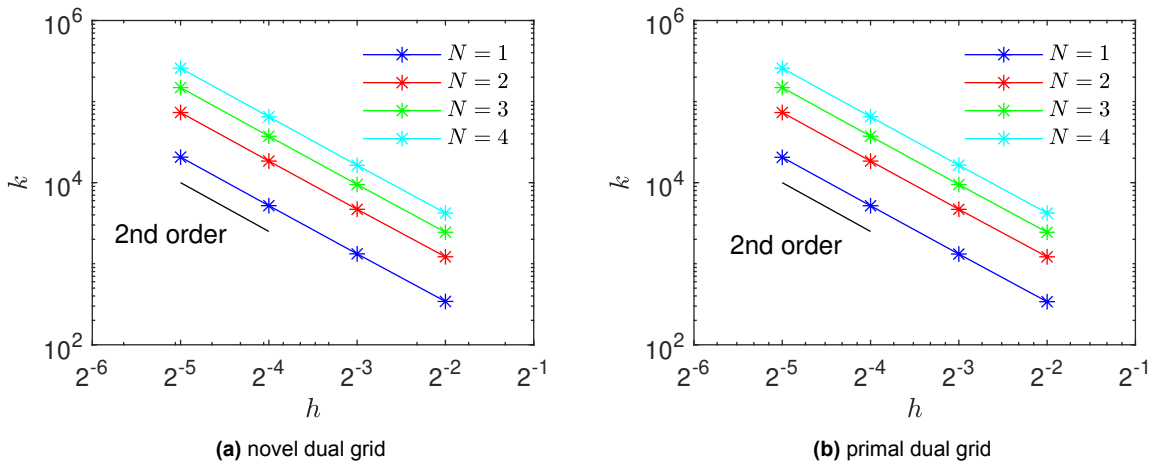**Figure 4.7:** Numerical errors of discrete the Green's formula.

(a) novel dual grid

(b) primal dual grid

Figure 4.8: Condition number k of matrix $\widetilde{\mathbb{S}}$ with the novel dual grid (3.1) and the primal dual grid (2.99).

N \ K	4	8	16	32
1	1.5926	1.6644	1.7052	1.7271
2	0.7232	0.7062	0.6970	0.6923
3	0.4624	0.4402	0.4286	0.4227
4	0.3388	0.3183	0.3077	0.3023

Table 4.1: Ratio of $\#\widetilde{\mathbb{S}}$ to $\#\mathbb{F}$, where $\#\widetilde{\mathbb{S}}$ and $\#\mathbb{F}$ are the sizes of the global system to solve in the hdMSEM with the novel dual grid and the MSEM respectively.

4.2. Pressure-driven Channel Stokes Flow

This section presents a case to solve pressure-driven channel Stokes flow using the hdMSEM with the novel dual grid. The implementations of no-slip wall boundary conditions and pressure inlet/outlet are verified. At the same time, we discuss the discrete conservation law for a grid topology near the boundary, which is more complicated than Dirichlet boundary conditions discussed in Section 4.1.

Consider the square domain $\Omega = [0,1]^2$ and a uniform mesh of K^2 elements used in Section 4.1, and the Stokes equations in velocity-vorticity-pressure formulation (4.1). There is no mass source and volume force in this case, hence $g = 0$ and $f = 0$. The physical boundary conditions setting is depicted in Fig. 4.9: The pressure at Inlet and outlet boundaries Γ_1 and Γ_2 are 1 and 0 respectively, and the tangential velocity is 0; the top and bottom boundaries Γ_3 and Γ_4 are both no-slip walls. Hence, the tangential and normal velocity are both 0.

$$\boldsymbol{u} \cdot \boldsymbol{n} = 0$$
$$\boldsymbol{u} \times \boldsymbol{n} = 0$$

$$p = 1$$
$$\boldsymbol{u} \times \boldsymbol{n} = 0$$

Γ_4

Γ_1 Γ_2

Γ_3

$$p = 0$$
$$\boldsymbol{u} \times \boldsymbol{n} = 0$$

$$\boldsymbol{u} \cdot \boldsymbol{n} = 0$$
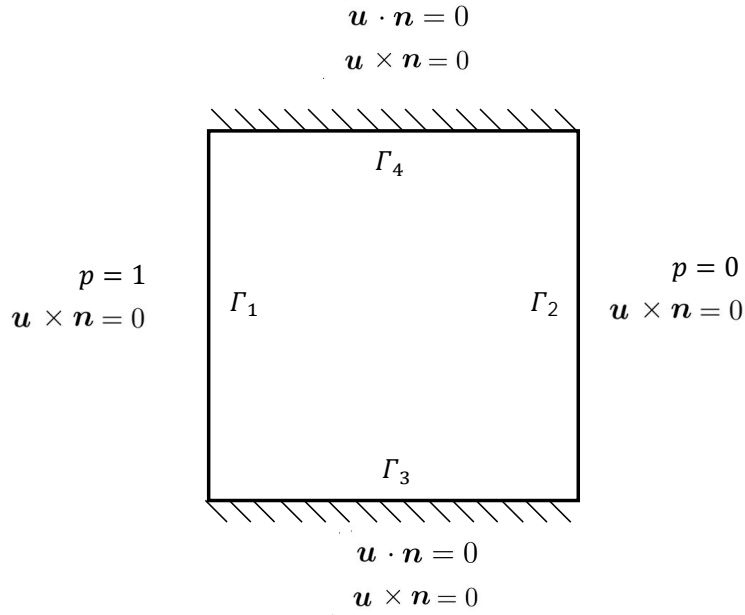$$\boldsymbol{u} \times \boldsymbol{n} = 0$$

Figure 4.9: Boundary conditions for pressure-driven channel Stokes flow.

As discussed in Section 3.2, at the boundary, the pressure is associated with λ^h, the tangential velocity is associated with γ^h, and the normal velocity is implemented with $\boldsymbol{u}^h$ and trace operator T, i.e.,

$$\tilde{\underline{\lambda}} = -\mathsf{M}_{\mathsf{TF}}(\hat{p}) \qquad \forall \tilde{\underline{\lambda}} \in \widetilde{\underline{\mathsf{TF}}}_{N-1}(\Gamma_{\hat{p}}), \tag{4.10a}$$

$$\tilde{\underline{\gamma}} = 0 \qquad \forall \tilde{\underline{\gamma}} \in \widetilde{\underline{\mathsf{TE}}}_{N}(\Gamma_{\|}), \tag{4.10b}$$

$$\mathbb{T}_{\mathsf{F}}\underline{u} = 0 \qquad \forall \tilde{\underline{\lambda}} \in \widetilde{\underline{\mathsf{TF}}}_{N-1}(\Gamma_{\perp}), \tag{4.10c}$$

where $\Gamma_{\hat{p}} = \Gamma_1 \cup \Gamma_2$, $\Gamma_{\|} = \Gamma_1 \cup \Gamma_2 \cup \Gamma_3 \cup \Gamma_4$ and $\Gamma_{\perp} = \Gamma_3 \cup \Gamma_4$.

The analytical solution of this case is easy to derive: In domain $\Omega = [0,1]^2$, there is

$$\begin{cases} p = 1 - x \\ u = \dfrac{1}{2\nu}(-y^2 + y) \\ v = 0 \\ \omega = \dfrac{1}{2\nu}(2y - 1) \end{cases}, \tag{4.11}$$

where ν is the kinematic viscosity.

Choosing $N = 3$, $K = 4$ and 8 and $\nu = 1, 2$ and 5, comparisons between the numerical solution using the hdMSEM with the novel dual grid and the analytical solution is demonstrated in Fig. 4.11 and 4.12.
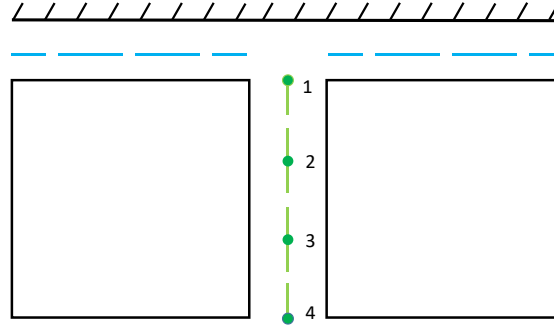
Figure 4.10: Trace degrees of freedom near no-slip wall boundary when $N = 3$: Green lines stand for trace degrees of freedom at the interface perpendicular to the boundary and noted as $\tilde{\gamma}_{1,2,3,4}$ and green nodes stand for the primal trace degrees of freedom $\gamma_{1,2,3,4}$.

The results show that the discrete solutions u^h, ω^h, and p^h are consistent with the analytic solutions at the boundary and inside the domain. Because the analytical solutions are functions of order up to 2, the 3rd-order element can exactly reconstruct the analytical solution, and therefore, there are no discrete errors for both $K = 4$ and 8.

In Section 3.2, we claimed that no boundary condition needs to be posed on the trace degree of freedom $\tilde{\gamma}$ which is at the interface Γ perpendicular to the boundary, illustrated in Fig. 4.10. According to the definition of trace variable $\gamma = \boldsymbol{u} \times \boldsymbol{n}$, $\gamma = \mathsf{M}_{\mathsf{TE}}^{-1}\tilde{\gamma}$ should equal to 0 exactly at the wall boundary to satisfy the zero normal velocity condition. Take the case when $N = 3$ shown in Fig. 4.10 for example, no boundary condition is posed on $\tilde{\gamma}_{1,2,3,4}$, while there is the algebraic relation, $[\gamma_1, \ \gamma_2, \ \gamma_3, \gamma_4]^\mathsf{T} = \mathsf{M}_{\mathsf{TE}}^{-1}[\tilde{\gamma}_1, \ \tilde{\gamma}_2, \ \tilde{\gamma}_3, \tilde{\gamma}_4]^\mathsf{T}$, and γ_1 should exactly equal to 0 according to its physical meaning. We examine it by plotting the $\mathsf{M}_{\mathsf{TE}}^{-1}\tilde{\gamma}$ along boundary, see in Fig. 4.13. The results show that the dual trace degrees of freedom meet the zero normal velocity condition up to machine precision. At the same time, the trace variable at the interface perpendicular to the inlet/outlet is consistent with the velocity profile at the inlet/outlet. Having proved the physical meaning represented by the dual trace degrees of freedom $\tilde{\gamma}$ at the boundary, it is evident to reason that the discrete conservation law of mass and vorticity is still preserved in this case, see numerical confirmation in Fig. 4.14.
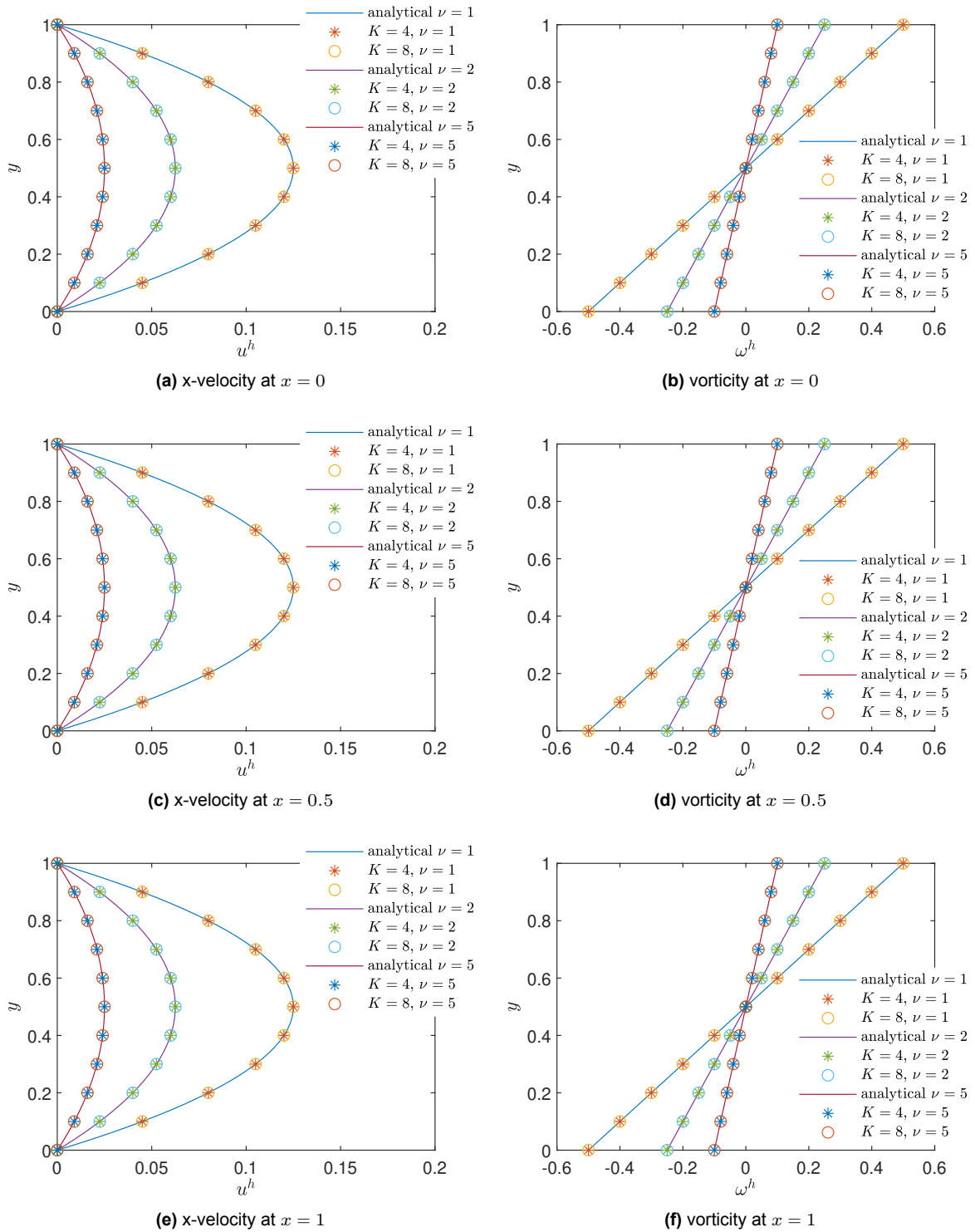
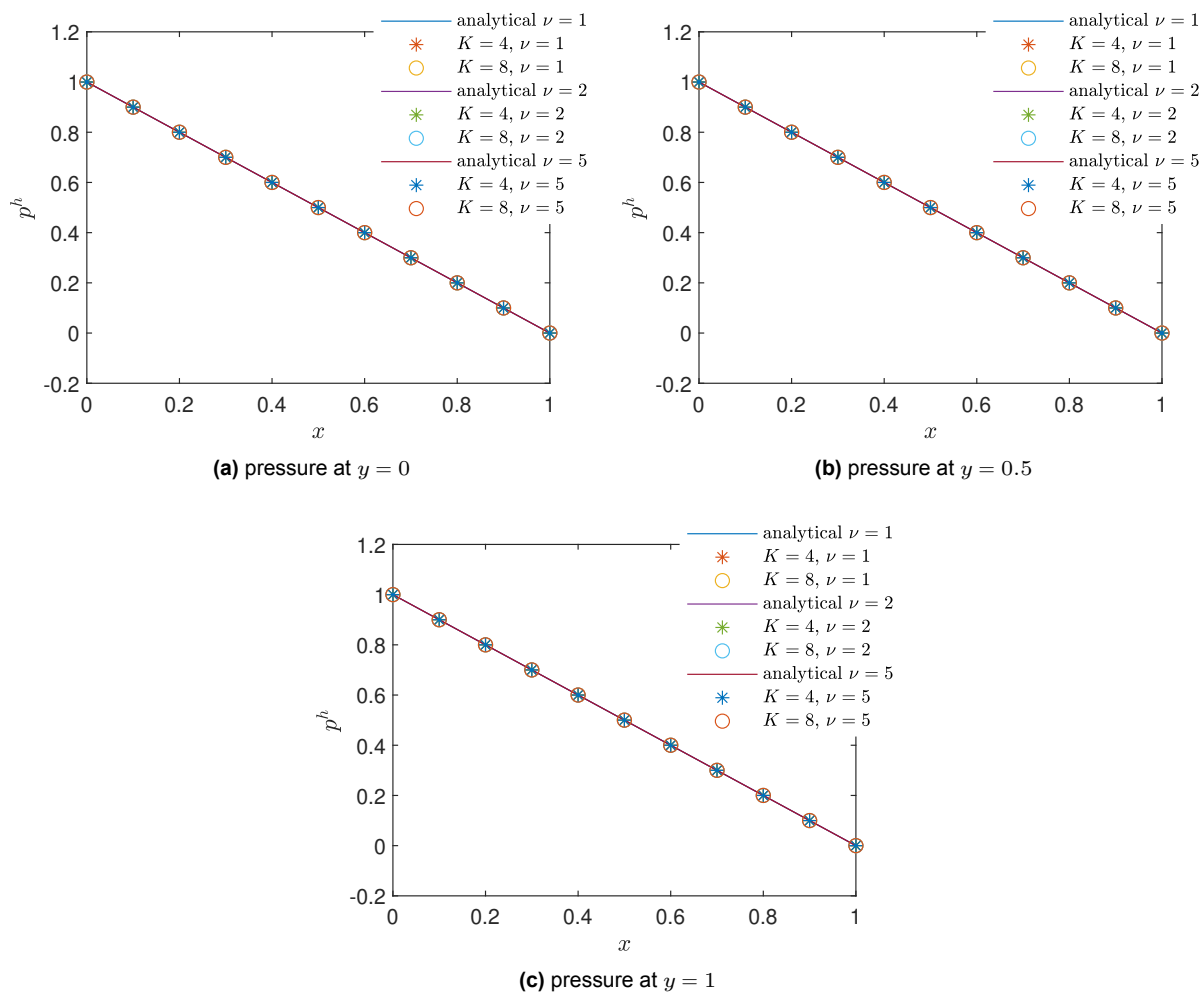**Figure 4.11:** Profiles of u^h and ω^h, where $N = 3$.

(a) pressure at $y = 0$

(b) pressure at $y = 0.5$

(c) pressure at $y = 1$

Figure 4.12: Profiles of p^h, where $N = 3$.
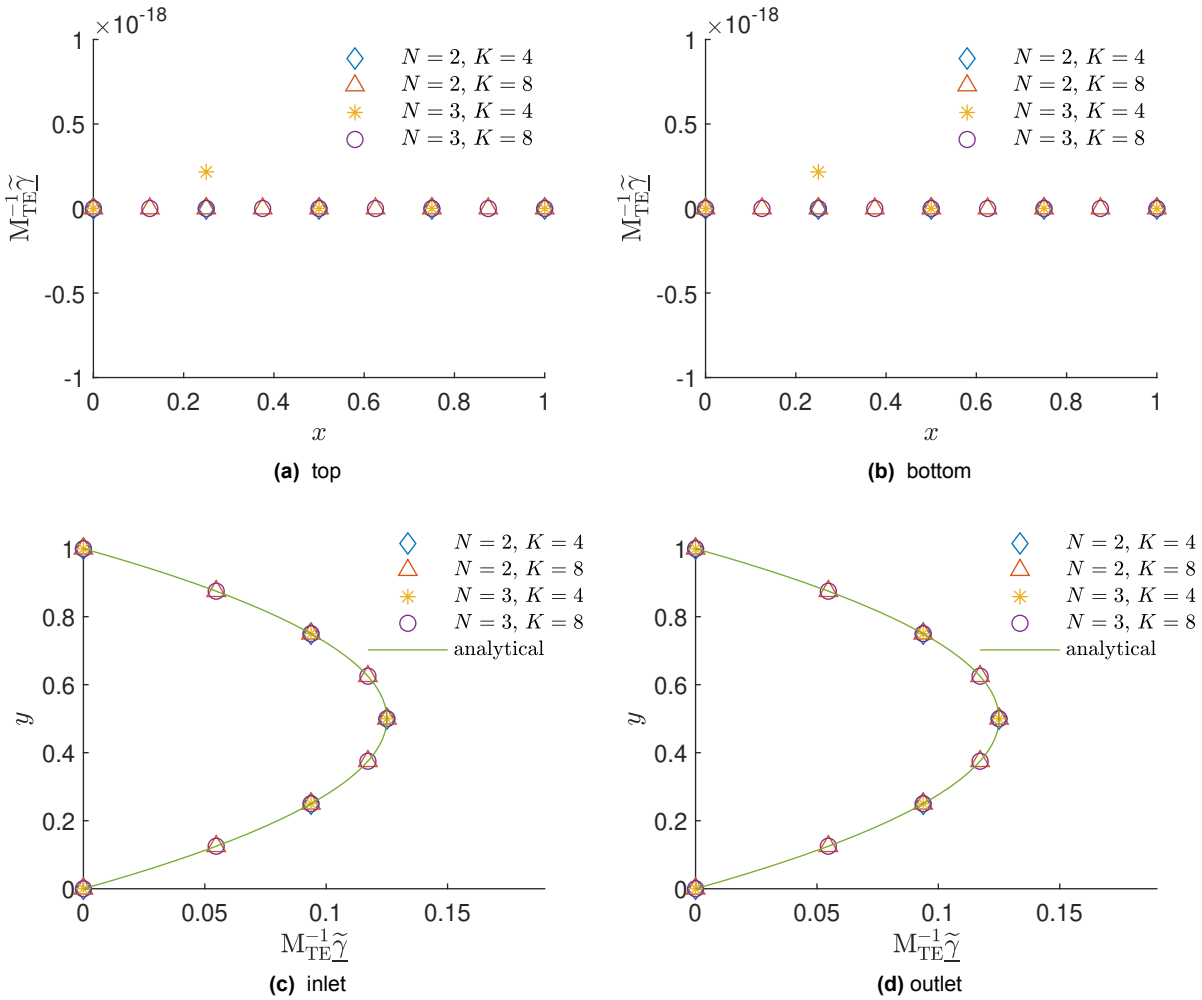
Figure 4.13: Values of $\mathrm{M}_{\mathrm{TE}}^{-1}\underline{\widetilde{\gamma}}$ along boundaries when $\nu = 1$, $N = 2, 3$ and $K = 4, 8$.

(a)

(b)

(c)
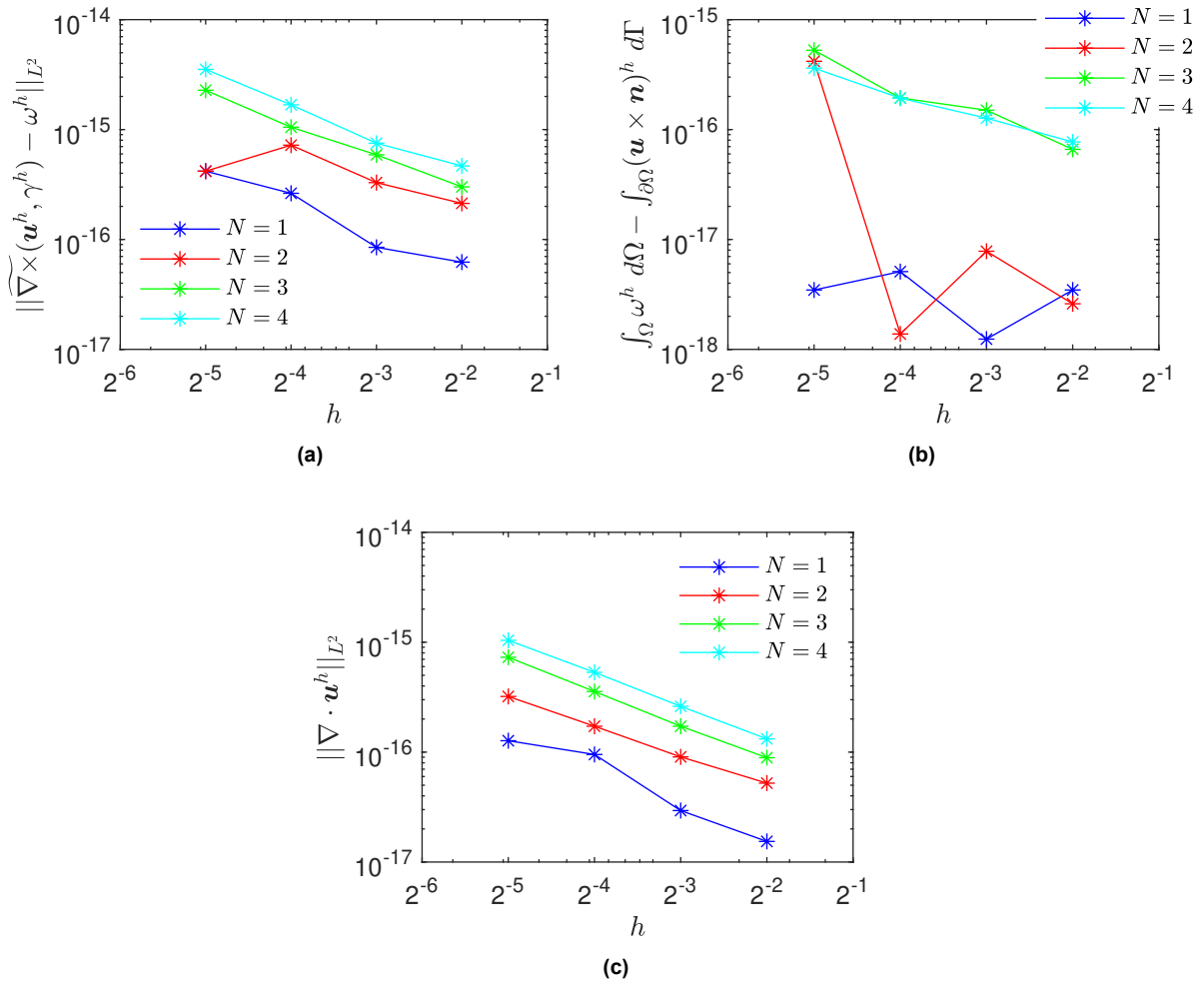
Figure 4.14: $L^2 - $ norm of $\widetilde{\nabla \times}(\boldsymbol{u}^h, \gamma^h) - \omega^h$, $\int_\Omega \omega^h \, d\Omega - \int_{\partial\Omega}(\boldsymbol{u} \times \boldsymbol{n})^h \, d\Gamma$ and $\nabla \cdot \boldsymbol{u}^h$ when $\nu = 1$, $N = 1, 2, 3, 4$ and $K = 4, 8, 16, 32$.

4.3. Backward-facing Step Stokes Flow

Based on the pressure-driven channel flow case, we introduce a right-angle boundary and study the grid topology near the boundary. To simplify the problem, the convective term is ignored for the moment. Therefore the problem we solve is still the Stokes equations in the velocity-vorticity-pressure formulation (4.1), and choose $\nu = 1$, $g = 0$ and $\boldsymbol{f} = 0$.

The geometry of domain and boundary conditions are illustrated in Fig. 4.15, where L_{in} is the length of the inlet channel, L is the length of the main channel, h is the height of the inlet channel, and H is the height of the main channel. The horizontal position of the inlet is $x = 0$, and the vertical position of the bottom wall of the main channel is $y = 0$. In this case, we set $L_{in} = 1$, $L = 4$, $h = 1$ and $H = 2$. The top, bottom, and the step face of the channel are all no-slip walls, a constant pressure 0 is assigned to the outlet uniformly, and the normal velocity is specified as a parabolic function at the inlet,

$$\hat{u}_\perp(y') = 6y'(1 - y'), \tag{4.12}$$

where y' is the height from the bottom wall of the inlet channel, i.e., $y' = y - (H - h)$. This parabolic function satisfies the no-slip condition at the top and bottom wall and ensures the average inlet velocity is 1.
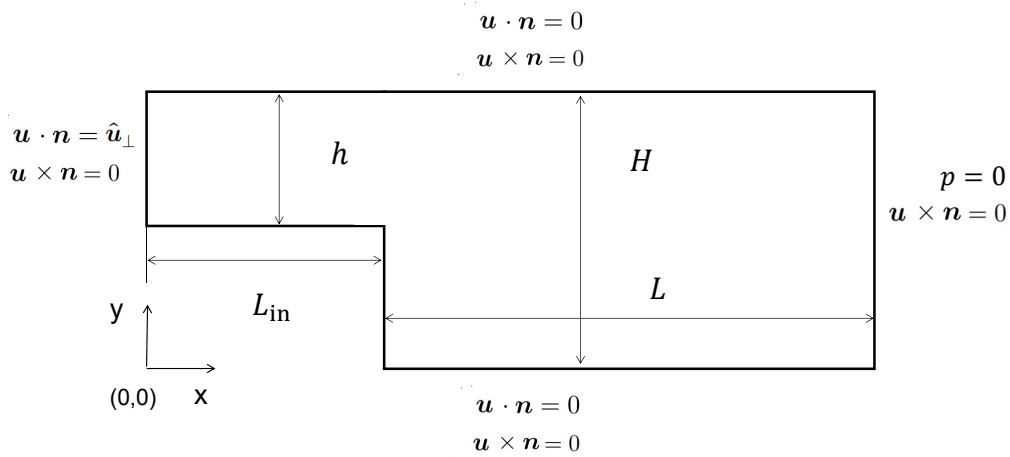

Figure 4.15: The domain and boundary conditions for backward-facing step Stokes flow.
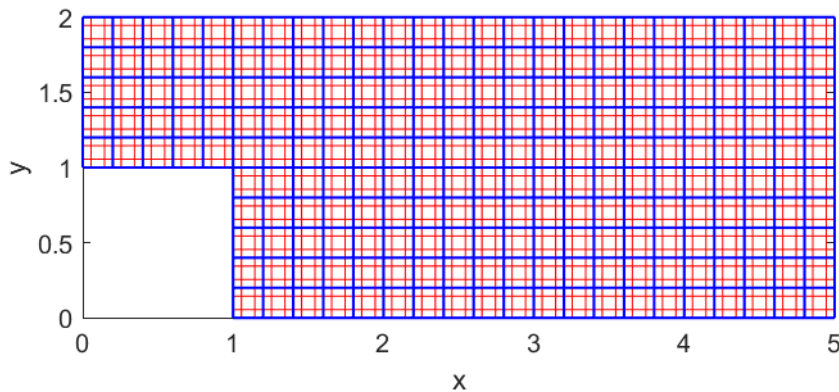

Figure 4.16: Grid for backward-facing step flow, when $N = 3$, $h = 1/5$ and the total numbder of elements is 225.

The implementation of boundary conditions in matrix formulation can be written as

$$\underline{\tilde{\lambda}} = 0 \qquad \forall \underline{\tilde{\lambda}} \in \widetilde{\underline{\mathsf{TF}}}_{N-1}(\Gamma_{\hat{p}}), \tag{4.13a}$$

$$\underline{\tilde{\gamma}} = 0 \qquad \forall \underline{\tilde{\gamma}} \in \widetilde{\underline{\mathsf{TE}}}_{N}(\Gamma_{\|}), \tag{4.13b}$$

$$\mathbb{T}_{\mathsf{F}} \boldsymbol{u} = 0 \qquad \forall \underline{\tilde{\lambda}} \in \widetilde{\underline{\mathsf{TF}}}_{N-1}(\Gamma_{\perp}), \tag{4.13c}$$

$$\mathbb{T}_{\mathsf{F}} \boldsymbol{u} = \underline{\hat{u}_{\perp}} \qquad \forall \underline{\tilde{\lambda}} \in \widetilde{\underline{\mathsf{TF}}}_{N-1}(\Gamma_{\mathsf{inlet}}), \tag{4.13d}$$

and the implementation of no-slip conditions near right-angled boundaries is discussed in detail in Section 3.2, see Fig. 3.3b.

The domain is discretized with uniform grids, where the size of element $\Delta x = \Delta y = h$ and the order is N. An example of the grid is given in Fig. 4.16, when $h = 1/5$ and $N = 3$. The numerical solutions are demonstrated in Fig. 4.17 with a grid of $N = 3$ and $h = 1/20$. In addition, the solutions on the grid of $N = 3$ and $h = 1/5$ can be found in Appendix A.

The hdMSEM with the novel dual grid outputs physical solutions, while there is an issue in backward-facing step flow, which deserves highlighting: As the definition of vorticity is

$$\omega = \frac{\partial v}{\partial x} - \frac{\partial u}{\partial y}, \tag{4.14}$$

the vorticity value at the corner boundary is physically infinite as there is a discontinuity of y-velocity v. In traditional CFD solvers, which only have a discrete flow field in the pressure-velocity field, this singularity of vorticity is not an issue in numerical computing; however, in the framework of the hdMSEM, there is a degree of freedom directly associated with the vorticity at the corner, and due to the discrete error, its value cannot be infinite. Fig. 4.18 shows the singularity in the discrete vorticity field at the corner when $N = 3$ and $h = 1/20$. The following part will discuss whether this singularity breaks the consistency of the global solution and the vorticity conservation law.

We set $h = 1/10, 1/20$ and $N = 3, 4$ and the profiles of u^h, v^h, ω^h and p^h at $x' = 0$ are presented in Fig. 4.19, where x' is the distance from the left starts of the main channel, i.e., $x' = x - L_{in}$. Obviously, the singularity only creates significant errors near the corner in the numerical solution of vorticity field ω^h, and the numerical solution converges to the exact value ∞ with mesh refinement. At the same time, the singularity has little influence on the numerical solution of the velocity field $\boldsymbol{u}^h$. Besides, the discontinuity of y-velocity field v results in slight oscillation near the corner in the discrete field v^h, which is less apparent when the spatial step h is more minor. These numerical solutions demonstrates that the natural form of the hdMSEM with the novel dual grid can deal with the singularity stably without introducing any damping term.
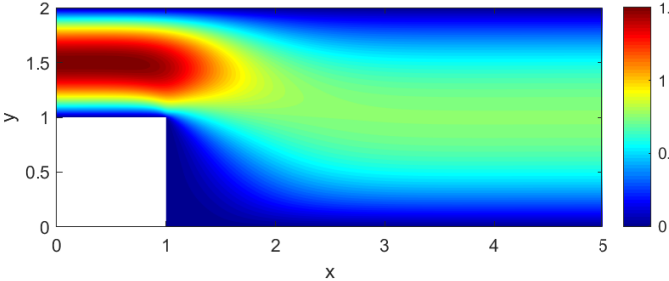
In addition, we set $N = 1, 2, 3, 4$ and $h = 1/5, 1/10, 1/20, 1/40$ and study the conservation law of mass and vorticity. The results in Fig. 4.20 demonstrate that the discrete conservation of mass and vorticity can still be preserved even though there is a physical singularity.
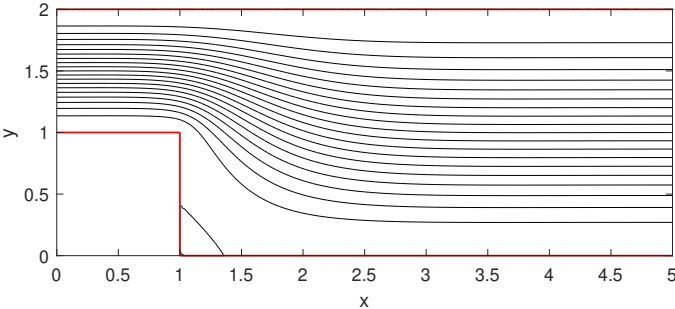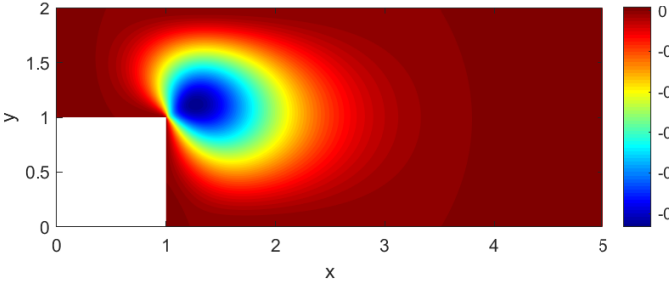
(a) stream function
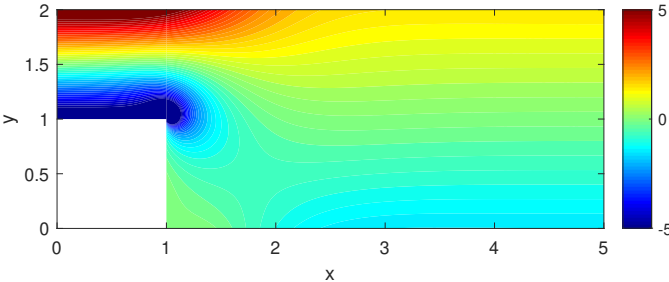
(b) vorticity

(c) x-velocity

(d) y-velocity

Figure 4.17: Numerical solution of stream function, vorticity, x-velocity and y-velocity, when $N = 3$ and $h = 1/20$.
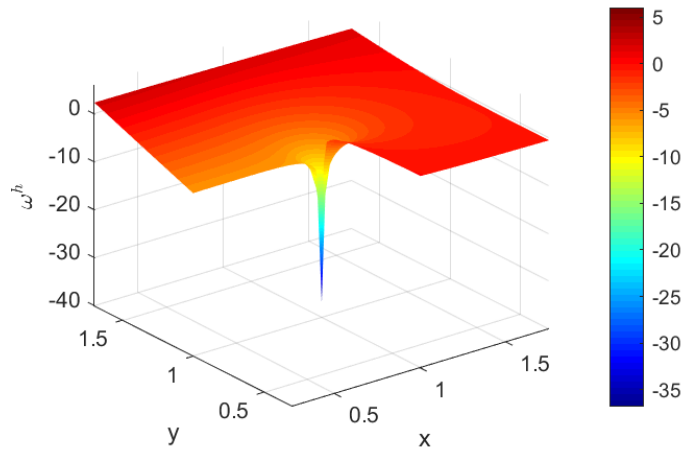
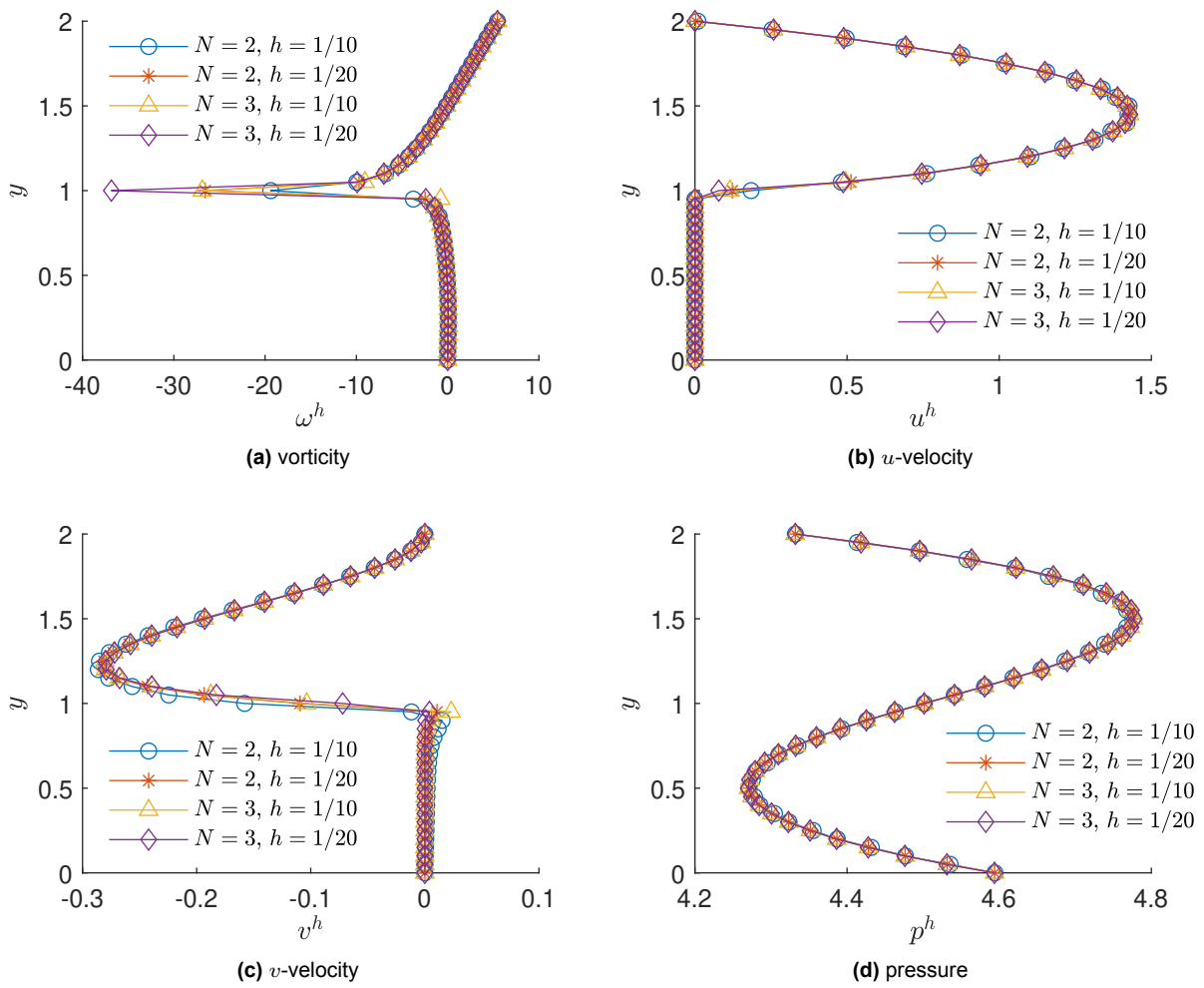**Figure 4.18:** Singularity of vorticity at the corner, when $N = 3$ and $h = 1/20$.

(a) vorticity

(b) u-velocity

(c) v-velocity

(d) pressure

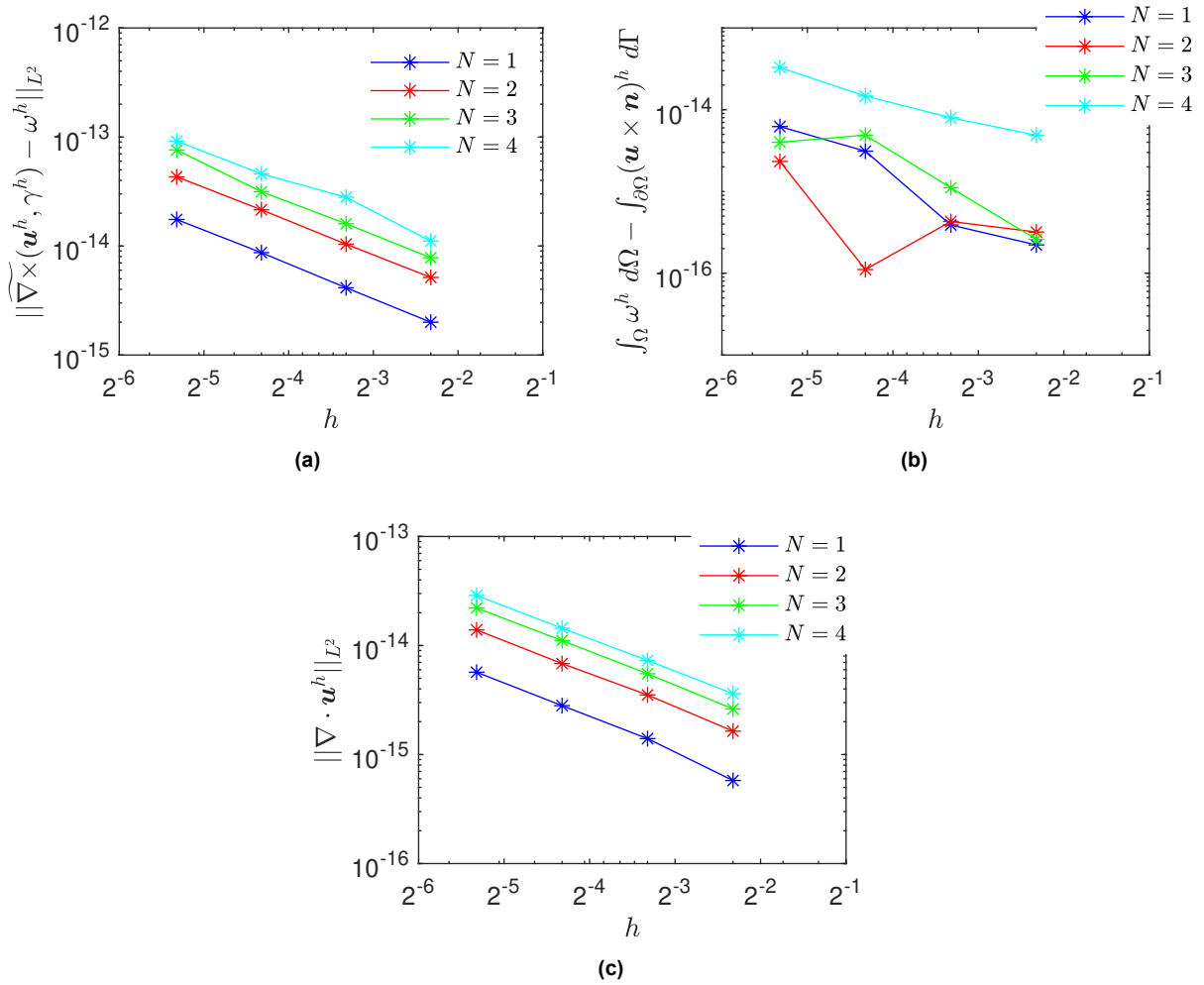**Figure 4.19:** Profiles of ω, u, v and p at $x' = 0$

Figure 4.20: L^2- norm of $\widetilde{\nabla\times}(\boldsymbol{u}^h,\gamma^h)-\omega^h$, $\int_\Omega \omega^h\,d\Omega - \int_{\partial\Omega}(\boldsymbol{u}\times\boldsymbol{n})^h\,d\Gamma$ and $\nabla\cdot\boldsymbol{u}^h$ for backward-facing step Stokes flow when $N=1,2,3,4$ and $h=1/5,1/10,1/20,1/40$.

4.4. Backward-facing Step Navier-Stokes Flow

As the hdMSEM with the novel dual grid has proven to solve backward-facing step Stokes flow in the last section, the nonlinear convective term is introduced into the problem, and the Navier-Stokes equations in the velocity-vorticity-pressure formulation can be written as

$$\omega - \nabla \times \boldsymbol{u} = 0, \tag{4.15a}$$

$$\partial_t \boldsymbol{u} + \omega \times \boldsymbol{u} + \nu \nabla \times \omega + \nabla P = \boldsymbol{f}, \tag{4.15b}$$

$$\nabla \cdot \boldsymbol{u} = g, \tag{4.15c}$$

where now P is the total pressure, i.e, $P = \frac{1}{2}\boldsymbol{u}^2 + p$, and in this section, we set $\boldsymbol{f} = 0$ and $g = 0$. The domain geometry and boundary conditions are demonstrated in Fig. 4.21, where $h = 1, H = 2, L_{\text{in}} = 20$ and $L = 60$. Different from the boundary setting in Section 4.3, there is no tangential velocity needs to be specified at the pressure outlet for the Navier-Stokes equations, and the static pressure condition should be expressed as $P - \frac{1}{2}\boldsymbol{u}^2 = 0$. The implementation of the static pressure outlet in matrix formulation can be expressed as

$$
\begin{aligned}
\tilde{\underline{\lambda}} &= -\mathsf{M}_{\mathsf{TF}}(\hat{\underline{p}} + \frac{1}{2}\mathcal{M}(\underline{\boldsymbol{u}})\underline{\boldsymbol{u}}) & \forall \tilde{\underline{\lambda}} \in \widetilde{\underline{\mathsf{TF}}}_{N-1}(\Gamma_{\hat{p}}), \\
\tilde{\underline{\gamma}} &= \mathsf{M}_{\mathsf{TE}}\mathcal{M}_{\|}\underline{\boldsymbol{u}} & \forall \tilde{\underline{\gamma}} \in \widetilde{\underline{\mathsf{TE}}}_N(\Gamma_{\|}),
\end{aligned}
\tag{4.16}
$$

see the discussion in Section 3.2.4. The normal velocity function at the inlet is (4.12), with which the average inlet velocity is 1.
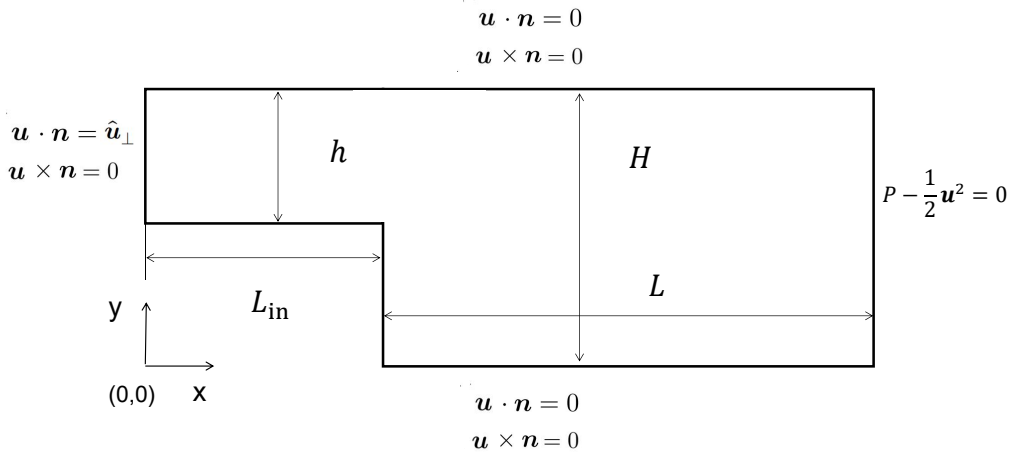

Figure 4.21: The domain and boundary conditions for backward-facing step Navier-Stokes flow.

The grid used in this section is a uniform orthogonal grid with the element size $\Delta x = h_x = 0.5$ and $\Delta y = h_y = 0.1$, and the order of the element $N = 3$. The grid's topology is the same as the one in Section 4.3, illustrated in Fig. 4.16.

The pressure-linked pseudo time stepping method (3.24) proposed in Section 3.3.2 is used to solve the nonlinear discrete system. The pseudo time step size $\Delta t = 10^{-3}$ and the convergence criterion is chosen as $||\underline{x}^k - \underline{x}^{k-1}||_{L^0} < 10^{-7}$, where $\underline{x}^k$ is the vector of all degrees of freedom at pseudo time step k, i.e.,
$\underline{x}^k = \left[\underline{\omega}^k \ \underline{\boldsymbol{u}}^k \ \tilde{\underline{P}}^k \ \tilde{\underline{\gamma}}^k \ \tilde{\underline{\lambda}}^k \ \underline{\omega_c}^k\right]^{\mathsf{T}}$.

Define the Reynolds number Re_H as

$$Re_H = \frac{H\overline{u_{\perp}}}{\nu}, \tag{4.17}$$

where $H = 2$ is the height of the main channel and $\overline{u_{\perp}} = 1$ is the average velocity at the inlet. The numerical solutions when $Re_H = 800$ are demonstrated in Fig. 4.22, and in Fig. 4.22, we compare the profiles of flow fields at $x' = 6$, $x' = 14$ and $x' = 30$ with the solution computed in a very fine grid, given in the study of Erturk [52], where the x' is the distance from the starts of the main channel, i.e., $x' = x - L_{in}$. In
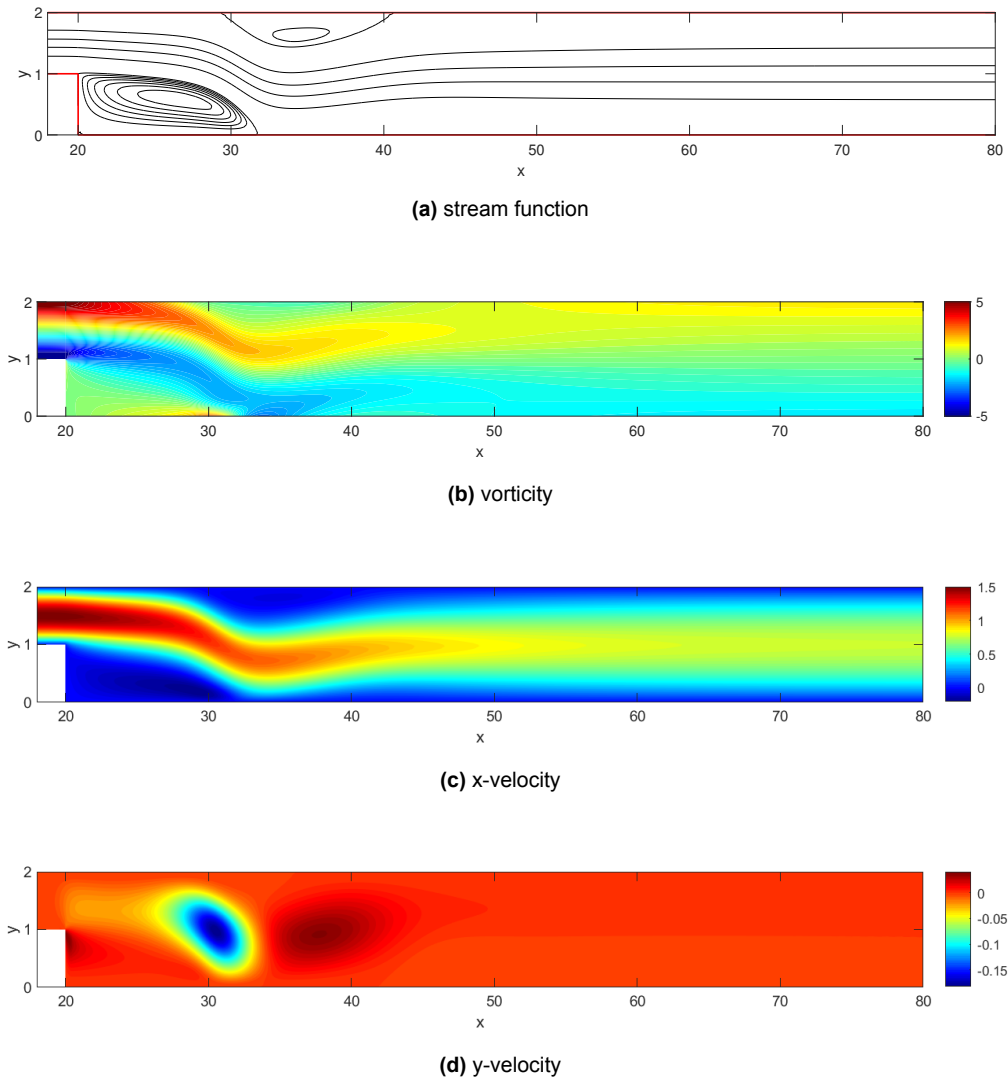
(a) stream function

(b) vorticity

(c) x-velocity

(d) y-velocity

**Figure 4.22:** Numerical solution of stream function, vorticity, u-velocity and v-velocity at $Re_H = 800$.

the comparison, our solutions match very well at $x' = 6$ and $x' = 30$ while having a slight difference of y-velocity at $x' = 14$.

Besides, we can verify the solution by comparing the position of the recirculating regions. Shown in the Fig. 4.23, the right end position of the recirculating region at the bottom is denoted as $X1$, and the left start position and the right end position of the recirculating region at the top are denoted as $X2$ and $X3$ respectively. A comparison between the present solution and the reference solutions is demonstrated in Table 4.2.

In Fig. 4.24, we present the profiles of ω^h, u^h, v^h and P^h at $x' = 0$. For the Navier-Stokes flow, there is a discontinuity at the corner instead of a singularity, which does not break the consistency of the global flow field solution in the framework of the hdMSEM with the novel dual grid. In addition, the verification of conservation laws of mass and vorticity in the pseudo time stepping is shown in Fig. 4.25.
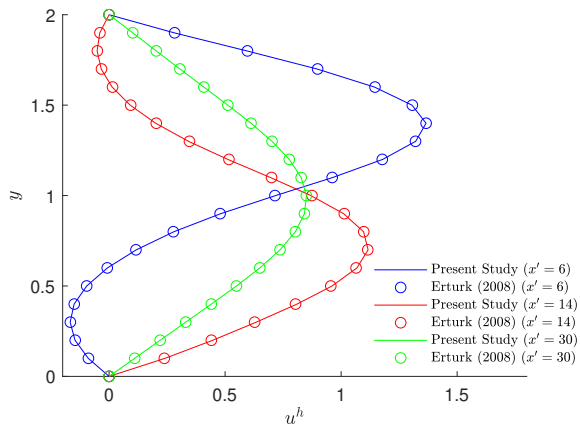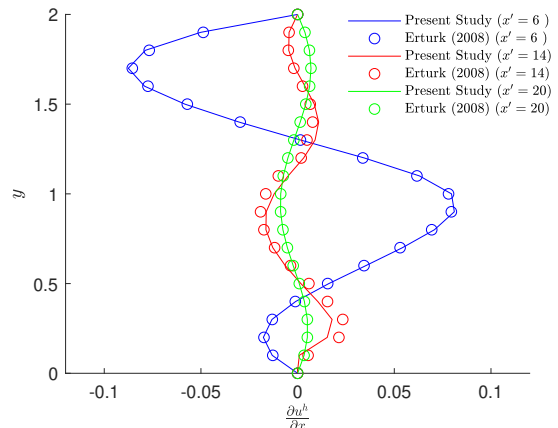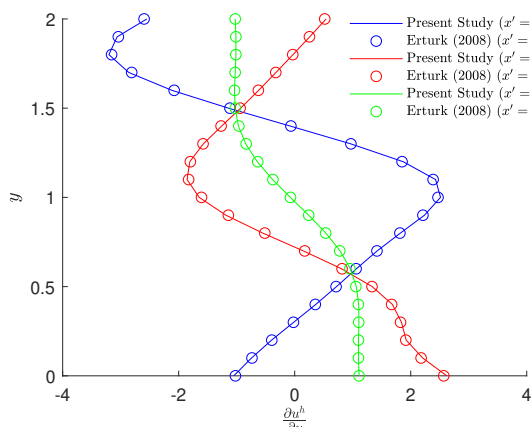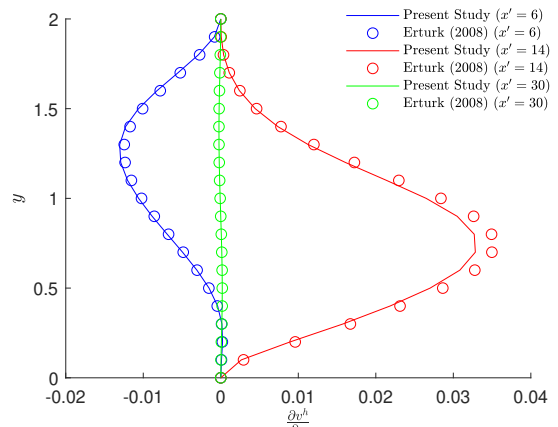
(a) x-velocity
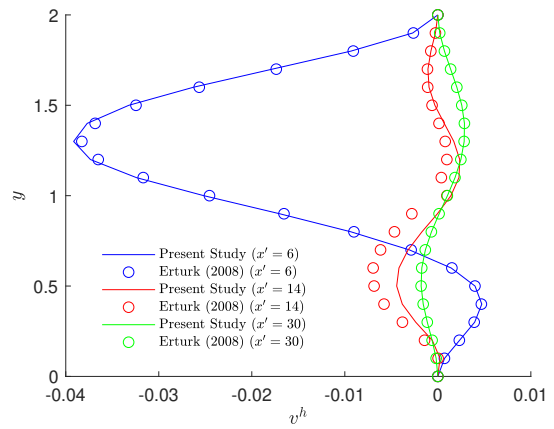
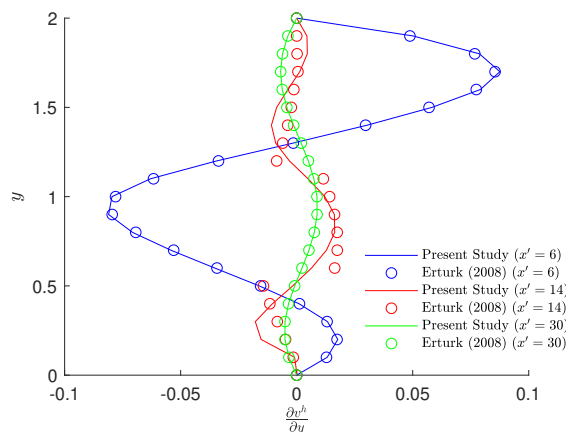**(b)** y-velocity
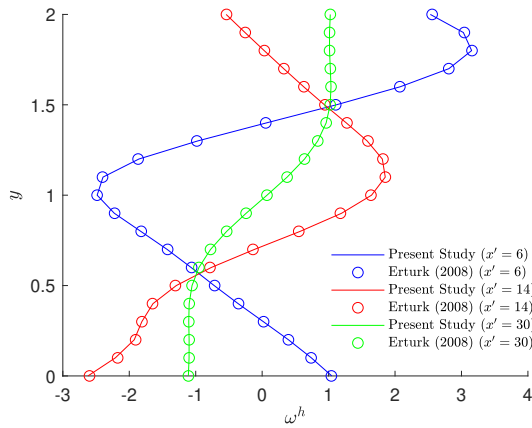
(c) vorticity

(d) horizontal gradient of x-velocity

(e) vertical gradient of x-velocity

(f) horizontal gradient of y-velocity

(g) verttical gradient of y-velocity

Figure 4.22: Profiles of u^h, v^h, ω^h, $\frac{\partial u^h}{\partial x}$, $\frac{\partial u^h}{\partial y}$, $\frac{\partial v^h}{\partial x}$, $\frac{\partial v^h}{\partial x}$ and $\frac{\partial v^h}{\partial y}$ at $Re_H = 800$.
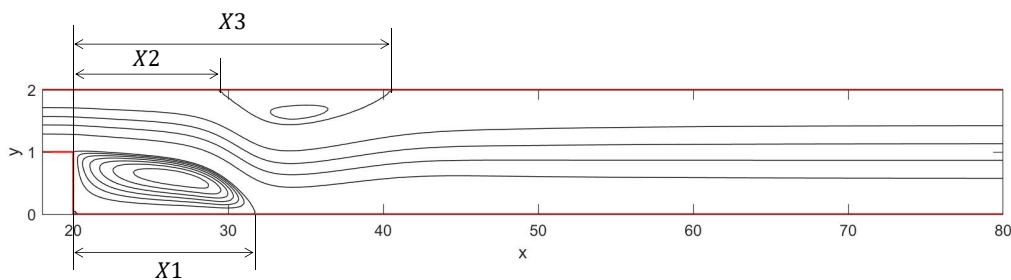

Figure 4.23: Comparison of $X1$, $X2$, $X3$ and $X3 - X2$ of the recirculating regions

	$X1$	$X2$	$X3$	$X3 - X2$
present study	11.86	9.36	20.64	11.28
Erturk [52]	11.834	9.476	20.553	11.077
Gartling [53]	12.20	9.70	20.96	11.26
Guj and Stella [54]	12.05	9.70	20.30	10.60

Table 4.2: Position of the recirculating regions

(a) vorticity

(b) u-velocity

(c) v-velocity

(d) pressure
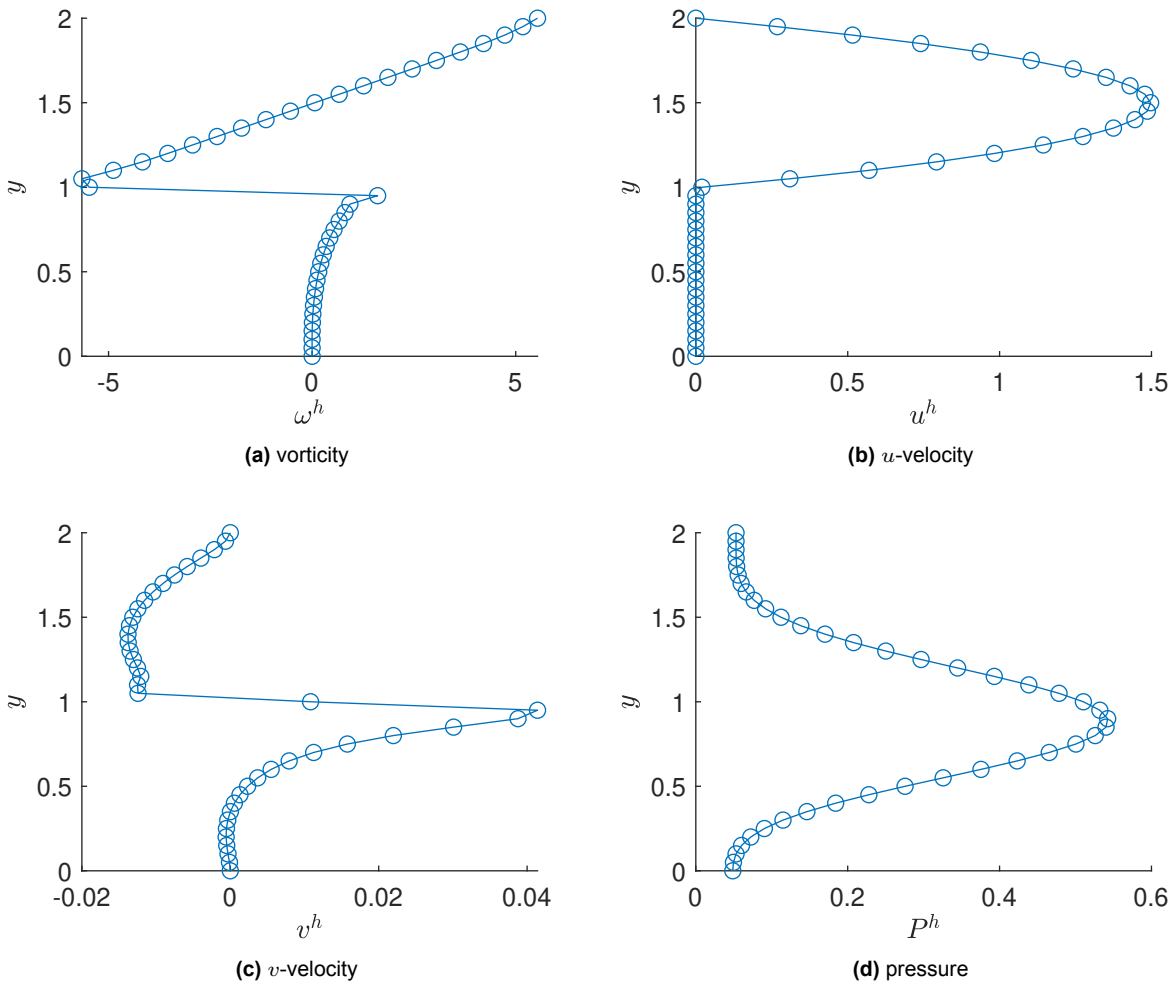
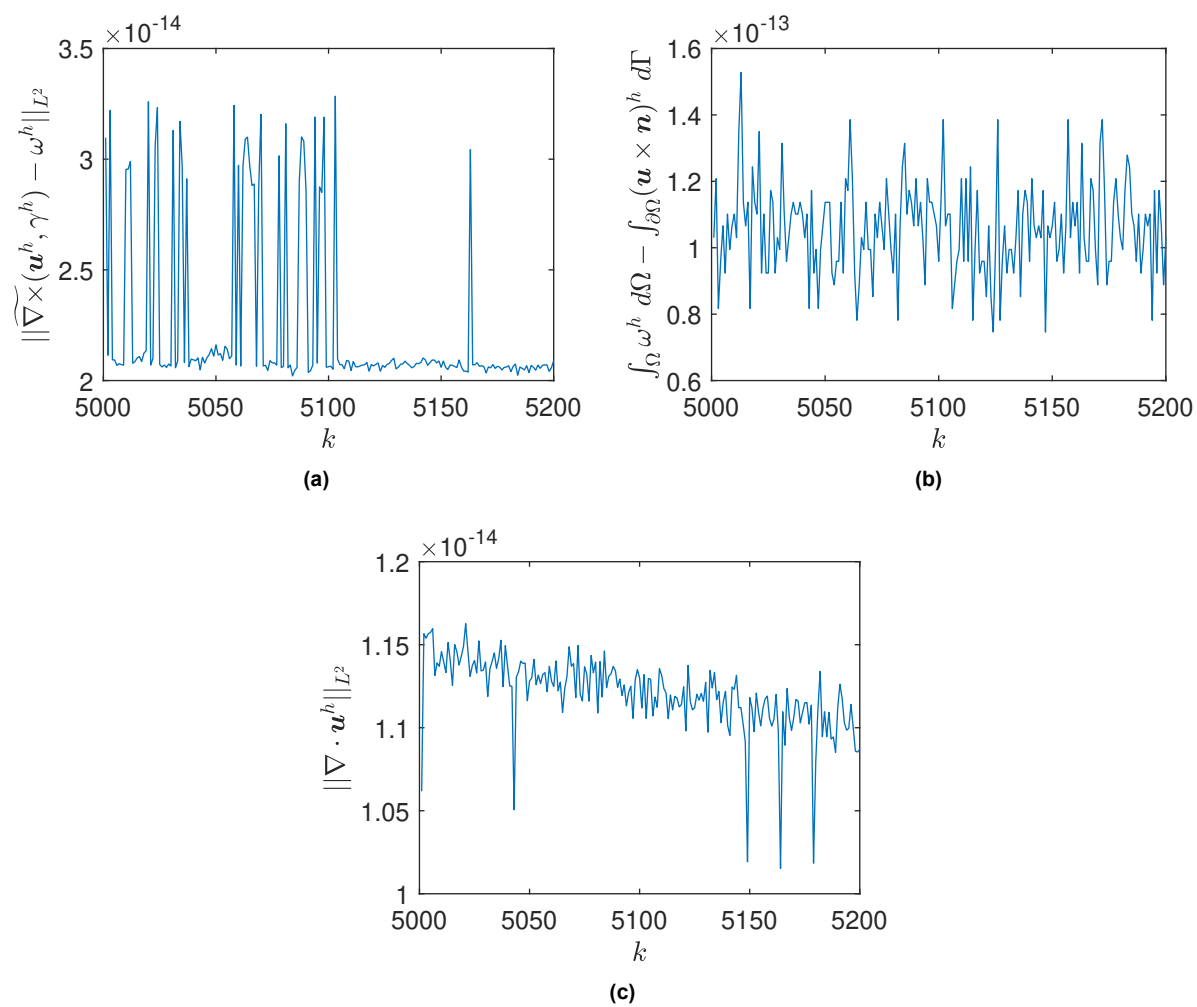**Figure 4.24:** Profiles of ω^h, u^h, v^h and P^h at $x' = 0$

Figure 4.25: $L^2 - $ norm of $\widetilde{\nabla \times}(\boldsymbol{u}^h, \gamma^h) - \omega^h$, $\int_\Omega \omega^h \, d\Omega - \int_{\partial\Omega}(\boldsymbol{u} \times \boldsymbol{n})^h \, d\Gamma$ and $\nabla \cdot \boldsymbol{u}^h$ where k is the number of pseudo time step.

4.5. Flow over Rectangular Cylinder

In this case, the mass, energy, enstrophy, and vorticity conserving (MEEVC) scheme is implemented in the framework of the hdMSEM with the novel dual grid to simulate the unsteady Navier-Stokes flow. We study the flow over rectangular cylinder cases with different Reynolds numbers to investigate the performance of the numerical scheme. In the global domain Ω, consider the Navier-Stokes equations in the vorticity-velocity-pressure formulation (4.15), and set $g = 0$ and $\boldsymbol{f} = 0$. The geometry of the domain and the boundary conditions are illustrated in Fig. 4.26, where R is the width of the channel, D is the width of the rectangular cylinder, W is the length of the rectangular cylinder, and L_1 and L_2 are the length of the upstream and downstream region respectively. In this thesis, we set $D = 1$ and $W = 0.5$, and for the size of the channel, $R = 18$, $L_1 = 9$ and $L_2 = 25$, which have ignorable boundary effect to the flow field in the study of Sohankar et al. [55].

The normal velocity at the inlet is specified as $\boldsymbol{u} \cdot \boldsymbol{n} = 1$ and the tangential velocity $\boldsymbol{u} \times \boldsymbol{n} = 0$; the top and bottom boundaries of the channel are free-slip walls which means the normal velocity $\boldsymbol{u} \cdot \boldsymbol{n} = 0$ and vorticity at wall $\omega = 0$; the four faces of the rectangular cylinder are no-slip walls where $\boldsymbol{u} \cdot \boldsymbol{n} = 0$ and $\boldsymbol{u} \times \boldsymbol{n} = 0$; the static pressure at the outlet is set as 0, i.e., $P - \frac{1}{2}\boldsymbol{u}^2 = 0$.
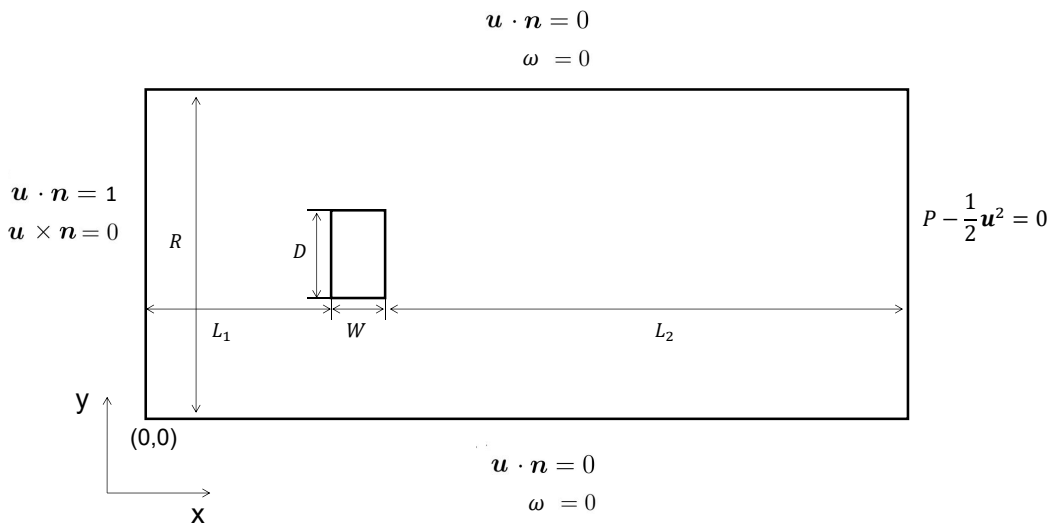

Figure 4.26: Domain geometry and boundary conditions for the flow over a rectangular cylinder.

In this case, a nonuniform orthogonal grid is used to discretize the domain, refined near the cylinder wall to resolve the boundary layer, shown in Fig.4.27. The thickness of the first layer element $\sigma = 0.02D$, the number of the elements along horizontal direction $K_x = 170$ and along vertical direction $K_y = 112$. And the order of the element is chosen as $N = 2$.
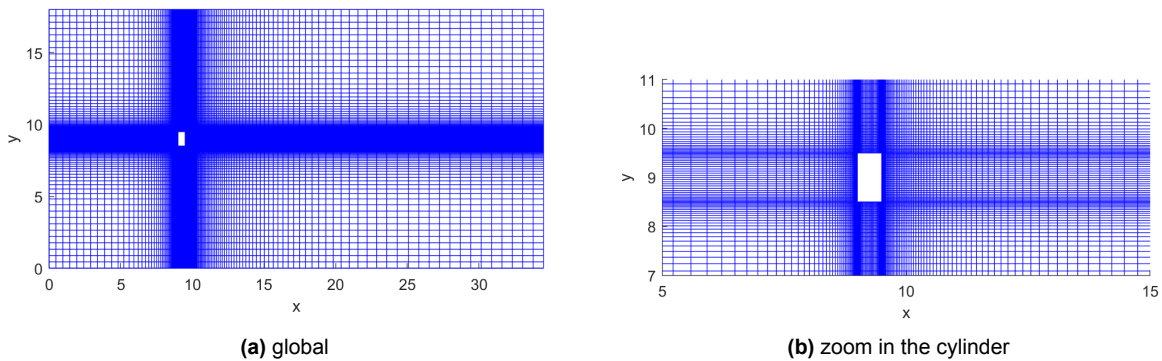

(a) global

(b) zoom in the cylinder

Figure 4.27: A nonuniform orthogonal grid for the flow over a rectangular cylinder, where $K_x = 170$, $K_y = 112$.

We use the MEEVC scheme in the framework of the hdMSEM with the novel dual grid proposed in Section 3.3.3 for time stepping, where the time step $\Delta t = 1$ in this case, and the tolerance of the Newton-iteration in solving the nonlinear system is 10^{-7}.

The Reynolds number, in this case, is defined as

$$Re = \frac{D\hat{u}_\perp}{\nu}, \tag{4.18}$$

where the width of the cylinder $D = 1$ and the the inlet velocity $\hat{u}_\perp = 1$. We firstly set $Re = 35$, when the flow field converges to a stable solution according to the study of Mashhadi et al. [56]. The numerical solutions of the flow field in the steady flow are shown in Fig. 4.28. Besides, we investigate the lift coefficient C_l and the drag coefficient C_d in the time stepping and compare with the DNS solution in FVM given by Mashhadi et al. [56], see in Fig. 4.29. The solution in the present study matches very well with the reference values.

(a) stream function

(b) vorticity
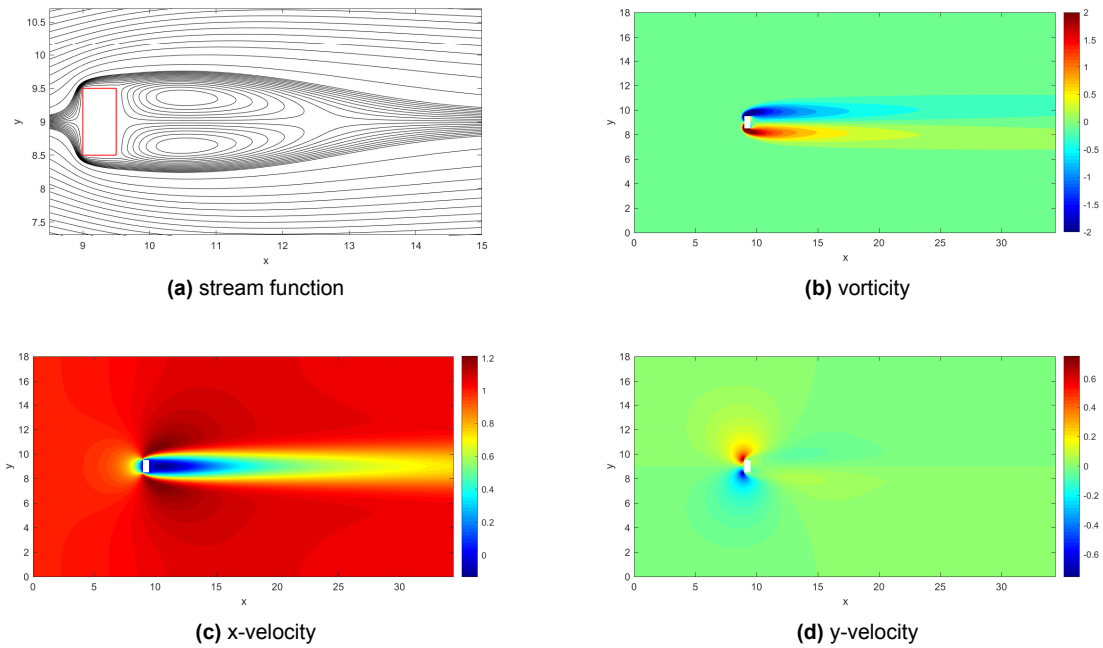
(c) x-velocity

(d) y-velocity

Figure 4.28: Numerical solution of stream function, vorticity, x-velocity and y-velocity at $Re = 35$.

(a) lift coefficient
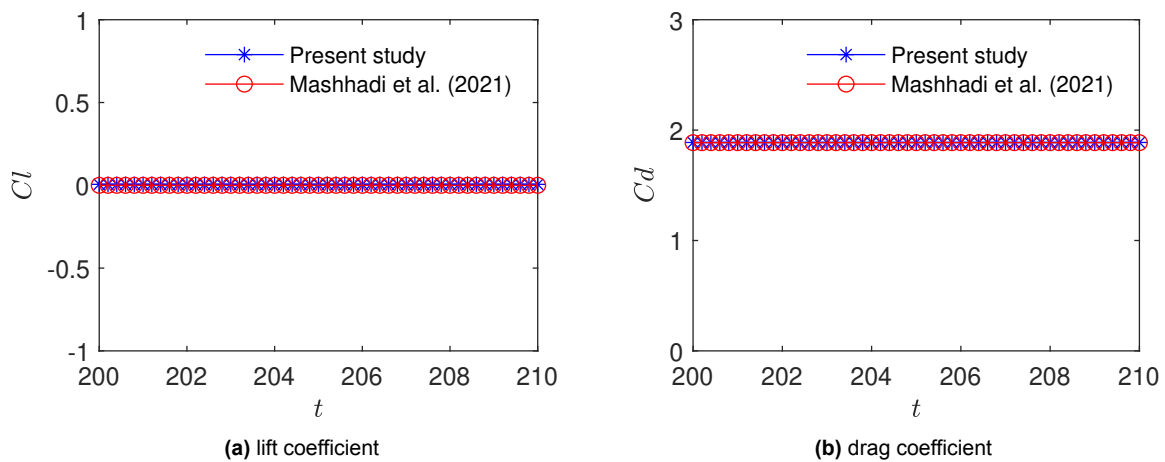
(b) drag coefficient

Figure 4.29: Lift coefficient and drag coefficient at $Re = 35$.

(a) stream function

(b) vorticity

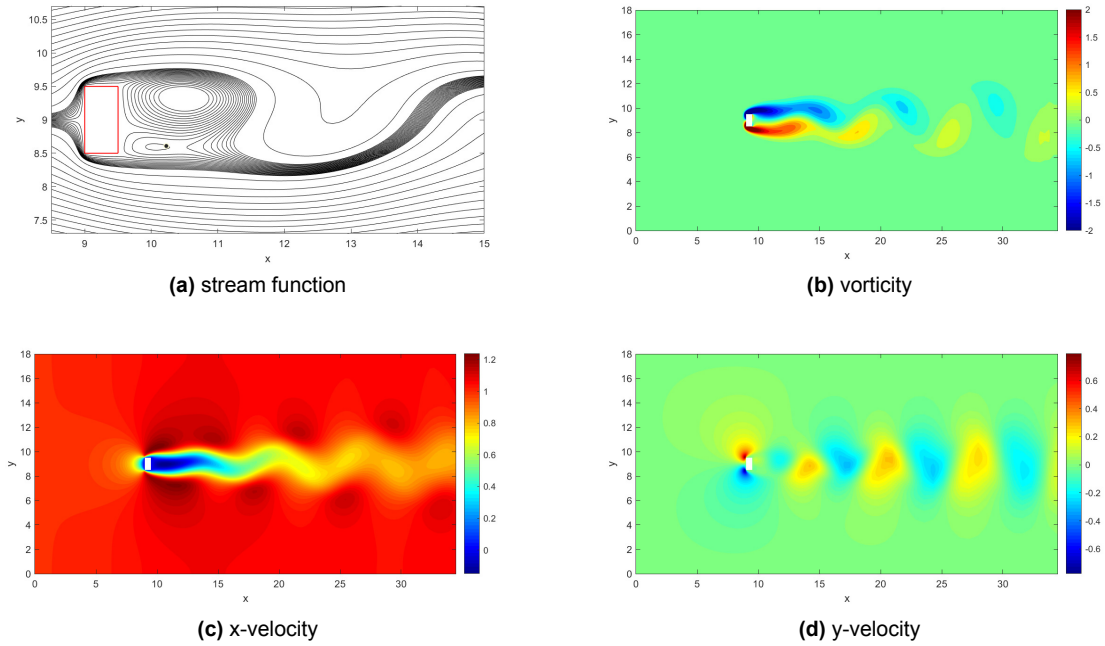**(c)** x-velocity

(d) y-velocity

Figure 4.30: Snapshot of the numerical solution of stream function, vorticity, x-velocity and y-velocity at $Re = 40$.

	present study	Mashhadi et al. (2021)	relative difference
$\overline{C_d}$	1.830	1.833	0.16%
$C_d{}'$	1.466×10^{-4}	1.496×10^{-4}	2.03%
$C_l{}'$	3.562×10^{-2}	3.523×10^{-2}	1.11%
T_{C_d}	4.204	4.355	3.57%
T_{C_l}	8.407	8.709	3.57%

Table 4.3: Oscillation parameters of drag coefficient and lift coefficient when $Re = 40$.

Next, the Reynolds number is increased to $Re = 40$. The flow field solutions are presented in Fig. 4.32. Compared with the case when $Re = 35$, it is evident that the critical Reynolds number between the steady solution and the unsteady solution is between $Re = 35$ and $Re = 40$, and the present numerical scheme is sensitive enough to predict the transition. A comparison between the C_l and C_d in the present study and reference solution [56] is demonstrated in Fig. 4.31. We define the root mean square of the drag and lift coefficient as

$$C_d' = \sqrt{\frac{1}{N}\sum_1^N (C_d(t) - \overline{C_d})^2},$$

$$C_l' = \sqrt{\frac{1}{N}\sum_1^N (C_l(t) - \overline{C_l})^2},$$

(4.19)

and investigate the mean value of the drag coefficient $\overline{C_d}$, the root mean square of the drag coefficient $C_d{}'$, the root mean square of the lift coefficient $C_l{}'$, the period of the drag coefficient T_{C_d} and the period of the lift coefficient T_{C_l}, see in Table 4.3. From this, it can be seen that the relative difference between the solution in the present study and the reference solution [56] is less than 5%. In addition, the period of lift coefficient is exactly twice as long as the period of drag coefficient, and the lift coefficient reaches the peak at the same time when drag coefficient reaches the maximum.

Finally, we study the case when $Re = 100$. The numerical solution of the flow fields at $Re = 100$ can be found in Fig. 4.32, where a more significant vortex shedding behavior can be observed.
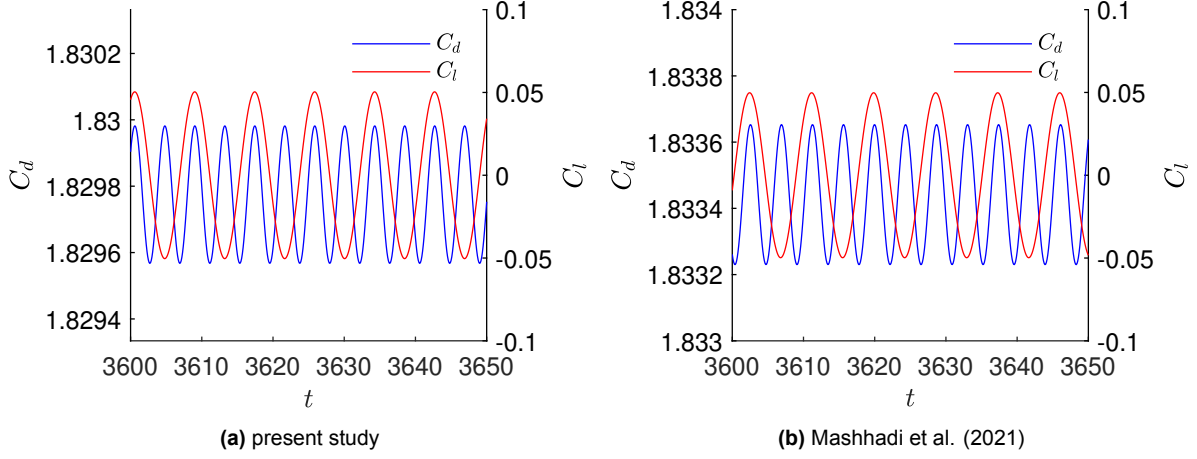
(a) present study **(b)** Mashhadi et al. (2021)

Figure 4.31: Lift coefficient and drag coefficient at $Re = 40$.

	present study	Mashhadi et al. (2021)	relative difference
$|u_1'|_{\max}$	4.807×10^{-2}	4.668×10^{-2}	2.89%
$|u_2'|_{\max}$	4.445×10^{-2}	4.358×10^{-2}	1.96%
$T_{u_1'}$	5.891	5.726	2.80%
$T_{u_2'}$	5.891	5.726	2.80%
Δt	0.940	0.927	1.40%

Table 4.4: Oscillation parameters of u_1' and u_2' when $Re = 100$.

The accuracy of the global field solution can be verified by comparing the velocity's mean field and fluctuation field with the reference solution [56]. We denote x' as the downstream distance, i.e., $x' = x - L_1 - W$ and y' as the vertical distance from the axis of symmetry, i.e., $y' = y - \frac{R}{2}$. then the profile of mean velocity at $x' = 16$ is shown in Fig. 4.33, where the present solution matches very well with the reference solution despite a bulge occurs at the region between wake and outer free stream in the present solution. The fluctuation of the x-velocity at the path of the vortex core is compared in Fig. 4.34 with the oscillation parameters presented in Table 4.4, where Δt is the time lag between the phase of u_1' and u_2' and depends on the streamwise convective velocity. The relative difference between the solution with the present method and the reference solution is less than 3%, which verifies the accuracy of the global field solution.

In addition, we aim to examine the resolution of the boundary layer with the current grid. A coarser grid is given, of which $\sigma = 0.025D$, $K_x = 156$ and $K_y = 100$, while the current grid has $\sigma = 0.02D$, $K_x = 170$ and $K_y = 112$. The lift and drag coefficients computed with the coarse grid and fine grid are shown in Fig. 4.35, and the oscillation parameters can be found in Table 4.5, from which it can be seen that the relative difference is less than 1.5%. This grid independence test proves that the grid shown in Fig. 4.27, which is used at $Re = 35$, $Re = 40$, and $Re = 100$, is fine enough to resolve the boundary layer.

Finally, we investigate the structure-preserving capability in solving the unsteady Navier-Stokes equations. Fig. 4.36 demonstrates that the L^2-errors of the discrete conservation law of mass and vorticity in time stepping are below 10^{-13}. It is important to note that although the tolerance for Newton iterations to solve the nonlinear system is set as 10^{-7} in the case, the L^2 error of the discrete conservation law can reach a lower level because it is only dependent on the floating-point precision as the two discrete constitutive equations,

$$\omega^h - \nabla \times \boldsymbol{u}^h = 0, \tag{4.20a}$$

$$\nabla \cdot \boldsymbol{u}^h = 0, \tag{4.20b}$$

are linear.

(a) stream function

(b) vorticity

(c) x-velocity

(d) y-velocity

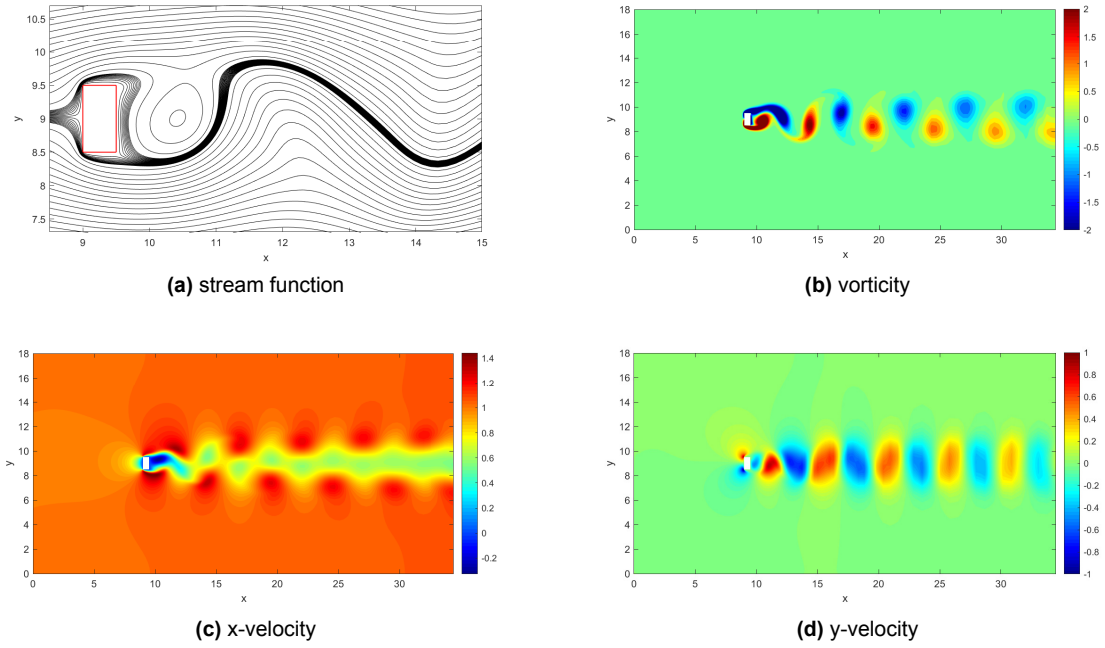**Figure 4.32:** Snapshot of the numerical solution of stream function, vorticity, x-velocity and y-velocity at $Re = 100$.
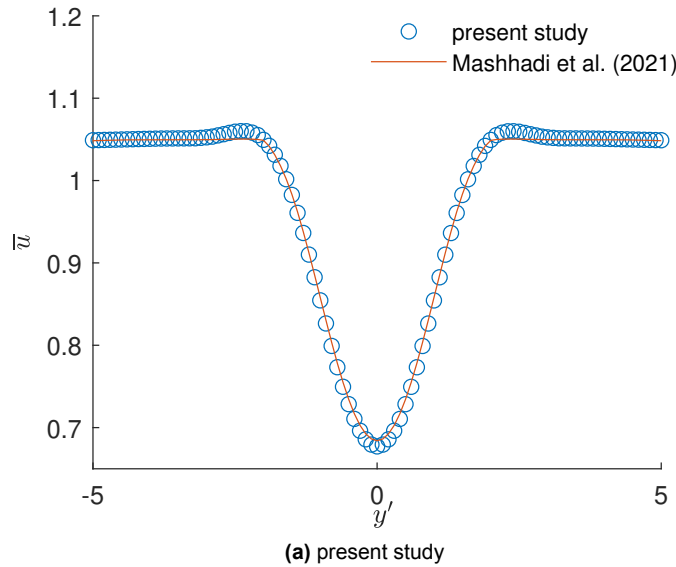

(a) present study

Figure 4.33: Profile of mean x-velocity $\overline{u}$ at $x' = 16$.

	coarse grid	fine grid	relative difference
$\overline{C_d}$	1.793	1.782	0.62%
$C_d{}'$	3.370×10^{-2}	3.395×10^{-2}	0.73%
$C_l{}'$	3.228×10^{-1}	3.267×10^{-1}	1.19%
T_{C_d}	2.923	2.946	0.76%
T_{C_l}	5.846	5.891	0.76%

Table 4.5: Oscillation parameters of drag coefficient and lift coefficient when $Re = 100$.
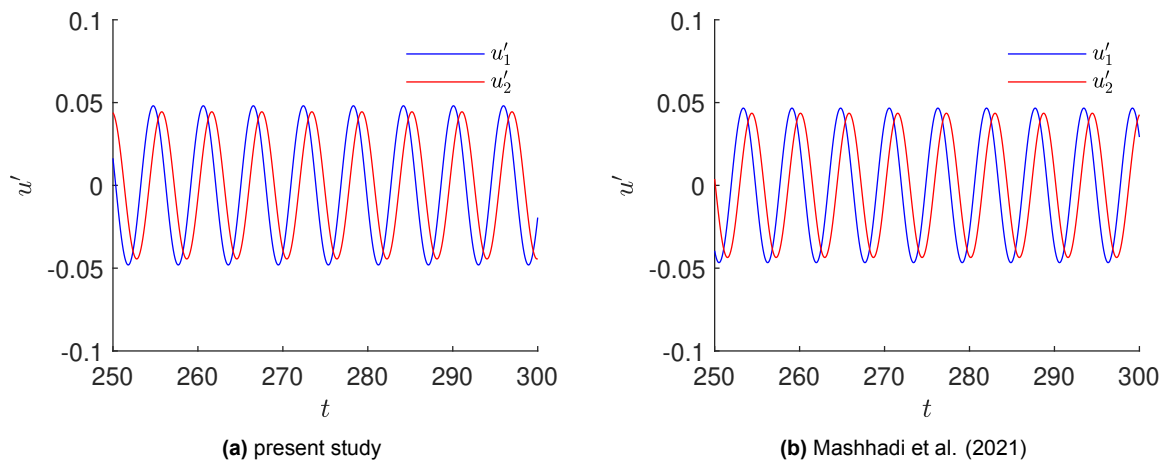
Figure 4.34: Fluctuation of x-velocity at the path of the vortex core u'_1 (at $x' = 16$) and u'_2 (at $x' = 17$).
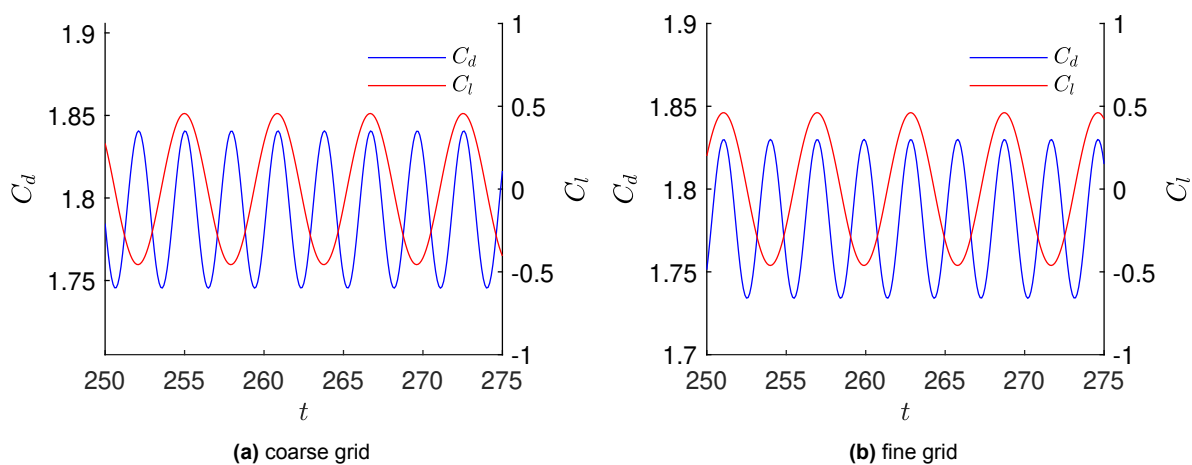

Figure 4.35: Lift coefficient and drag coefficient with coarse grid ($\sigma = 0.025D$, $K_x = 156$ and $K_y = 100$) and fine grid ($\sigma = 0.02D$, $K_x = 170$ and $K_y = 112$), when $Re = 100$.
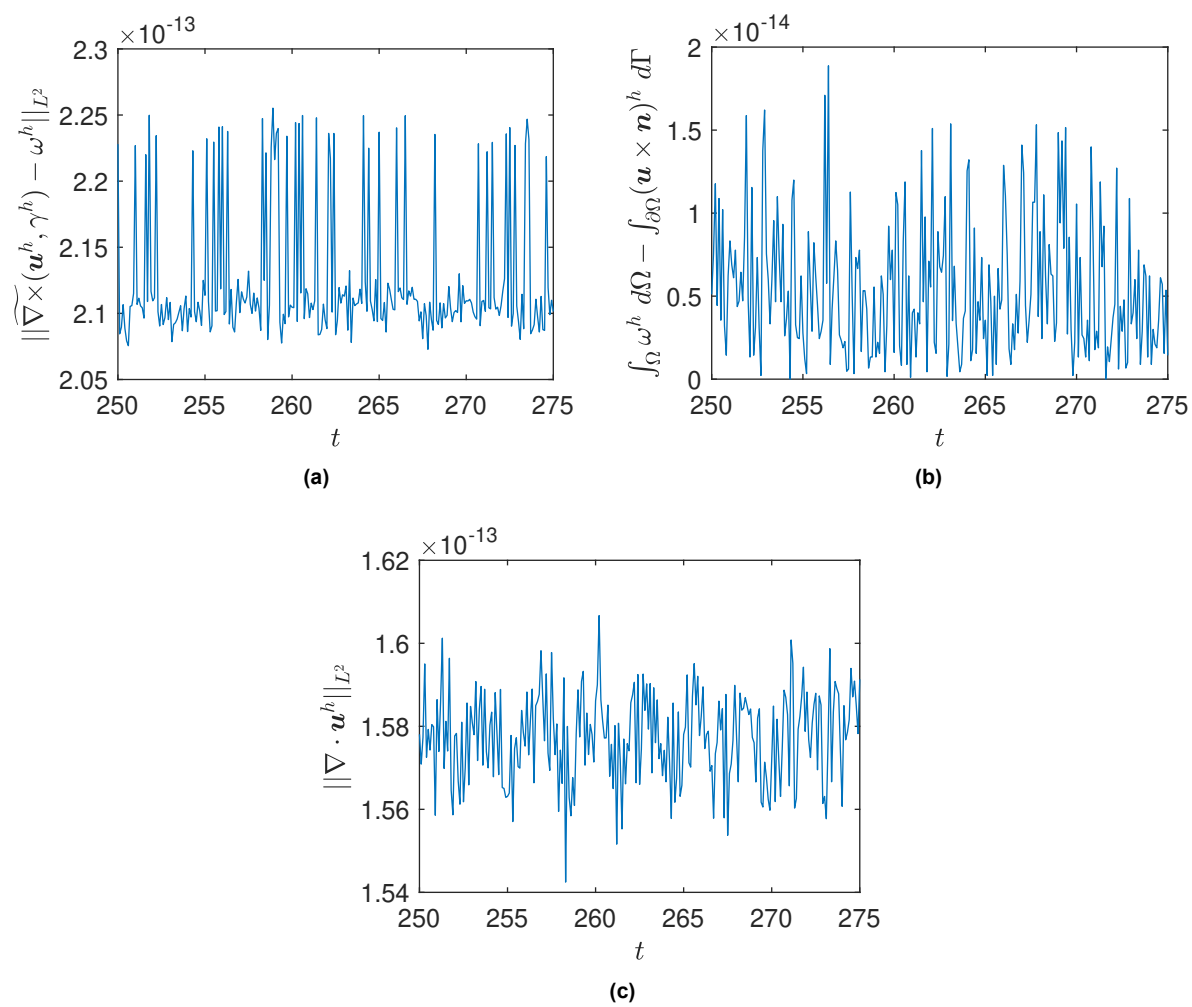
Figure 4.36: $L^2 -$ norm of $\widetilde{\nabla \times}(\boldsymbol{u}^h, \gamma^h) - \omega^h$, $\int_\Omega \omega^h \, d\Omega - \int_{\partial\Omega} (\boldsymbol{u} \times \boldsymbol{n})^h \, d\Gamma$ and $\nabla \cdot \boldsymbol{u}^h$ in time stepping when $Re = 100$.

<div align="right">

5

</div>

Conclusion and Recommendation for Future Work

5.1. Conclusion

This thesis proposed the hdMSEM with a novel dual grid and firstly extended it to solving steady and unsteady 2D incompressible Navier-Stokes flow with the pressure-linked pseudo-time-stepping method and the mass, energy, enstrophy, and vorticity conserving (MEEVC) scheme. In numerical experiments, the present study output physical resolutions match the analytical/reference solutions well, and the discrete conservation laws are examined. For the research questions of this thesis, we can conclude as follows:

1. Can we propose a novel dual grid for the hdMSEM to eliminate the singularity problem while keeping the discrete system symmetrical and the mathematical definition of matrix equations rigorous?

    In Section 3.1, we propose a novel dual grid by introducing a dummy degree at the edge where four elements meet and applying a curvilinear dual grid for trace variables, demonstrate the symmetry of the matrix of the discrete system, and clarify the mathematical definition of the matrix equations. The numerical experiments in Section 4 demonstrate that the hdMSEM with the novel dual grid can output accurate solutions with no singularity problem for the numerical system. At the same time, the discrete conservation laws of mass and vorticity are verified. In Section 4.1, we discuss the theoretical parallel efficiency of the hdMSEM with the novel dual grid by investigating the number of degrees of freedom and the condition number of the global discrete system.

2. How to implement different boundary conditions in hdMSEM with the novel dual grid?

    In Section 3.2, we propose a set of the dual grid topology near different kinds of boundaries and the corresponding implementation of boundary conditions in matrix formulation. All types of boundary conditions mentioned in Section 3.2 are verified in the numerical experiments in Section 4. Besides, in Section 4.2, we investigate the physical meaning of the dual degrees of freedom near the boundary, and in Section 4.3, we prove the hdMSEM with the novel dual grid can capture the physical singularity in vorticity field at the corner.

3. How to extend the hdMSEM with the novel dual grid to solve steady and unsteady incompressible Navier-Stokes equations and implement the MEEVC scheme in the framework of the hdMSEM with the novel dual grid?

    In Section 3.3, we implemented the pressure-linked pseudo time-stepping method and the mass, energy, enstrophy, and vorticity conserving (MEEVC) scheme in the framework of the hdMSEM with the novel dual grid for solving steady Navier-Stokes equations and unsteady Navier-Stokes equations respectively. The backward-facing step flow case in Section 4.4 proves the convergence and accuracy of the method for steady case; the flow over rectangular cylinder case in Section 4.5 demonstrates precision of the method in simulating unsteady Navier-Stokes flow, as the amplitude, frequency and mean value match well with reference solutions. In addition, the discrete conservation laws for vorticity and mass are verified for both steady and unsteady cases, where there is only floating-point errors are introduced in the discrete conservation law.

5.2. Recommendation for Future Work

This paper lays the foundation for using hdMSEM to solve incompressible Navier-Stokes equations, on which further research and development can be carried out. Here, we raise two issues that deserve to be researched in the future:

5.2.1. Boundary Implementation and Discrete Conservation Law in Curvilinear Grid

In this thesis, all numerical experiments were tested using orthogonal grids. Therefore, the performance of the method on the curvilinear grid has to be studied and verified. Here we give two questions to focus on: 1. In section 3.3.2, we verified that for the trace degrees of freedom $\tilde{\gamma}$ on the face perpendicular to the boundary, the value of $M_{TE}\tilde{\gamma}$ at the boundary is precisely the normal velocity at the boundary, and then, in a curved grid, is it equal to the velocity along the curvlinear grid line? 2. Theoretically speaking, the discrete conservation laws of vorticity and mass are independent of the grid geometry in the frame of hdMSEM, so they are expected to be verified on the curvilinear grid.

5.2.2. Verification of the Discrete Conservation Laws of Enstrophy and Energy for 2D Unsteady Incompressible Navier-Stokes Equations

The MEEVC scheme in the framework of MSEM is proven to preserve the conservation law for mass, vorticity, enstrophy, and energy in solving 2D unsteady incompressible Navier-Stokes equations [46, 47]. In this thesis, the discrete conservation laws of mass and vorticity have been verified. However, the cases in this thesis cannot examine the conservation of enstrophy and energy, as the analytical solutions of the dissipation rate of enstrophy and energy still need to be discovered. In future work, the discrete conservation law of enstrophy and energy with the MEEVC scheme implemented in the framework of the hdMSEM with the novel dual grid is expected to be verified by benchmark case such as 2D shear layer roll-up test, where there is no external force, net flux of energy and enstrophy over the domain boundary. Hence, the dissipation rate of enstrophy and energy can be defined analytically.

References

[1] Enzo Tonti. *The mathematical structure of classical and relativistic physics*. Vol. 10. Springer, 2013.

[2] Hassler Whitney. *Geometric integration theory*. Courier Corporation, 2012.

[3] Enzo Tonti et al. *On the formal structure of physical theories*. Istituto di matematica del Politecnico di Milano, 1975.

[4] Marc Gerritsma. "Edge Functions for Spectral Element Methods". In: vol. 76. Oct. 2010, pp. 199–207. DOI: `10.1007/978-3-642-15337-2_17`.

[5] Artur Palha. "High order mimetic discretization; development and application to Laplace and advection problems in arbitrary quadrilaterals". PhD thesis. Technische Universiteit Delft, 2013.

[6] J Kreeft. "Mimetic spectral element method; a discretization of geometry and physics". PhD thesis. Technische Universiteit Delft, 2013.

[7] Marc Gerritsma. "An Introduction to a Compatible Spectral Discretization Method". In: *Mechanics of Advanced Materials and Structures - MECH ADV MATER STRUCT* 19 (Jan. 2012). DOI: `10.1080/15376494.2011.572237`.

[8] Jasper Kreeft et al. "Mimetic framework on curvilinear quadrilaterals of arbitrary order". In: *arXiv preprint arXiv:1111.4304* (2011).

[9] Yi Zhang et al. "A hybrid mimetic spectral element method for three-dimensional linear elasticity problems". In: *Journal of Computational Physics* 433 (Feb. 2021), p. 110179. DOI: `10.1016/j.jcp.2021.110179`.

[10] Yi Zhang et al. "A hybrid mimetic spectral element method for the vorticity-velocity-pressure formulation of the Stokes equations". In: *ENUMATH 2019*. Egmond aan Zee, the Netherlands, 2019. URL: `www.mathischeap.com/contents/TALKS/ENUMATH_2019_Stokes_talk.html`.

[11] Enzo Tonti. "The reason for analogies between physical theories". In: *Applied Mathematical Modelling* 1.1 (1976), pp. 37–50.

[12] Enzo Tonti et al. "The algebraic-topological structure of physical theories". In: *Conference on Symmetry, Similarity and Group Theoretic Methods in Mechanics, Calgary (Canada)*. Academic Press. 1977, pp. 441–467.

[13] Enzo Tonti. "On the Mathematical Structure of a Large Class of Physical Theories". In: *Rend. Acc. Lincei* 52 (Dec. 1971), p. 13.

[14] Raoul Bott et al. *Differential forms in algebraic topology*. Vol. 82. Springer, 1982.

[15] J Blair Perot et al. "Differential forms for scientists and engineers". In: *Journal of Computational Physics* 257 (2014), pp. 1373–1393.

[16] Enzo Tonti. "Why starting from differential equations for computational physics?" In: *Journal of Computational Physics* 257 (2014), pp. 1260–1290.

[17] Theodore Frankel. *The geometry of physics: an introduction*. Cambridge university press, 2011.

[18] John M Lee et al. *Smooth manifolds*. Springer, 2012.

[19] Edwin H Spanier. *Algebraic topology*. Springer Science & Business Media, 1989.

[20] Albrecht Dold. *Lectures on algebraic topology*. Springer Science & Business Media, 2012.

[21] Jozef Dodziuk. "Finite-difference approach to the Hodge theory of harmonic forms". In: *American Journal of Mathematics* 98.1 (1976), pp. 79–104.

[22] Jonni Lohi et al. "Whitney forms and their extensions". In: *Journal of Computational and Applied Mathematics* 393 (2021), p. 113520.

[23] Franco Brezzi. "On the existence, uniqueness and approximation of saddle-point problems arising from Lagrangian multipliers". In: *Publications mathématiques et informatique de Rennes* S4 (1974), pp. 1–26.

[24] Franco Brezzi et al. "Two families of mixed finite elements for second order elliptic problems". In: *Numerische Mathematik* 47 (1985), pp. 217–235.

[25] Franco Brezzi et al. *Mixed and hybrid finite element methods*. Vol. 15. Springer Science & Business Media, 2012.

[26] Jean-Claude Nédélec. "Mixed finite elements in $\mathbb{R}^3$". In: *Numerische Mathematik* 35 (1980), pp. 315–341.

[27] Jean-Claude Nédélec. "A new family of mixed finite elements in $\mathbb{R}^3$". In: *Numerische Mathematik* 50 (1986), pp. 57–81.

[28] Pierre-Arnaud Raviart et al. "A mixed finite element method for 2-nd order elliptic problems". In: *Mathematical Aspects of Finite Element Methods: Proceedings of the Conference Held in Rome, December 10–12, 1975*. Springer. 2006, pp. 292–315.

[29] Alain Bossavit. "Mixed finite elements and the complex of Whitney forms". In: *The mathematics of finite elements and applications VI* 137 (1988), p. 144.

[30] Alain Bossavit. "Whitney forms: A class of finite elements for three-dimensional computations in electromagnetism". In: *IEE Proceedings A (Physical Science, Measurement and Instrumentation, Management and Education, Reviews)* 135.8 (1988), pp. 493–500.

[31] Alain Bossavit. "Solving Maxwell equations in a closed cavity, and the question of 'spurious modes'". In: *IEEE Transactions on magnetics* 26.2 (1990), pp. 702–705.

[32] Pavel B Bochev et al. "Principles of mimetic discretizations of differential operators". In: *Compatible spatial discretizations*. Springer. 2006, pp. 89–119.

[33] Mathieu Desbrun et al. "Discrete exterior calculus". In: *arXiv preprint math/0508341* (2005).

[34] Anil N Hirani et al. "Delaunay hodge star". In: *Computer-Aided Design* 45.2 (2013), pp. 540–544.

[35] Theodore HH Pian et al. *Hybrid and incompatible finite element methods*. CRC press, 2005.

[36] Theodore HH Pian. "Derivation of element stiffness matrices by assumed stress distributions". In: *AIAA journal* 2.7 (1964), pp. 1333–1336.

[37] Pin Tong. "New Displacement Hybrid Finite Element Models for Solid Continua". In: *International Journal for Numerical Methods in Engineering* 2 (June 1970), pp. 73–83. DOI: `10.1002/nme.1620020108`.

[38] Theodore Pian. "Variational principles for incremental finite element methods". In: *Journal of The Franklin Institute-engineering and Applied Mathematics - J FRANKLIN INST-ENG APPL MATH* 302 (Nov. 1976), pp. 473–488. DOI: `10.1016/0016-0032(76)90037-5`.

[39] F. B. Belgacem et al. "The mortar element method for three dimensional finite elements". In: *ESAIM: Mathematical Modelling and Numerical Analysis* 31.2 (1997), pp. 289–302.

[40] Wohlmuth et al. "A Mortar Finite Element Method Using Dual Spaces for the Lagrange Multiplier". In: *SIAM Journal on Numerical Analysis* (2000).

[41] Axel et al. "Dual-primal FETI methods for linear elasticity". In: *Communications on Pure & Applied Mathematics* (2006).

[42] F. Brezzi. "On the Existence, Uniqueness and Approximation of Saddle-Point Problems Arising from Lagrangian Multipliers". In: *Revue française d automatique informatique recherche opérationnelle Mathématique* 8.NR2 (1974).

[43] Y. Zhang et al. "The Discrete Steklov–Poincaré Operator Using Algebraic Dual Polynomials". In: *Computational Methods in Applied Mathematics* (2019).

[44] Yi Zhang. "Mimetic Spectral Element Method and Extensions toward Higher Computational Efficiency". In: (2022).

[45] Woźny et al. "Construction of dual bases". In: *Journal of Computational & Applied Mathematics* 245 (2013), pp. 75–85.

[46] Artur Palha et al. "A mass, energy, enstrophy and vorticity conserving (MEEVC) mimetic spectral element discretization for the 2D incompressible Navier-Stokes equations". In: *Journal of Computational Physics* 328 (Apr. 2016). DOI: `10.1016/j.jcp.2016.10.009`.

[47] Yi Zhang et al. "A MEEVC discretization for two-dimensional incompressible Navier-Stokes equations with general boundary conditions". In: *arXiv preprint arXiv:2307.08166* (2023).

[48] Thomas James Willmore. *An introduction to differential geometry*. Courier Corporation, 2013.

[49] Seymour V Parter. "On the Legendre–Gauss–Lobatto points and weights". In: *Journal of scientific computing* 14 (1999), pp. 347–355.

[50] Olga Taussky. "The role of symmetric matrices in the study of general matrices". In: *Linear Algebra and its Applications* 5.2 (1972), pp. 147–154.

[51] David Ronald Kincaid et al. *Numerical analysis: mathematics of scientific computing*. Vol. 2. American Mathematical Soc., 2009.

[52] Ercan Erturk. "Numerical solutions of 2-D steady incompressible flow over a backward-facing step, Part I: High Reynolds number solutions". In: *Computers & Fluids* 37.6 (2008), pp. 633–655.

[53] David K Gartling. "A test problem for outflow boundary conditions—flow over a backward-facing step". In: *International Journal for Numerical Methods in Fluids* 11.7 (1990), pp. 953–967.

[54] G Guj et al. "Numerical solutions of high-Re recirculating flows in vorticity-velocity form". In: *International journal for numerical methods in fluids* 8.4 (1988), pp. 405–416.

[55] Ahmad Sohankar et al. "Low-Reynolds-number flow around a square cylinder at incidence: study of blockage, onset of vortex shedding and outlet boundary condition". In: *International journal for numerical methods in fluids* 26.1 (1998), pp. 39–56.

[56] A Mashhadi et al. "Flow over rectangular cylinder: Effects of cylinder aspect ratio and Reynolds number". In: *International Journal of Mechanical Sciences* 195 (2021), p. 106264.
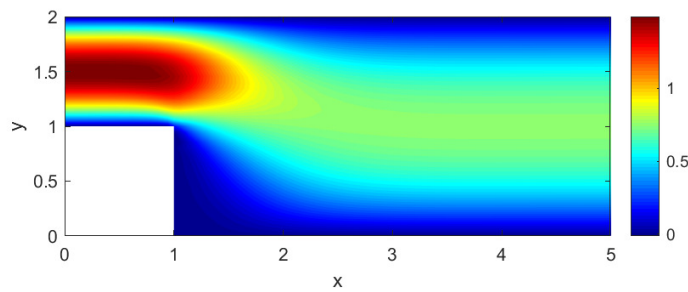
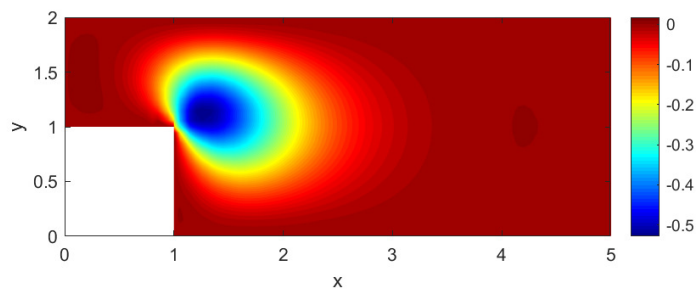# A
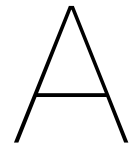
Numerical Solutions
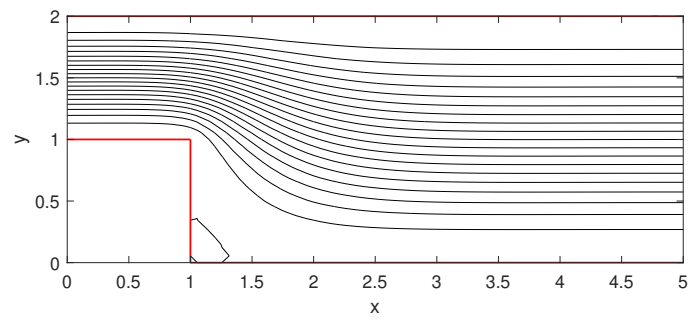
(a) stream function
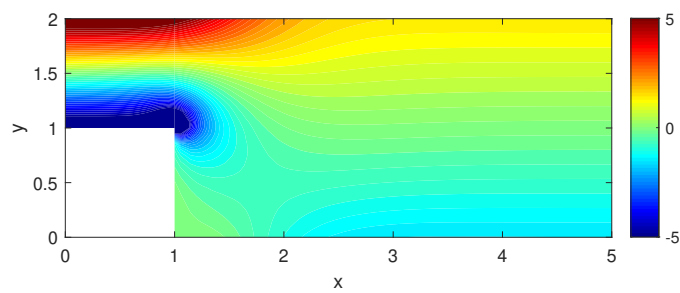
(b) vorticity

(c) x-velocity

(d) y-velocity

Figure A.1: Numerical solution of stream function, vorticity, x-velocity and y-velocity for backward-facing step Stokes flow, when $N = 3$ and $h = 1/5$.